University of Groningen

Electronic and structural properties of graphene/metal interfaces

Bignardi, Luca

IMPORTANT NOTE: You are advised to consult the publisher's version (publisher's PDF) if you wish to cite from it. Please check the document version below.

Document Version
Publisher's PDF, also known as Version of record

Publication date:
2013

Link to publication in University of Groningen/UMCG research database

Citation for published version (APA):
Bignardi, L. (2013). *Electronic and structural properties of graphene/metal interfaces*. s.n.

Copyright
Other than for strictly personal use, it is not permitted to download or to forward/distribute the text or part of it without the consent of the author(s) and/or copyright holder(s), unless the work is under an open content license (like Creative Commons).

The publication may also be distributed here under the terms of Article 25fa of the Dutch Copyright Act, indicated by the “Taverne” license. More information can be found on the University of Groningen website: https://www.rug.nl/library/open-access/self-archiving-pure/taverne-amendment.

Take-down policy
If you believe that this document breaches copyright please contact us providing details, and we will remove access to the work immediately and investigate your claim.

Downloaded from the University of Groningen/UMCG research database (Pure): http://www.rug.nl/research/portal. For technical reasons the number of authors shown on this cover page is limited to 10 maximum.

Download date: 05-05-2023

Electronic and structural properties of graphene/metal interfaces

Luca Bignardi

Zernike Institute PhD thesis series: 2013-12
ISSN: 1570-1530
ISBN: 978-90-367-6258-8 (electronic)
ISBN: 978-90-367-6259-5 (printed)

The work described in this thesis was performed in the research group Surfaces and Thin Films of the Zernike Institute for Advanced Materials, University of Groningen. This work is part of the research program of the Stichting voor Fundementeel Onderzoek der Materie (FOM), part of the Nederlandse Organisatie voor Wetenschappelijk Onderzoek (NWO).

Printed by: Ipskamp Drukkers B.V. – Enschede (NL)
Cover design: Luca and Paolo Bignardi. The cover picture represents a schematic of the photoemission process, as an ideal tool to unravel the electronic band structure of a graphene layer and to observe electrons from the Dirac cone.

RIJKSUNIVERSITEIT GRONINGEN

Electronic and structural properties of graphene/metal interfaces

Proefschrift

ter verkrijging van het doctoraat in de
Wiskunde en Natuurwetenschappen
aan de Rijksuniversiteit Groningen
op gezag van de
Rector Magnificus, dr. E. Sterken,
in het openbaar te verdedigen op
dinsdag 18 juni 2013
om 11.00 uur

door

Luca Bignardi

geboren op 27 juli 1984
te Cremona, Italië

Promotor: Prof. dr. P. Rudolf
Copromotor: Dr. M. Stöhr

Beoordelingscommissie: Prof. dr. H. Zacharias
Prof. dr. G. Mistura
Prof. dr. ir. J.T.M. de Hosson

Contents

Alla mia famiglia,
con affetto e riconoscenza

Chapter One

Introduction

In this chapter we will sketch an overview of the state of the art of the investigation carried out on graphene/metal interfaces. Moreover, the experiments and results described in each chapter of the thesis will be outlined.

1.1 GRAPHENE/METAL INTERFACES

Carbon is the fourth most abundant chemical element by mass in the universe, after hydrogen, helium and oxygen. It plays a key role in the chemistry of life, being involved in the structure of all the building blocks of living beings. It is economically relevant because it composes hydrocarbons, which are the base of our present economic system.

Since its valence electrons can hybridize sp, sp^2 and sp^3, carbon is a very versatile element; it shows in nature several allotropes (see figure 1.1), with different crystalline structures and chemical bonds, such as diamond, graphite(and graphene), nanotubes and fullerenes, which surely have had a very relevant role in stimulating both fundamental and applied research. Moreover, it is remarkable to see that all the allotropes of carbon show a topological variety uncommon for other chemical elements (figure 1.1), going from 0D compounds (fullerenes) to fully 3D crystals (graphite, diamond).

Graphite, which exhibits a highly anisotropic crystalline structure, can easily be described as a stack of 2D carbon lattices, each of them known as graphene. Due to this peculiaricularity, the approach originally chosen to model the electronic properties of the 3D solid [2] was to explore the properties of the single graphene sheet and later combine them to obtain the 3D structure. Graphene can be considered as a building block for many other carbon-based materials, such as carbon nanotubes and fullerenes. It consists of a honeycomb sp^2-bonded lattice of carbon atoms. Its electronic band structure was calculated with a tight-binding approach already in 1947 [2], disclosing that a single layer of graphene has a linear energy dispersion E(k) at the K point of its Brillouin zone[1] which has later been found to be responsible for its very special electronic properties [3].

---

[1] An overview of the relevant properties of graphene is given in appendix A.

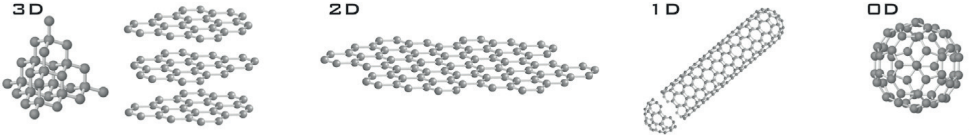

Figure 1.1: Crystal structures of the different allotropes of carbon. (Left to right) Three-dimensional diamond and graphite (3D); two-dimensional graphene (2D); one-dimensional nanotubes (1D); and zero-dimensional buckyballs (0D). (Adapted from [1]). © Elsevier 2007.

Peierls [4], Landau [5] and Mermin [6] theoretically proved that the existence of a self-standing single layer of graphene (as a 2D solid) was thermodynamically unfavorable, confining the existence of graphene to the pure theoretical speculation.

However, the formation of a (substrate supported) graphene single layer was postulated in 1968 to explain some low energy electron diffraction patterns observed (in Ultra-High Vacuum conditions, UHV) on the Pt(100) surface after exposure and subsequent dissociation of hydrocarbons (ethylene and propylene)[7]. Such outcome opened the way to studies concerning the dissociation of gaseous hydrocarbons on transition metal surfaces and therefore implementing the family of protocols that later were gathered under the definition of Chemical Vapour Deposition (CVD) of graphene.

An important point was marked in 2004, when a group of researchers from Manchester University, lead by K. Novoselov and A. Geim, reported a deposition method for a single layer of graphene on a silicon oxide substrate based on micro-mechanical cleavage of graphite. This outcome opened the way to the characterization of electrical properties of graphene [3]. Moreover, Novoselov and Geim showed how it was possible to deposit freestanding graphene layers onto a TEM grid [8]: these layers were stable as a matter of fact and were apparently confuting the prediction made by theory. This issue was solved by Fasolino *et al.* [9], which proved that the freestanding graphene was not flat but undulated and therefore posses a 3D structure. This undulations have been observed by convergent beam electron diffraction [10]

Although the large breakthrough in the field came only in the very recent years, in the second half of the 20th century several efforts were done in order to understand the properties of graphite, spurred by its possible application in nuclear technology [11]. Fundamental studies allowed to discover superconductive properties of some intercalated graphite compounds [12], which consist of a graphite matrix hosting intercalated species (generally, metallic atoms).

The CVD growth was proved to be the most suitable for the technological implementation of a mass scale production of graphene. The growth of graphene on Ni surfaces has been widely explored for many years, because it can be easily achieved by the methods described above. Specifically, graphene was grown in ultra-high vacuum (UHV) on Ni single crystals by exposure of the metallic surface to ethylene and it was found to constitute a thermodynamically stable surface termination, provided that the growth temperature was properly chosen [13, 14, 15]. Electronic decoupling of the graphene layer from the surface was later reported by intercalation of metallic atoms [16, 17].

After the first deposition of a graphene layer on silicon oxide in 2004, a huge raise of interest was directed towards this topic, involving many branches of physics and nanotechnology and indicating how graphene could lead rapidly to relevant applications [18]. Despite of the fact that the micro-mechanical cleavage method was proven to give high quality samples (*i.e.* low density of defects, high carrier mobility [19, 20]), it is obviously not suitable to implement a large-scale graphene production and device fabrications. Therefore, the CVD deposition protocols [21, 22, 23] and the procedures based on chemical exfoliation of graphite or reduction of graphite oxide [24, 25, 26] have been extensively explored and improved in the last years, yielding to the production of graphene flakes whose features, such as carrier mobility and density of defects, match the values obtained with micromechanical cleavage

Two different categories of CVD growth of graphene on metals can be distinguished in the literature [27, 23]:

i) Segregation of bulk carbon to the surface. The starting material for this method is a metallic bulk crystal either doped with carbon atoms, or presenting small amounts of carbon as impurities. With annealing at high temperature, the carbon atoms segregate to the surface forming a graphitic layer [28, 13].

ii) Decomposition of molecules containing carbon. A hot metallic surface is exposed to a carbon-containing gas (generally hydrocarbons). The catalytic decomposition of the gas molecules at the surface leads to the formation of a (graphitic) carbon layer. This technique is nowadays the most commonly used to grow graphene on metals.

In our experiments we always worked with the second method, because it is considered more reliable and controllable.

As mentioned earlier, the first observation of graphene on transition metal surfaces dates back to the studies carried out on single crystals. In the 1970s and 1980s there have been numerous contributions in that field, which have been summarized in several review papers [27, 23, 29]. A quite number of graphene/metal interfaces were investigated in the past years, as shown by the the table in figure 1.2. Among them we shall mention graphene on Ni(111) [30], graphene on Ir(111) [31, 32, 33], graphene on Pt(111) [34, 35] and graphene on Cu(111) [36].

A common scheme to classify the graphene/metal interfaces is based on the extent of the interaction between the graphene and the substrate, which can be either strong or weak [23]. In figure 1.2 we show a table listing all the graphene/metal interfaces so far explored and the relevant properties of them. A graphene layer that

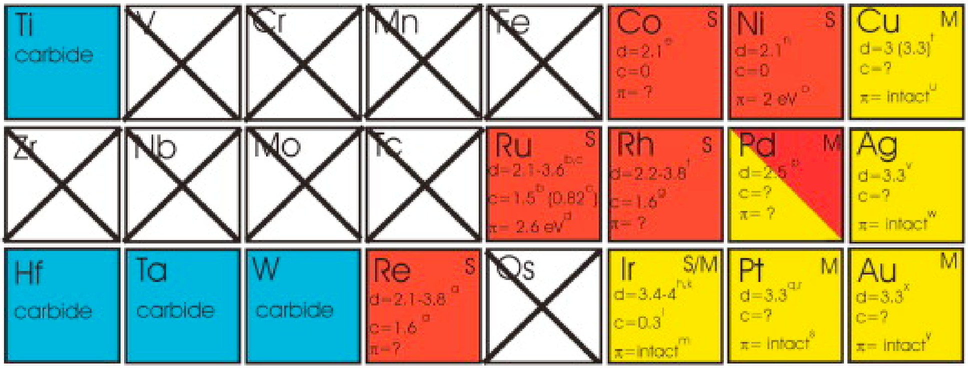

Figure 1.2: Summary of the interactions between transition metals and graphene. For the elements labelled in blue, graphene may grow on the bulk-carbides of these elements by segregation of carbon atoms. Elements in red are characterized as metals that interact strongly with graphene and elements in yellow are those that interact weakly. S or M in the upper right corner of each element-box indicates if graphene forms single or multiple rotational domains, d is the reported graphene-metal separation in Å. Different values may indicate the range of separations within the moiré superstructures. The buckling or corrugation of the graphene sheet is given by c in Å, and the amount of downward shift of the π-band is given by π (Intact, means that a linear dispersion at the Dirac point is still observed). After [23]. © 2012, Elsevier.

strongly interacts with the metal is characterized by large modifications in the shape of the π band, which commonly interacts and hybridizes with the electronic bands of the metal in the proximity of the Fermi level. This may turn out in a destruction of the Dirac cone together with a doping process of the graphene. A typical example of strongly interacting graphene is the graphene/Ni(111) interface [30]. On the other hand, if the graphene layer interact weakly with the substrate underneath, the shape of the electronic bands remains generally unaffected and a doping process of graphene is only observed. These features are typical of an interface such as graphene/Ir(111) [33, 31].

The basic adsorption structures of graphene on metals are shown in fig. 1.3, following the scheme adopted in [23]. The fcc-site (hcp-site) situation represents a graphene layer whose carbon atoms rest on top of the fcc-hollow (hcp-hollow) site of the substrate and other carbon atoms are found to be on atop sites. In the literature one sometimes also encounters a nomenclature that labels adsorption sites with respect to the centre of the carbon-ring, i.e. in that nomenclature fig. 1.3-(a) would be labeled 'atop', (b) hcp, and (c) fcc. However, only on Ni and possibly on Co a good lattice match between graphene and the metal substrate exists. This allows

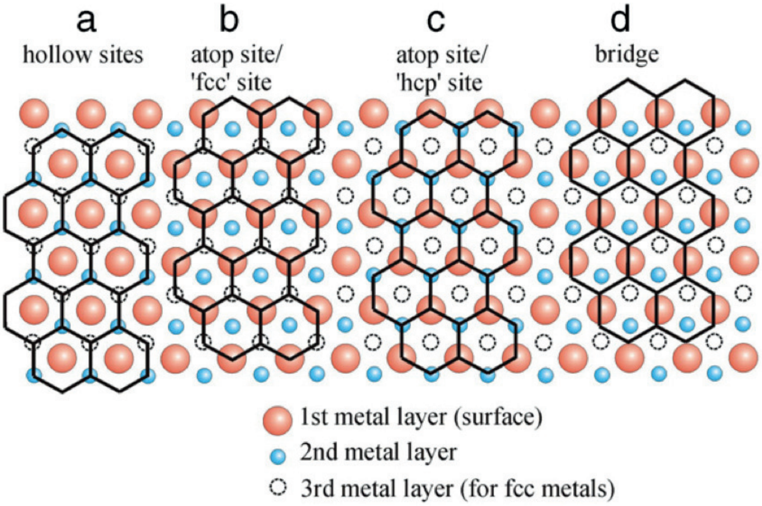

Figure 1.3: Four basic adsorption arrangements for non-rotated graphene on hexagonal (fcc(111) or hcp(0001)) metal surfaces. (a) All carbon atoms of graphene are located in three-fold hollow sites of the surface, i.e. the carbon-atoms surround the surface metal-atom. (b) Carbon atoms alternately occupy metal atop sites and the 'fcc' hollow sites. (c) Carbon atoms alternately occupy metal atop sites and the 'hcp' hollow sites. (d) Illustrates the adsorption structure known as bridge-structure. Here we use the nomenclature that labels the adsorption sites by the position of the carbon atoms with the respect to the substrate. Another sometimes used nomenclature labels the adsorption sites by the position of the centre of t carbon hexagon relative to the substrate. In this second alternative nomenclature (a) would be labelled 'atop', (b) 'hcp', (c) 'fcc', and (d) 'bridge' adsorption. After [23]. © 2012, Elsevier.

the graphene to adopt (at least within large domains) a single adsorption structure. For lattice mismatched systems the lattice of graphene and that of the substrate are incommensurate and therefore periodic repetitions of certain adsorption structures give rise to a Moiré pattern.

1.2 OUTLINE OF THIS THESIS

In this thesis, we present investigations of electronic and structural properties of some graphene/metal interfaces which were so far not completely understood. Such studies required a careful review of the growth protocols reported in the literature in order to reproduce them and thereby fully control the features of the interfaces. Our attention was devoted in particular to the electronic (filled and empty) states of graphene and to the dynamics of excited charge carriers. We have used a combination of several techniques of surfaces science, in order to have a complete overview of all the features of the selected interface. The final aim of this work is to give a contribution in increasing the knowledge about the electronic and structural properties of CVD graphene, investigating how the presence of the metallic substrate may affect these properties.

In chapter 2, the CVD methods and techniques used in the preparation of the graphene/metal interfaces shall be escribed. A preliminary characterization is also presented , which is complementary to what is illustrated in the following chapters.

Chapters 3 and 4 report on an investigation of the electronic properties of the graphene/Ni(111) interface by means of time-resolved photoemission spectroscopy experiments. A High-Harmonic Generation (HHG) setup allowed to investigate final-state effects in the photoelectron spectra of graphene/Ni. Furthermore, we studied the lifetimes of a photoexcited electron distribution. This work was carried out at the Physikalisiche Institut of the Westfälische Wilhelms-Universität Münster (Germany), together with Dr. Thorben Haarlammert, Dr. Carsten Winter, and Prof. Helmut Zacharias. Theoretical support has been provided by Prof. G. Fecher, Johannes Gutenberg-Universität Mainz (Germany) and by Dr. Elena Voloshina, Humbolt Universität zu Berlin (Germany).

Chapter 5 focusses on the characterization of the graphene/Cu(111) interface, by combining low energy electron diffraction, photoelectron spectroscopy and microscopy as well as scanning tunneling microscopy. A comprehensive view of the electronic and structural properties of the interface is given, determining the modification of graphene properties due to the interaction with the substrate. The influence of the different steps of the CVD growth procedure on the final graphene/Cu(111) interface are discussed as well. The Scanning Tunneling Microscopy investigations described in the chapter were carried out by Stefano Gottardi, Mihaela Enache, Dr. Kathrin Müller and Dr. Meike Stöhr, at the Zernike Institute for Advanced Materials, University of Groningen.

Chapter 6 presents a full characterization of CVD-grown graphene transferred to and suspended on TEM grids. In this way, one has access to the properties of bare graphene, without any interaction with the substrate. We could measure, by means of angle-resolved photoelectron spectroscopy and microscopy, the value of the Fermi velocity of the electrons at the Dirac point of graphene. The crystalline structure of the membrane was investigated by means of Transmission Electron Microscopy (TEM) and Raman spectroscopy. This study was carried out in collaboration with

Dr. Willem van Dorp and Prof. Dr. Jeff de Hosson (Material Science group) and Oleksii Ivashenko, Stefano Gottardi and Dr. Meike Stöhr (Surfaces and thin Films group) at the Zernike Institute for Advanced Materials.

Chapter 7 describes an investigation of the friction properties of a monolayer of Xe sliding over a layer of CVD graphene, grown on copper and later transferred on the surface of a quartz micro balance (QCM) covered with Au electrodes. We observed a complete depinning of the Xe monolayer at a temperature that is higher than what observed for a similar experiment performed on the bare Au covered quartz crystal. This work has been performed in collaboration with M. Pierno and prof. G. Mistura, who carried out the nanotribology measurements at the University of Padova, Italy. Theoretical support has been provided by prof. Pierluigi Silvestrelli (University of Padova).

In chapter 8, we focus our attention to the image potential states observed at the graphene/copper interface. Experiments carried out with 2-photon photoemission allowed us to determine the position and characteristics of an image potential state of this interface, which is detected both at the the graphene/Cu(111) and the graphene/Cu foil interfaces. This work was carried out in collaboration with Silvia Tognolini, Dr. Gianluca Galimberti and Dr. Stefania Pagliara (Dipartimento di Matematica e Fisica, Università Cattolica, Brescia, Italy) and Prof. Fulvio Parmigiani (Dipartimento di Fisica, Università degli Studi di Trieste, Italy). Electron backscattering diffraction was carried out with the help of Dr. W. van Dorp and Dr. V. Ocelík, Material Science group, Zernike Institute for Advanced Materials.

REFERENCES

[1] M. I. Katsnelson, *Materials today* **10**, 20 (2007).

[2] P. R. Wallace, *Physical Review* **71**, 622 (1947).

[3] K. S. Novoselov, A. K. Geim, S. V. Morozov, D. Jiang, Y. Zhang, S. V. Dubonos, I. V. Grigorieva, and A. A. Firsov, *Science* **306**, 666 (2004).

[4] R. Peierls, R. Peierls, and R. Dalitz, *Selected Scientific Papers of Sir Rudolf Peierls: With Commentary*, World Scientific Series in 20th Century Physics, World Scientific (1997).

[5] Landau L. D., *Phys. Z. Sowjetunion* **11**, 26 (1937).

[6] N. D. Mermin, *Physical Review* **176**, 250 (1968).

[7] A. E. Morgan and G. A. Somorjai, *Surface Science* **12**, 405 (1968).

[8] J. C. Meyer, A. K. Geim, M. I. Katsnelson, K. S. Novoselov, T. J. Booth, and S. Roth, *Nature* **446**, 60 (2007).

[9] A. Fasolino, J. H. Los, and M. I. Katsnelson, *Nature Materials* **6**, 858 (2007).

[10] J. C. Meyer, A. K. Geim, M. I. Katsnelson, K. S. Novoselov, D. Obergfell, S. Roth, C. Girit, and A. Zettl, *Solid State Communications* **143**, 101 (2007).

[11] B. Kelly, *Physics of Graphite*, RES mechanica monographs, Kluwer Academic Pub (1981).

[12] M. Dresselhaus and G. Dresselhaus, *Advances in Physics* **30**, 139 (1981).

[13] J. Shelton, H. Patil, and J. Blakely, *Surface Science* **43**, 493 (1974).

[14] Y. Gamo, A. Nagashima, M. Wakabayashi, M. Terai, and C. Oshima, *Surface Science* **374**, 61 (1997).

[15] C. Oshima and A. Nagashima, *Journal of Physics: Condensed Matter* **9**, 1 (1997).

[16] Y. Dedkov, A. Shikin, V. Adamchuk, S. Molodtsov, C. Laubschat, A. Bauer, and G. Kaindl, *Physical Review B* **64**, 1 (2001).

[17] A. Varykhalov, J. Sánchez-Barriga, A. Shikin, C. Biswas, E. Vescovo, A. Rybkin, D. Marchenko, and O. Rader, *Physical Review Letters* **101**, 1 (2008).

[18] A. T. S. Wee, *ACS Nano* **6**, 5739 (2012).

[19] K. S. Novoselov, D. Jiang, F. Schedin, T. J. Booth, V. V. Khotkevich, S. V. Morozov, and A. K. Geim, *Proceedings of the National Academy of Sciences of the United States of America* **102**, 10451 (2005).

[20] K. S. Novoselov, A. K. Geim, S. V. Morozov, D. Jiang, M. I. Katsnelson, I. V. Grigorieva, S. V. Dubonos, and A. A. Firsov, *Nature* **438**, 197 (2005).

[21] X. Li, W. Cai, J. An, S. Kim, J. Nah, D. Yang, R. Piner, A. Velamakanni, I. Jung, E. Tutuc, S. K. Banerjee, L. Colombo, and R. S. Ruoff, *Science* **324**, 1312 (2009).

[22] S. Bae, H. Kim, Y. Lee, X. Xu, J.-S. Park, Y. Zheng, J. Balakrishnan, T. Lei, H. Ri Kim, Y. I. Song, Y.-J. Kim, K. S. Kim, B. Ozyilmaz, J.-H. Ahn, B. H. Hong, and S. Iijima, *Nature Nanotechnology* **5**, 574 (2010).

[23] M. Batzill, *Surface Science Reports* **67**, 83 (2012).

[24] D. A. Dikin, S. Stankovich, E. J. Zimney, R. D. Piner, G. H. B. Dommett, G. Evmenenko, S. T. Nguyen, and R. S. Ruoff, *Nature* **448**, 457 (2007).

[25] S. Gilje, S. Han, M. Wang, K. L. Wang, and R. B. Kaner, *Nano Letters* **7**, 3394 (2007).

[26] R. Y. N. Gengler, K. Spyrou, and P. Rudolf, *Journal of Physics D: Applied Physics* **43**, 374015 (2010).

[27] J. Wintterlin and M.-L. Bocquet, *Surface Science* **603**, 1841 (2009).

[28] M. Eizenberg and J. M. Blakely, *The Journal of Chemical Physics* **71**, 3467 (1979).

[29] N. C. Bartelt and K. F. McCarty, *MRS Bulletin* **37**, 1158 (2012).

[30] Y. S. Dedkov and M. Fonin, *New Journal of Physics* **12**, 125004 (2010).

[31] A. T. N'Diaye, J. Coraux, T. N. Plasa, C. Busse, and T. Michely, *New Journal of Physics* **10**, 043033 (2008).

[32] P. Lacovig, M. Pozzo, D. Alfè, P. Vilmercati, A. Baraldi, and S. Lizzit, *Physical Review Letters* **103**, 166101 (2009).

[33] J. Coraux, A. T. N'Diaye, M. Engler, C. Busse, D. Wall, N. Buckanie, F.-J. M. z. Heringdorf, R. van Gastel, B. Poelsema, and T. Michely, *New Journal of Physics* **11**, 3006 (2009).

[34] P. Sutter, J. T. Sadowski, and E. Sutter, *Physical Review B* **80**, 245411 (2009).

[35] M. Gao, Y. Pan, L. Huang, H. Hu, L. Z. Zhang, H. M. Guo, S. X. Du, and H. J. Gao, *Applied Physics Letters* **98**, 033101 (2011).

[36] L. Gao, J. R. Guest, and N. P. Guisinger, *Nano Letters* **10**, 3512 (2010).

Chapter Two

Chemical vapour deposition of graphene on metallic substrates

In this chapter the process of growth of graphene on some metallic surfaces by means of chemical vapor deposition will be explained. We will describe the features of graphene prepared on nickel and copper surfaces and the properties of such interfaces, looking at their electronic and structural properties.

2.1 GROWTH OF GRAPHENE ON NICKEL SURFACE

METHOD OF GROWTH

The production of graphene monolayers on nickel was one of the first example of chemical vapor deposition of graphene on a metallic surface. The nickel was found to be catalytically active in splitting molecules of ethylene or propylene and produce on the metallic surface a monolayer of graphitic phase of carbon both on (100) and (111) oriented surfaces [1, 2, 3].

As evidenced by Nakamura and co-workers [4], the temperature of deposition plays a critical role in determining the crystalline phase that appears on the surface, which could be either carbidic or graphitic. This two phases have a different crystalline structure, as immediately results from a low energy electron diffraction (LEED) pattern, as in figures 2.1 and 2.2.

It was proven in [4] that the superstructure formed by carbides on Ni(111) is described by the superlattice matrix:

$$G = \begin{pmatrix} \frac{1}{2} + \frac{\sqrt{3}}{\gamma} & 1 \\ 1 - \frac{\sqrt{3}}{2\gamma} & 2 \end{pmatrix},$$

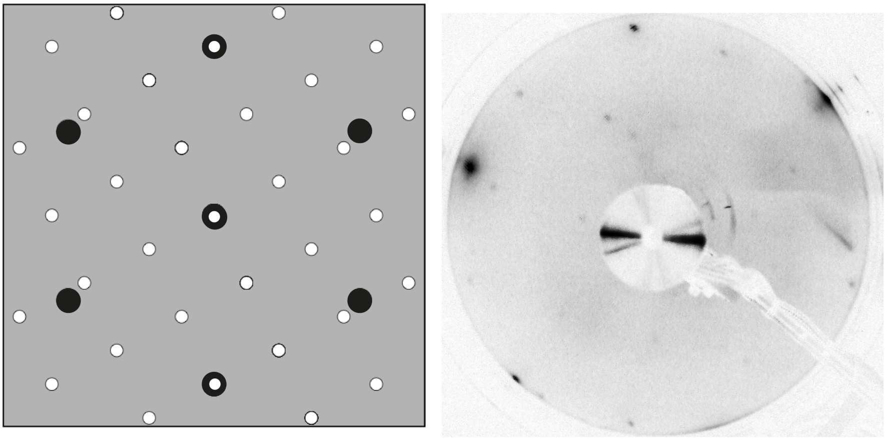

Figure 2.1: Left: simulation of LEED pattern of a single-domain carbides on Ni(111) surface. The black spots correspond to spots belonging to the Ni pattern. Right: LEED pattern (E_p = 70 eV) of single-domain carbides on Ni(111). Not every spot reported in the simulation is visible.

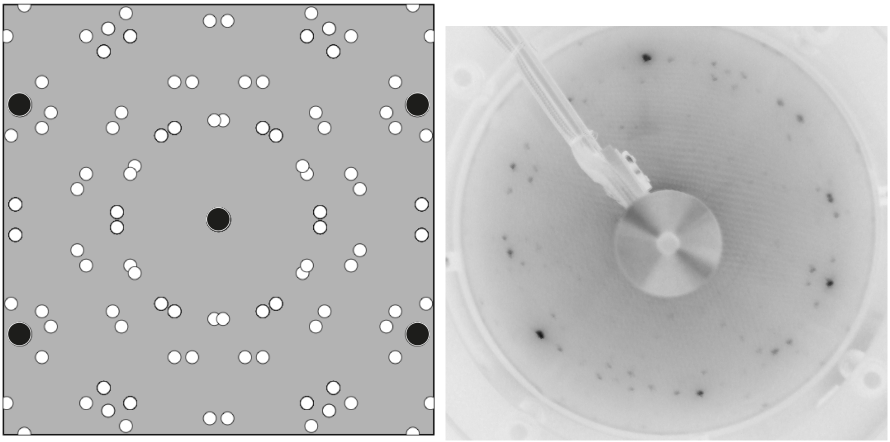

Figure 2.2: Left: simulation of LEED pattern of a six-domains carbides on Ni(111) surface. The black spots correspond to spots belonging to the Ni pattern. Right: LEED pattern ($E_p = 77eV$) of six domains carbides on Ni(111). Not every spot reported in the simulation is visible

with $\gamma = 5\sqrt{3}/9$. We have noticed that two possible LEED patterns can be obtained: a single-domain pattern (fig. 2.1) and a six-domain pattern (fig. 2.2), with a higher probability to observe the former.

For the Ni(111) surface, it has been shown that the formation of carbides starts at a temperature of about 420 K, while the graphitic layer formation can take place only at temperatures above 640 K. Since the temperature of decomposition of the carbide layer in a graphitic one is about 680 K, the two phases are competing in this range of temperatures, the temperature of deposition must be chosen quite far from the phase-transition temperature, in order to obtain only graphitc carbon deposited on the surface. A later work by Grüneis and co-workers [5], showed that with temperatures of deposition of about 820 K or higher, the presence of carbide components is drastically reduced in favor of the graphitic carbon.

On the other hand, it must be kept in mind that the higher is the deposition temperature, the higher is the chance that carbon deeply buried in the crystal bulk can segregate to the surface and form carbide layer, before the actual decomposition of the carbon-containing molecules starts. Furthermore, the high solubility of carbon and nickel [6, 7] is a critical issue to be taken into account already during the preparation of the clean surface, in order to preserve its catalytic properties. At the annealing temperature of nickel, the carbon buried into the bulk of the crystal indeed migrates to the surface quite easily.

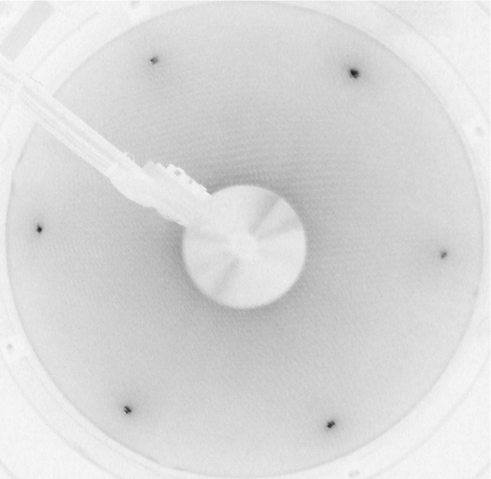

Figure 2.3: LEED pattern ($E_p = 77 eV$) of graphene on Ni(111) single crystal.

To remove carbon contaminations from the top-most layers of the surface of a Ni(111) single crystal, we prepared it in ultra high-vacuum (UHV) by cycles of Ar-sputtering (E_p = 1 keV) annealing at high temperature (1100 K). After each cycle the surface was exposed to oxygen (Messer, purity 99.995%) at a pressure of 2×10^{-8}mbar for 5 minutes, followed by an annealing at about 800 K, in order to remove the carbon present in the first layers of the crystal. The treatment was concluded with an annealing at 800 K in hydrogen (Messer, purity 99.995%, pressure 10^{-8}mbar) in order to remove traces of oxygen. After these treatment, a clean (111) LEED pattern was detected.

The Ni(111) single crystal surface was prepared by several cycles of argon ion sputtering (E_{ions} = 1 keV) and subsequent annealing at high temperature (1080 K). The graphene layer was grown *in-situ*, following the chemical vapor deposition (CVD) procedure described in the literature [2], employing of ethylene gas (purity 99.95%, Messer Gas) at 875 K. The surface was then cooled to room temperature.

CHARACTERISTICS OF THE GRAPHENE/NI(111) INTERFACE

The graphene/Ni(111) interface has been widely explored in the past years [8]. Among its remarkable characteristics, it is relevant to mention the spin-filtering properties, which was first predicted [9, 10] and subsequently experimentally proved [11].

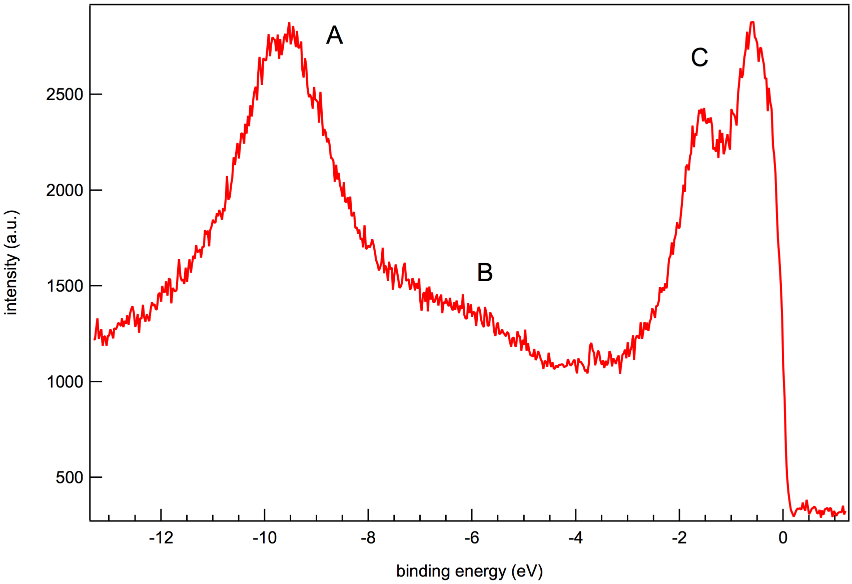

Figure 2.4: Valence band of the G/Ni(111) taken in normal emission (photon energy $h\nu$ = 40.8 eV, HeII).

The graphene/Ni(111) interface displays an almost perfect matching of the lattice parameters of the graphene and of the metal, which implies a matching of the two surface Brillouin zones. A first indication of the success of our growth protocol comes therefore from the observation of a p(1 × 1) LEED pattern, as shown in figure (2.3). Further confirmation comes from the valence band ultraviolet photoelectron spectrum of the interface, taken at normal emission and reporting the valence band, is shown in fig. 2.4. It is possible to identify three main features. The feature A corresponds to the π band of graphene, the feature B corresponds to the σ band of the graphene, respectively. The feature C is attributed to the $3d$ states of the nickel.

The position of the σ and π peaks in the spectrum results to be shifted of about 1.8 and 2.5 eV to higher binding energy compared to the case of valence band of graphite or (calculated) self-standing graphene [12]. This result points to an n-doped graphene and it is due to the strong interaction between the graphene and the nickel which produces a hybridization between the π states and the Ni 3d band. The angle-resolved photoemission experiments [8, 13] show that the Dirac cone shape is not preserved and the apex of the π band is not anymore at Fermi level around K point of the Brillouin zone (see fig. 2.5).

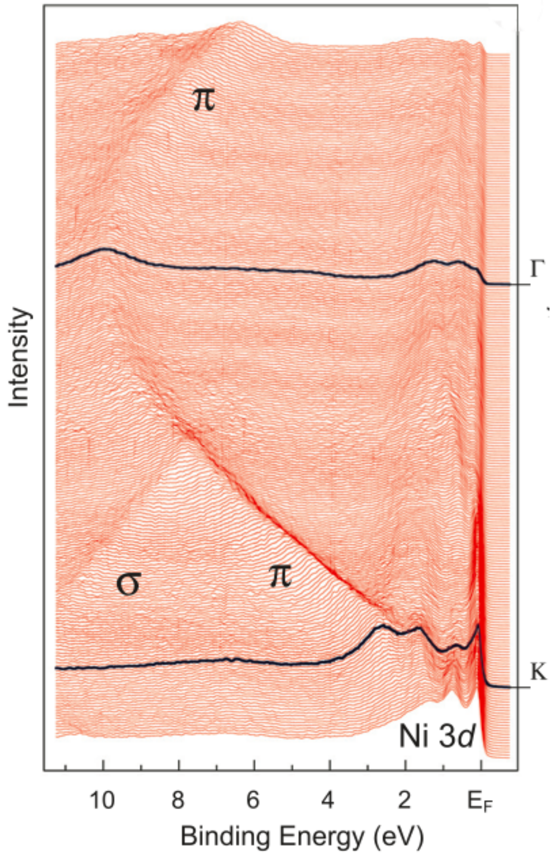

Figure 2.5: Angle-resolved photoemission of graphene on Ni(111), photon energy is 70 eV. The spectra at Γ and K points of the Brillouin zone are marked in black. After [8]. © 2010, IOP Publishing.

This interface has been proven to be extremely stable. The graphene passivates the underneath metal and protect it from the oxidation [11]. It can therefore be prepared *ex-situ*, transferred to atmospheric conditions and eventually introduced into a vacuum system again, where the original conditions can be restored by a mild annealing (400 K).

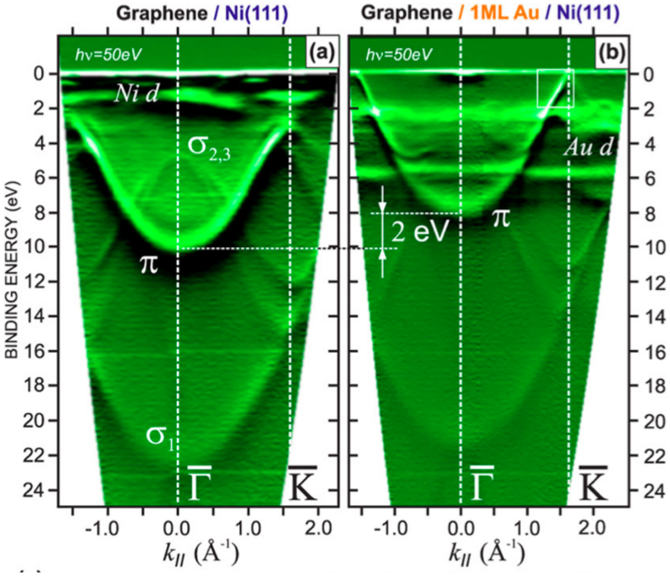

Figure 2.6: (a) Band-structure of G/Ni(111) and (b) of G/Au/Ni(111) systems, taken with an ARPES experiment ($h\nu$ = 50 eV), after [13]. © 2008 The American Physical Society.

THE GRAPHENE/AU/NI(111) INTERCALATED SYSTEM

In the previous section we have mentioned how the graphene on a Ni(111) crystal changes considerably its electronic properties. To study the electronic properties of graphene "as it is", any interaction with the substrate must be removed and this can be achieved with two different possibilities. The first one is the preparation of a suspended graphene, having thus some areas of the monolayer which are not interacting with any substrate. This strategy will be discussed later in this chapter. A second way is the intercalation of some atoms or molecules between the graphene and the metal. Among metal atoms, in the past, the intercalation of alkali metals [14], rare-earths [15], aluminum [16], copper [17], silver [18] and gold [13] has been investigated.

The latter is particularly relevant because Varykhalov and co-workers [13] proved that the intercalation of a monolayer of gold between the graphene and the nickel surface induces the shift of π bands closer to the Fermi level and established a situation that is very similar to the one of free-standing, not interacting graphene. The angle-resolved valence band data from these authors are shown in figures 2.6 and 2.7. The doping is removed, the hybridization of the carbon bands with the nickel 3d states vanishes and the Dirac cone linear shape is restored (positioned at K point of the

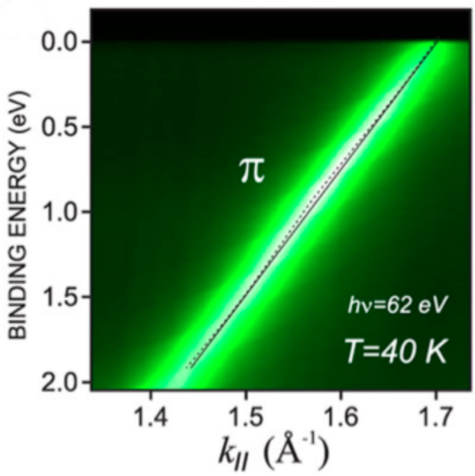

Figure 2.7: Detail of the Dirac cone in band-structure of G/Au/Ni(111) system, taken with an ARPES experiment ($h\nu$ = 62 eV), after [13]. © 2008 The American Physical Society.

Brillouin zone and at Fermi level). This system has been defined as *quasi-freestanding graphene*. A similar result has been achieved with the intercalation of gold underneath epitaxial graphene, grown on a SiC crystal surface [19].

The preparation of such *quasi-freestanding* sample is as follows. The graphene on Ni(111) was prepared as described in the previous section. A monolayer of Au has been evaporated by a Knudsen-cell evaporator kept at 1450 K, while the sample was held at room temperature. The deposition rate of the evaporator was previously calibrated by means of a quartz microbalance. The sample was then annealed for a short time (15 min.) at a temperature of about 550 K. The annealing causes the diffusion of gold atoms along the graphene surface and to the graphene defects, where intercalation through the graphene layer can take place [13]. We shall label this intercalated system as Graphene/Au/Ni(111).

The successful achievement of the intercalation is confirmed by the valence band photoemission spectrum UPS, as reported in figure 2.8 The valence band spectra, taken at normal emission with a photon energy of 40.8 eV, were acquired before (lower spectrum) and after (upper spectrum) the annealing process. It is possible to note a shift in the position of the peak attributed to the π band of graphene, which is indeed at about -10 eV binding energy in the red spectrum (not intercalated) while it moves to -8 eV in the green spectrum, indicating how the graphene is less bond to the substrate underneath. Comparing this shift with the band structure acquired in

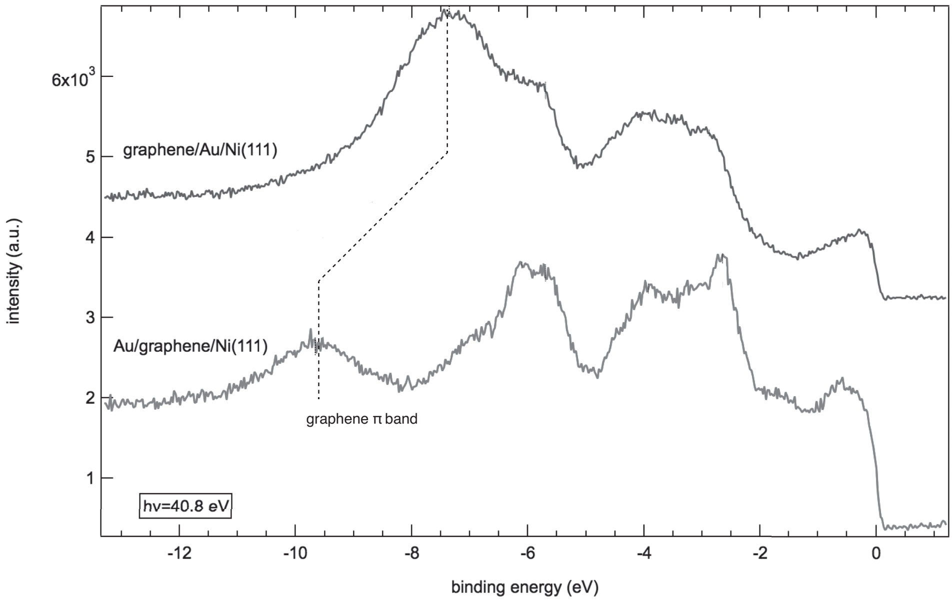

Figure 2.8: Angle-integrated valence band spectra of Au on G/Ni(111) and of the intercalated structure G/Au/Ni(111), acquired by UPS (photon energy is 40.8 eV). The lower and upper curves represent respectively the spectra acquired before and after the annealing. The dashed line indicates the shift of the peak of graphene π band due to the intercalation of Au atoms between the graphene and the nickel substrate.

ARPES (figure 2.6), we interpret this observation as the complete intercalation of the Au monolayer between the graphene and the nickel, assumption that is corroborated by the conclusions already drawn in previous papers [20, 13].

2.2 GROWTH OF GRAPHENE ON COPPER SURFACES

CVD growth of graphene on copper has revealed itself as one of the most promising and high-yield techniques for the production of graphene for technological applications [21, 22]. Unlike with nickel, carbon has a very low miscibility with copper, implying that, during the CVD process, the graphene is formed solely by the decomposition of the hydrocarbon gases. Furthermore, the process is self-stopping once a layer of graphene is fully covering the metal [22]. However, since copper has lower reactivity to hydrocarbons than nickel, the temperature required for the growth is much higher (1200 K, very close to the melting point of copper) [22].

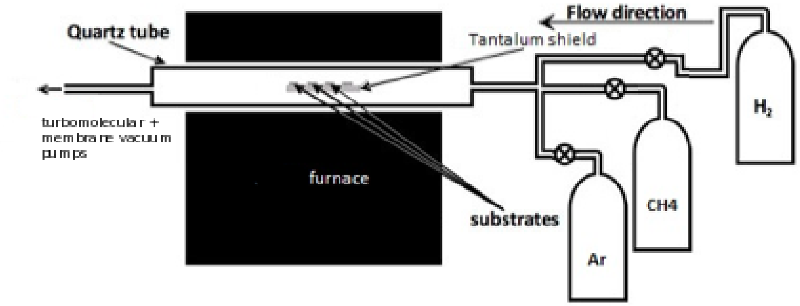

Figure 2.9: Schematic of the CVD setup for graphene growth (courtesy of Taco de Wolff).

EXPERIMENTAL PROCEDURE

We have grown graphene both on copper foil and on Cu(111) single crystal, following the parameters reported in [21]. The growth took place in a homebuilt, quartz-tube vacuum furnace, where the base pressure was about 10^{-5}mbar and the maximum temperature reachable was 1300 K. A schematic of the furnace is depicted in figure 2.9 The vacuum furnace is equipped with several gas lines and with a liquid-nitrogen trap, whose function is to remove unwanted residual components (mainly water) from the gases used in the CVD growth process.

The single-crystal Cu(111) surface was priorly prepared in UHV with several cycles of sputtering (Ar ions, $E_p = 1\ keV$) and annealing (800 K). The cleanliness was verified with LEED. The sample was then transferred into the CVD setup furnace. Since a layer of native oxide was formed during the transfer of copper in air, an annealing at a temperature ranging between 1180 and 1250 K in hydrogen flow (0.5 mbar) was used in reduce the sample surface and remove the copper oxide. Subsequently, the sample was exposed to a mixture of hydrogen (0.5 mbar, MesserGas, purity 99.999%) and methane (0.5 mbar, MesserGas, purity 99.995%) for a time ranging between 2 and 4 minutes. This ensured the coverage of the surface with a graphene layer. The sample was then cooled down in a Ar atmosphere (99.999% purity, MesserGas, pressure 0.1 mbar) with a initial rate of 10 K/min (in the interval 1200-750 K) and later with a rate of 5 K/minute (in the range 750-350 K).

The copper foil surface was prepared by etching in a 0.25M solution of H_2SO_4 for 5 minutes and subsequently rinsed in milliQ water. The sample was then rinsed in

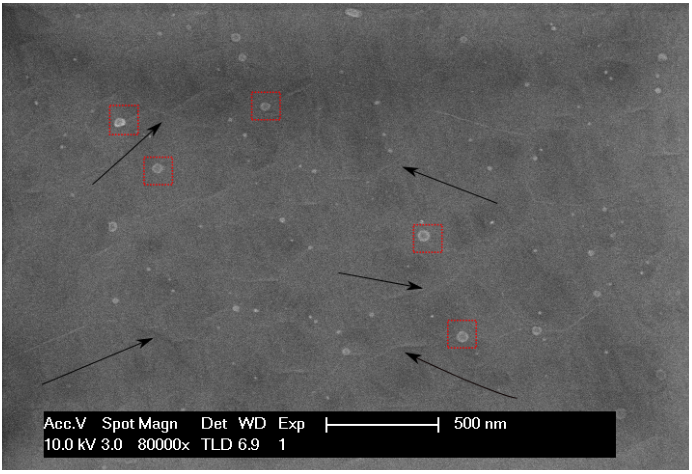

Figure 2.10: SEM image of graphene on Cu foil. The arrows are pointing to the graphene wrinkles on the surface. The white spots, in frames, are impurities deposited during the growth process due to re-evaporation of quartz tube at high temperature.

ethanol and dried with argon flow, before being introduced in the furnace: there it underwent the same H_2 treatment and graphene growth protocol as described above for the single-crystal substrate. The deposited graphene was inspected with a Scanning Electron Microscope (Tescan Lyra dual beam instrument, operated at 30 kV), as reported in figure 2.10. Unlike in the case of growth on nickel, the surface lattice parameters of graphene and copper are quite different (2.46 Å and 2.55 Å – for the {111} orientation – respectively). This difference, in combination with different dilatation coefficients, produces wrinkles and defects on the surface during the cooling after the deposition. Thus, the presence of graphene is revealed by the wrinkles that are present on the surface, marked with black arrows in fig.2.10. We also observe the presence of several white particles (highlighted by a frame in figure 2.10), which we attribute to contamination from the quartz tube. We could indeed reduce the number of these white particles by using a tantalum shield around the copper substrates, but not completely eliminate them. In chapter 5 we will show a more detailed characterization of electronic structure of the graphene on Cu(111) single crystals, in order to understand more deeply about the interaction of graphene with such surface.

2.3 TRANSFER OF GRAPHENE BY MEANS OF POLYMERIC STAMP

The growth of graphene on copper can be successfully combined with transfer to other surfaces with the help of a polymeric stamp (see for ex. reference [23]).

Such a transfer can be used *e.g.* in the production of a transistor, where it is necessary to have the graphene deposited on an insulating substrate. We have transferred graphene grown by CVD on copper foil onto silicon oxide and onto thin Au film on a quartz crystal for measurements of nanotribological properties on a micro-balance quartz (chapter 7).

A scheme of the transfer process is reported in fig. 2.11. The graphene was grown on copper foil as explained in the previous section. Firstly,a Polydimethylsiloxane (PDMS) stamp was pressed onto the graphene surface to establish a bond between the two, then the copper foil was etched away in a solution of $FeCl_3$ (iron chloride) in water, with a concentration of 100 g/l. The sample was subsequently rinsed twice in demi-water in order to remove any remaining traces of the etchant. Finally, the graphene layer was deposited onto the chosen substrate by mildly pressing the PDMS stamp onto it. The transfer process induces some damage in the graphene layer which can be visualized by optical microscopy if graphene is transferred onto a silicon wafer covered by a proper thickness of silicon oxide to produce an interference effect [24]. We used a n-doped silicon wafer, covered by a 300 nm silicon oxide layer.

Figure 2.12 shows an overview optical micrograph (taken by Taco de Wolff). Micrographs taken at larger magnification like the one shown in 2.13 demonstrate that the graphene layer is not continuous. The brighter areas, pinpointed by black arrows, are identified as cracks in the graphene due to the transfer process. Wrinkles in the graphene can also be seen as well as lighter spots (highlighted by the frames) identified as impurities accumulated during the transferring process.

We also characterized these same graphene transferred onto SiO_2 by Raman spectroscopy because, as explained below, position and intensity of the Raman peaks of a graphene layer give information can differentiate between single, double or multilayer graphene and reveal the presence of defects [25, 26, 27].

A typical raman spectrum taken on our samples is reported in figure 2.14. The exciting photon wavelength is 532 nm.

The peaks shown in the Raman spectrum correspond to as many active phonon modes, as depicted in figure 2.15: a D band (around 1370-1400 cm^{-1}), a G band (around 1600 cm^{-1}) and a G′ band (around (2700-2800 cm^{-1}).

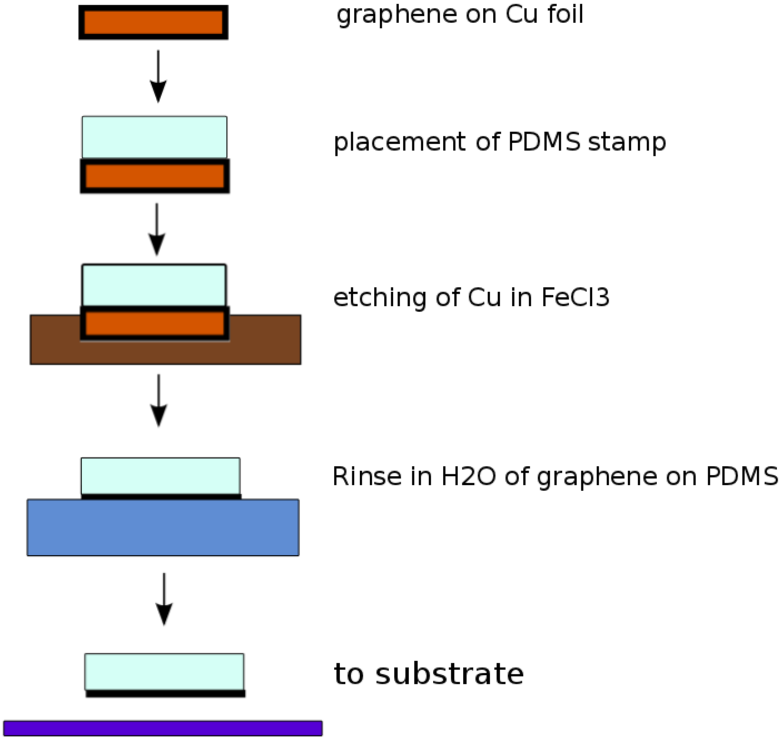

Figure 2.11: Schematic of the process of transferring of graphene/Cu foil to an other substrate by means of PDMS stamp.

The G band is associated with a degeneracy of the in-plane transversal and longitudinal optical phonons around the centre of the Brillouin zone; it is the only band coming from a first-order scattering process. The D and G′ bands are due to second-order scattering processes involving scattering at the K point of the Brillouin zone. Hence, these phonon modes have wave-vectors $q \sim 2k$, where k is the wave vector associated with the electronic states excited by the impinging photons (24, 27). In the case of D band, the impinging photon excites an electron in the conduction band that is subsequently inelastically scattered by an in-plane, transverse optical phonon and by the defects and edges in the lattice (see lower panels in figure 2.15). Therefore, the intensity of the D band is a fingerprint of the amount of defects (or edges) present in probed area, and therefore gives an indication about the quality of the graphene film. The mechanism that leads to appearance of peak G′ is related to the double and triple

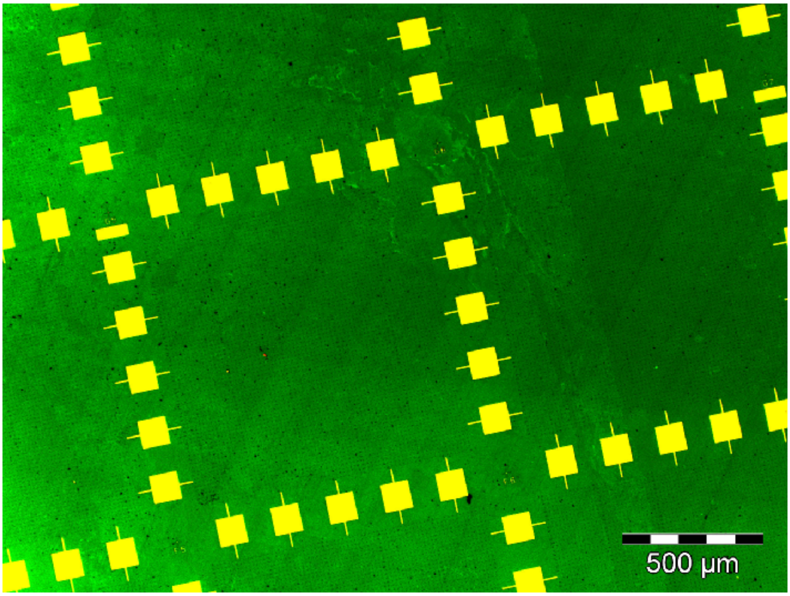

Figure 2.12: Optical image of a graphene layer on silicon oxide (300 nm)/silicon wafer. The bright squared markers were already present on the original substrate and acted as position reference.

scattering process of excited electrons with in-plane optical transverse mode phonons as sketched in figure 2.15. The shape of the G′ band is connected to the number of graphene monolayers which are deposited on the surface [27, 25]. The Raman spectra acquired on our samples can be fitted with a single lorentzian peak, indicating that the surface is covered, mainly, by a single layer of graphene [27]. Moreover, the spectrum of samples we have produced shows a relevant D band, confirming the presence of defects already seen in the optical microscopy. A ratio $I_D/I_G \simeq 0.3$ is detected. By following the approach described in [28], we can estimate that the average distance L_a between two defects in the graphene layer is about 15-20 nm.

2.4 TRANSFER OF GRAPHENE ONTO TEM GRIDS

The possibility of producing large flakes of graphene by means of CVD growth on copper and the successful achievement of transfer with the help of polymeric stamps opens the way to producing truly free standing graphene by transferring the graphene grown on copper foil onto special grids for Transmission Electron Microscopy (TEM).

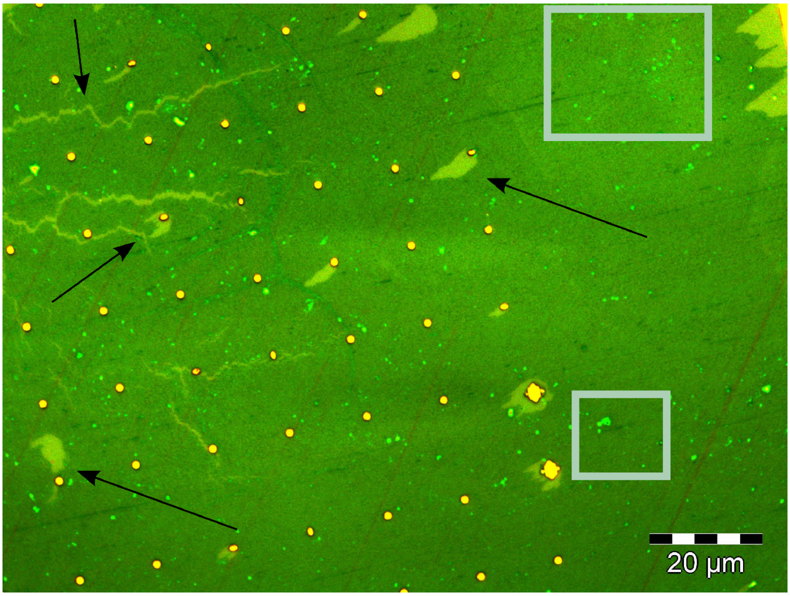

Figure 2.13: Optical microscopy image of CVD grown graphene transferred onto a silicon oxide (300 nm)/silicon wafer. The area with higher contrast, pinpointed by black arrows, are identified as cracks in the graphene layer. The brighter spots (highlighted by the frames) are attributed to impurities resulting from the transfer process).

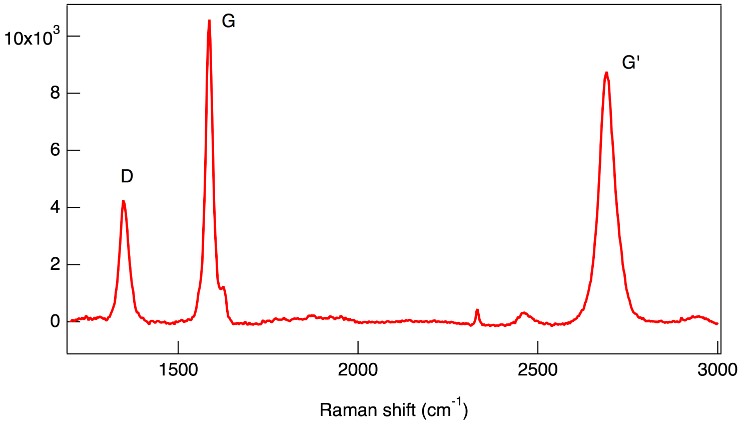

Figure 2.14: Raman spectrum of graphene on a SiO_2(300nm)/Si wafer. The exciting wavelength is 532 nm. The peaks just below 2500 cm^{-1} are artifacts of the detector.

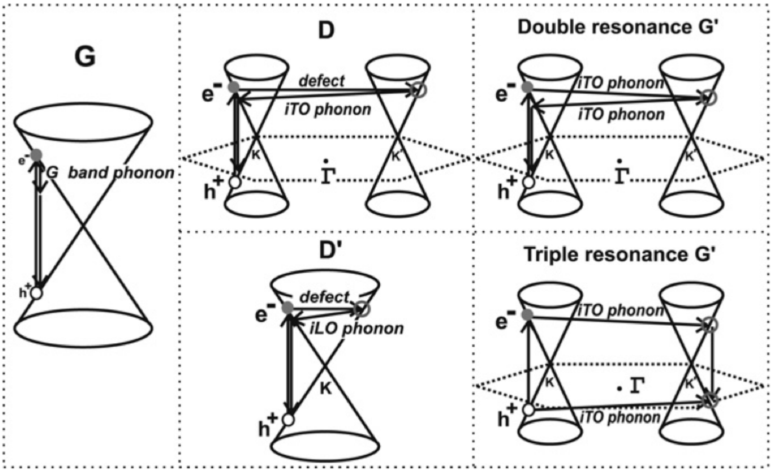

Figure 2.15: Overview of Raman-active modes and corresponding peaks in a raman spectrum for graphene samples [27]. © 2009 Elsevier.

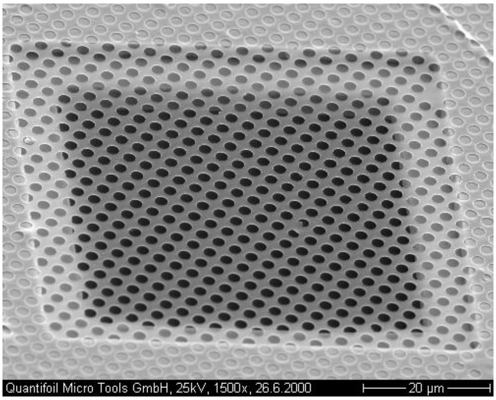

Figure 2.16: SEM image of a *Quantifoil*$^{®}$ 2/2 substrate used for deposition of free-standing graphene. Image taken from `http://www.quantifoil.com`

Such samples allow measuring the band structure of the graphene only, without the contributions/influence coming from a substrate as will be illustrated in chapter 6. We chose Quantifoil®2/2 TEM grids for our experiments. These substrates, for which an SEM micrograph is shown in figure 2.16, consist in a Au-mesh with a spacing of 100 μm onto which a 9 nm thick amorphous carbon membrane has been

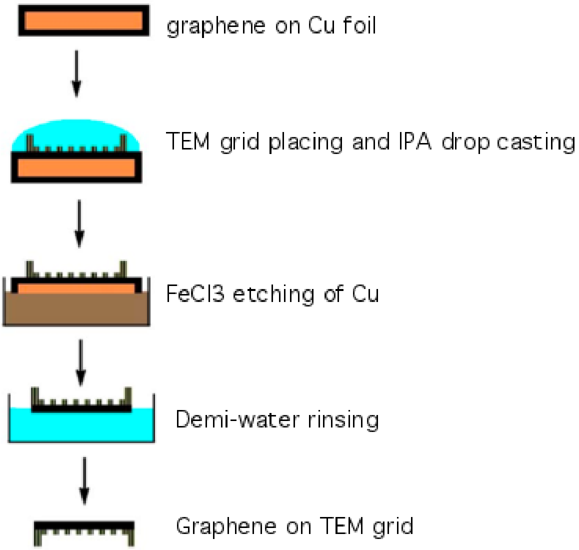

Figure 2.17: Steps of protocol for transferring graphene from copper foil to TEM grid. Adapted from [29]. © 2010 American Institute of Physics.

deposited. This membrane is patterned with 2 μm diameter circular holes with a spacing of 2 μm.

Since we wanted to avoid as much as possible the impurities found in the case of the transfer with the PDMS stamp described above, we decided to prepare the free-standing graphene samples following and adapting the protocol described in [29]. This procedure does not call for a stamp and proceeds through the steps depicted in figure 2.17. The graphene was grown on copper foil as explained earlier. A Quantifoil®2/2 TEM grid was then laid down on the sample, with the amorphous carbon membrane touching the graphene. A drop of 2-propanol alcohol (IPA) was depositedon the sample which, while evaporating, caused the graphene to bind to the carbon membrane of the Quantifoil®2/2 TEM grid. Then the copper foil was etched away in a solution of $FeCl_3$ in water, with a concentration of 100 g/liter. The sample was subsequently rinsed twice in demi-water in order to remove any remaining traces of the etchant. Finally the sample was annealed at 390 K for 5 minutes in an oven (at atmospheric pressure) in order to remove traces of water. The samples were inspected by means of scanning electron microscopy and a typical micrograph is shown in Figure 2.18. As for the bare grid shown in Fig. 2.16, it is possible to distinguish the holes

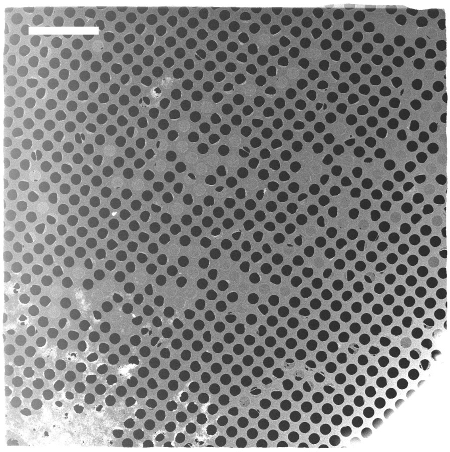

Figure 2.18: SEM overview image of a Quantifoil with some deposited graphene. The scale bar in the image is 10 μm. The primary energy of the electron beam is 10 kV.

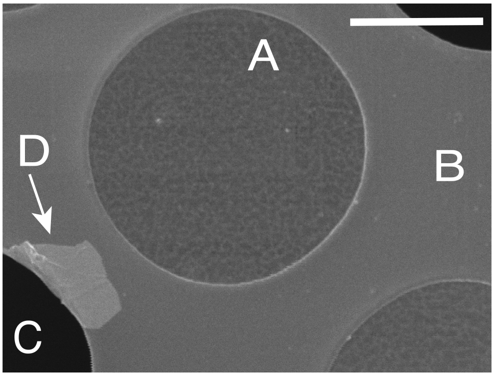

Figure 2.19: SEM image of a hole of the amorphous carbon membrane Quantifoil® where the graphene layer is suspended. See in the text for explanation of the various features. The scale bar is 1 μm.

in the carbon membrane but here about 50 % are filled with graphene and easily detectable.

If we take a closer look at the graphene-covered membrane as shown in figure 2.19, we can easily distinguish the holes that are covered with a free-standing layer of graphene (A) from those which are empty (C) because the former show a different contrast as well as white spots corresponding to impurities present on the graphene layer. The area marked with B is the supporting amorphous carbon grid. The graphene layer can break down during the transfer - the letter D marks an area where the ruptured graphene layer has folded over on the supporting grid.

In chapter 6 we shall provide a fully-featured characterization of these samples, exploring both electronic and structural properties of the suspended graphene produced.

REFERENCES

[1] M. Eizenberg and J. M. Blakely, *The Journal of Chemical Physics* **71**, 3467 (1979).

[2] C. Oshima and A. Nagashima, *Journal of Physics: Condensed Matter* **9**, 1 (1997).

[3] A. Nagashima, K. Nuka, K. Satoh, H. Itoh, T. Ichinokawa, C. Oshima, and S. Otani, *Surface Science* **287-288**, 609 (1993).

[4] J. Nakamura, H. Hirano, M. Xie, I. Matsuo, T. Yamada, and K. Tanaka, *Surface Science Letters* **222**, L809 (1989).

[5] A. Grueneis, K. Kummer, and D. V. Vyalikh, *New Journal of Physics* **11** (2009).

[6] B. S. Berry, *Journal of Applied Physics* **44**, 3792 (1973).

[7] J. J. Lander, H. E. Kern, and A. L. Beach, *Journal of Applied Physics* **23**, 1305 (1952).

[8] Y. S. Dedkov and M. Fonin, *New Journal of Physics* **12**, 125004 (2010).

[9] V. Karpan, G. Giovannetti, P. Khomyakov, M. Talanana, a. Starikov, M. Zwierzycki, J. van Den Brink, G. Brocks, and P. Kelly, *Physical Review Letters* **99** (2007).

[10] V. M. Karpan, P. A. Khomyakov, A. A. Starikov, G. Giovannetti, M. Zwierzycki, M. Talanana, G. Brocks, J. Van Den Brink, and P. J. Kelly, *Physical Review B* **78**, 195419 (2008).

[11] Y. S. Dedkov, M. Fonin, and C. Laubschat, *Applied Physics Letters* **92**, 052506 (2008).

[12] A. H. Castro Neto, F. Guinea, N. M. R. Peres, K. S. Novoselov, and A. K. Geim, *Review of Modern Physics* **81**, 109 (2009).

[13] A. Varykhalov, J. Sánchez-Barriga, A. Shikin, C. Biswas, E. Vescovo, A. Rybkin, D. Marchenko, and O. Rader, *Physical Review Letters* **101**, 1 (2008).

[14] A. Nagashima and N. Tejima, *Physical Review B* **50**, 17487 (1994).

[15] A. M. Shikin, D. Farias, Das, V. K. Adamchuk, and K.-H. Rieder, *Surface Science* **424**, 155 (1999).

[16] E. N. Voloshina, a. Generalov, M. Weser, S. Böttcher, K. Horn, and Y. S. Dedkov, *New Journal of Physics* **13**, 113028 (2011).

[17] Y. Dedkov, A. Shikin, V. Adamchuk, S. Molodtsov, C. Laubschat, A. Bauer, and G. Kaindl, *Physical Review B* **64**, 1 (2001).

[18] D. Farias, A. M. Shikin, K. H. Rieder, and YS, *Journal of Physics: Condensed Matter* **11**, 8453 (1999).

[19] I. Gierz, T. Suzuki, R. T. Weitz, D. S. Lee, B. Krauss, C. Riedl, U. Starke, H. Höchst, J. H. Smet, C. R. Ast, and K. Kern, *Physical Review B* **81**, 1 (2010).

[20] A. G. Starodubov, M. A. Medvetskii, A. M. Shikin, G. V. Prudnikova, and V. K. Adamchuk, *Physics of the Solid State* **44**, 681 (2002).

[21] X. Li, W. Cai, J. An, S. Kim, J. Nah, D. Yang, R. Piner, A. Velamakanni, I. Jung, E. Tutuc, S. K. Banerjee, L. Colombo, and R. S. Ruoff, *Science* **324**, 1312 (2009).

[22] C. Mattevi, H. Kim, and M. Chhowalla, *Journal of Materials Chemistry* **21**, 3324 (2011).

[23] S. Bae, H. Kim, Y. Lee, X. Xu, J.-S. Park, Y. Zheng, J. Balakrishnan, T. Lei, H. Ri Kim, Y. I. Song, Y.-J. Kim, K. S. Kim, B. Ozyilmaz, J.-H. Ahn, B. H. Hong, and S. Iijima, *Nature Nanotechnology* **5**, 574 (2010).

[24] P. Blake, E. W. Hill, A. H. Castro Neto, K. S. Novoselov, D. Jiang, R. Yang, T. J. Booth, and A. K. Geim, *Applied Physics Letters* **91**, 063124 (2007).

[25] A. C. Ferrari, J. C. Meyer, V. Scardaci, C. Casiraghi, M. Lazzeri, F. Mauri, S. Piscanec, D. Jiang, K. S. Novoselov, S. Roth, and A. K. Geim, *Physical Review Letters* **97**, 187401 (2006).

[26] A. Ferrari, *Solid State Communications* **143**, 47 (2007).

[27] L. M. Malard, M. Pimenta, G. Dresselhaus, and M. S. Dresselhaus, *Physics Reports* **473**, 51 (2009).

[28] M. M. Lucchese, F. Stavale, E. H. M. Ferreira, C. Vilani, M. V. O. Moutinho, R. B. Capaz, C. A. Achete, and A. Jorio, *Carbon* **48**, 1592 (2010).

[29] W. Regan, N. Alem, B. Alemán, B. Geng, Ç. Girit, L. Maserati, F. Wang, M. Crommie, and A. Zettl, *Applied Physics Letters* **96**, 113102 (2010).

Chapter Three

Final-state effects in photoemission experiments from graphene on Ni(111)

Photon-energy dependent photoemission experiments using high harmonic radiation as a tunable photon source on epitaxially grown graphene on a Ni(111) substrate are presented. A resonance in the photoemission cross section for the σ and π states of graphene was observed and compared to a simple model for the determination of photoemission cross sections of free standing graphene, pointing out the role of the interaction of graphene with the nickel substrate.

The work described in this chapter was reported in:
T. Haarlammert, L. Bignardi, C. Winter, G. Fecher, P. Rudolf, H. Zacharias, *Final-state effects in photoemission experiments from graphene on Ni(111)*, to appear in European Physical Journal B (2013).

3.1 INTRODUCTION

Graphene has attracted considerable scientific interest and attention in the last years. Its peculiar 2D crystalline lattice is responsible for several surprising electronic and structural properties that have been widely investigated [1, 2, 3]. The relevant electrical and optical properties are caused by the π band dispersion around the K point of the Brillouin zone, which is linear when the graphene is not interacting with a substrate [4]. However, the technological future exploitation of graphene requires a detailed knowledge of the graphene-metal interfaces, whose electronic properties can significantly differ from those of free-standing graphene, as a consequence of the interaction with the metal [5, 6].

Ultraviolet photoelectron spectroscopy (UPS) is a tool widely used for the investigation of the electronic structure of this material [7] and its interaction with the underlying substrate. In this work we apply high harmonic generation of ultrashort laser pulses as a tunable and polarized table-top photon source in the extreme ultraviolet (EUV) spectral region. The tunability of this photon source enables the measurement of relative photoemission (PE) cross sections of various occupied electronic states, employing photons with an energy between of $h\nu$ = 23.6 eV and 53.6 eV. The PE spectra of the valence band of graphene grown on a Ni(111) substrate by chemical vapour deposition (CVD) have been collected and a distinct profile for the PE cross section was observed for the σ and the π bands of the graphene. These experimental results were compared to tight-binding calculations of the band structure.

3.2 EXPERIMENTAL

Frequency conversion by high harmonic generation (HHG) of femtosecond visible laser pulses affords a table-top source of stepwise tunable extreme ultraviolet (EUV) radiation. In noble gases like argon odd harmonic orders of the fundamental photon energy are generated, providing EUV pulses with femtosecond duration [8, 9]. Laser intensities on the order of 10^{13} - 10^{14} W/cm^2 are required to generate high harmonics in noble gases.

In the setup employed for this experiment (shown in figure 3.1), a Ti:sapphire laser system is used to generate ultrashort laser pulses with a pulse energy of about 1 mJ, a pulse duration of 30 fs [10] at 6 kHz repetition rate. These ultrashort pulses are focussed onto an Ar gas target similar to the set-up of Spielmann *et al.* [11] for nonlinear frequency conversion. In the present experiments argon was employed as

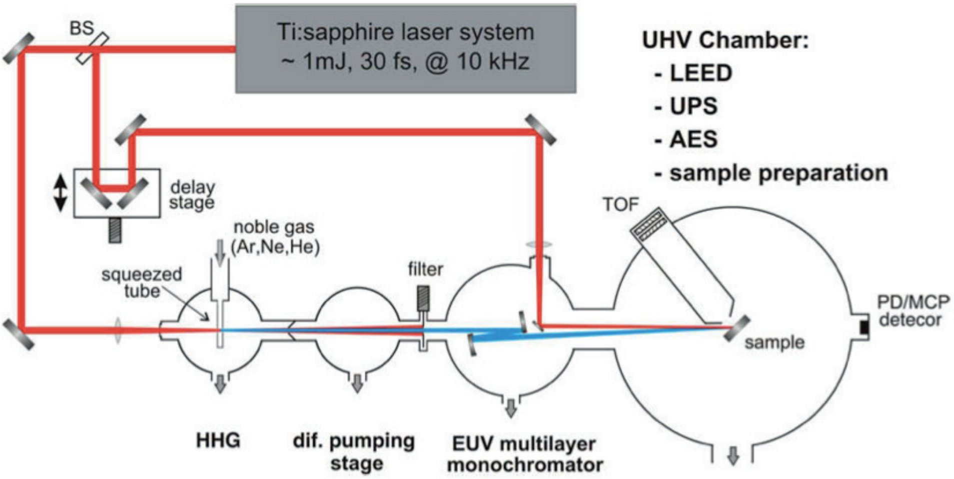

Figure 3.1: Schematic of the setup employed for the experiments described in the chapter. Adapted from [9]. © 2006 Elsevier.

nonlinear medium, since it is the most efficient target for EUV photon energies between hν = 20 eV and 55 eV [9]. By rotating the direction of the linear polarization of the fundamental, the polarization of the harmonics is changed accordingly. A thin Al foil (100 nm thick) was used to block the fundamental light and additionally to block residual gas flow from the generation process. The foil is nearly transparent for photon energies between hν = 20 and 70 eV and it can therefore be used to separate the generated EUV radiation from the fundamental beam. The odd harmonic orders of the fundamental photon energy are generated simultaneously. Therefore, a toroidal grating was used to select a specific harmonic order and thus to change the energy of the photons employed for the photoemission experiment.

The PE spectra were acquired in an ultrahigh vacuum (UHV) chamber with a base pressure of 2×10^{-10} mbar. The process of deposition on the Ni(111) substrate was carried out as described in chapter 2. Due to the almost perfect matching of Ni(111) and graphene surface lattice parameters, a $p(1 \times 1)$ pattern was observed with a low energy electron diffraction (LEED). Ultraviolet photoelectron spectroscopy (UPS) measurements using a commercial He-II discharge lamp and electron analyzer (Focus CSA 300) show at normal emission in an angle-integrated UPS spectrum, the π and σ bands of graphene, and thereby confirm the presence of graphene on the surface.

Photoemission spectra using the HHG source were acquired by means of a time-of-flight (TOF) detector. The electron flight time was measured in a field-free drift tube and the electrons were detected using a micro channel plate (MCP) detector. A total energy resolution of about 0.5 eV was achieved, limited by the finite energy bandwidth of the generated harmonics and by the time resolution of the TOF spectrometer. The EUV photon beam arrived on the sample with at an incidence angle of ca. $\vartheta = 55°$ with respect to the surface normal. All spectra shown here were taken at normal emission, that is at the Γ point of the Brillouin zone of the graphene. The angular acceptance of the spectrometer is ±2.5°, which corresponds to an integration over $\Delta k_{||} = 0.37\,\text{Å}^{-1}$ at $E_{kin} = 39.2\,\text{eV}$.

3.3 FINAL-STATE EFFECTS IN CROSS SECTIONS PROFILES

Fig.3.2 presents photoemission spectra from graphene on Ni(111) taken with photon energies between $h\nu = 23.4$ eV (15th harmonic order) and 54.6 eV (35th harmonic order). The spectra were normalized to the secondary photoelectron background because of the unequal conversion efficiencies for different harmonic orders. In fig. 3.2-(a) spectra taken with $\hat{p}$-polarized EUV radiation are reported. The zero binding energy (E_B) has been set to the Fermi level E_F. The most prominent structure derived from the *3d* band of Ni can be recognized at about 1 eV below the Fermi level [12]. Additional structures are evident at binding energies of $E_B = -5.5$ eV and $E_B = -11$ eV and can be assigned to emission from the graphene σ- and π bands, respectively. The position of the π states in the photoemission spectra at normal emission is shifted by about 3 eV towards higher E_B with respect to the graphene not interacting with any substrate [4]. The Ni substrate induced a shift in agreement with what was observed in earlier experiments [13, 14]. Fig. 3.2-(b) shows analogous photoemission spectra taken with $\hat{s}$-polarized light, where one clearly distinguishes emission from Ni *3d* bands, but no features belonging to the graphene π and σ bands. On the contrary, it is not possible to observe the structures belonging to π and σ bands of graphene, which are visible in photoemission with $\hat{p}-$polarized light only. This is due to the geometry of graphene bands and their selection rules for the photoionization [15, 16].

The photoemission spectra taken with both $\hat{s}$- and $\hat{p}$-polarized light show important changes in intensity, related to the PE cross sections. In our experimental set-up the photon flux cannot be recorded while collecting the photoemission spectra. Since the conversion efficiency strongly depends on the harmonic order selected for photoemission measurements, the spectra have to be normalized to the secondary

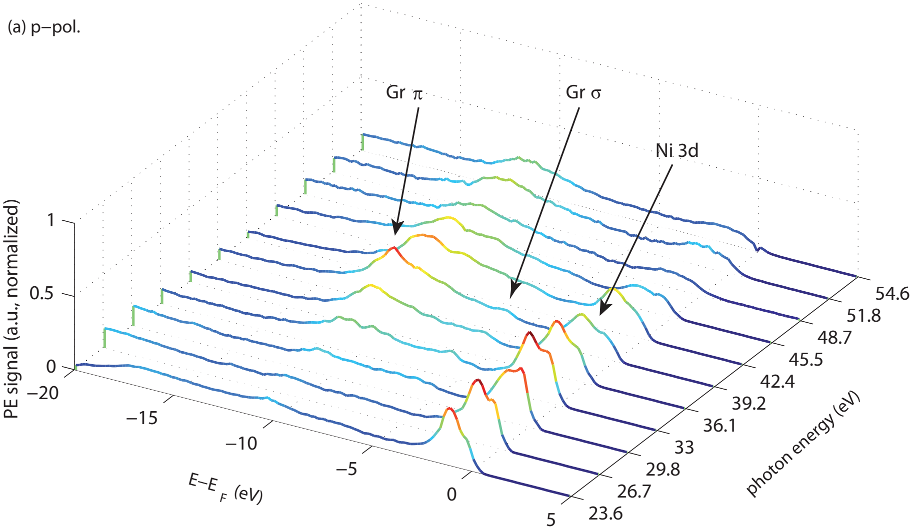
(a) p−pol.

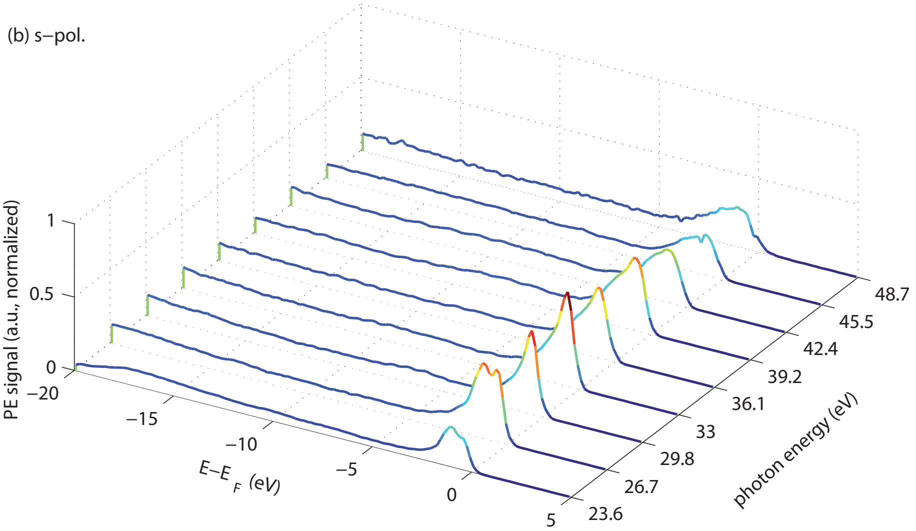
(b) s−pol.

Figure 3.2: Photoemission spectra of on graphene on Ni(111) with (a) $\hat{p}$ and (b) $\hat{s}$-polarized light, collected at normal emission, with various photon emission, as indicated.

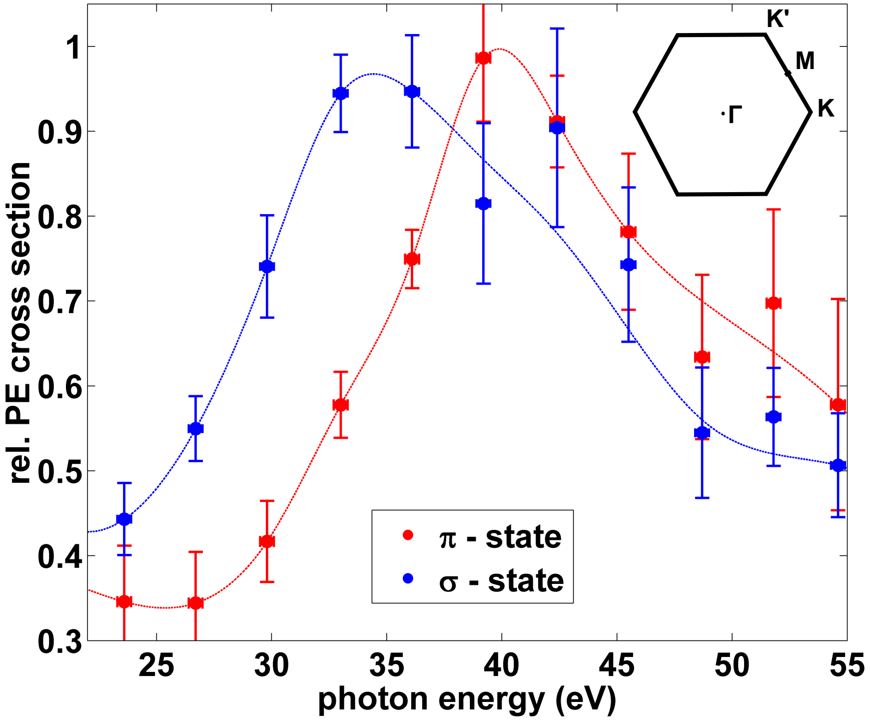

Figure 3.3: Experimentally determined relative photoemission cross sections for the graphene σ and π bands, measured with various photon energies. The dashed lines are guides for the eye.

photoelectron background to compare spectra taken at different photon energies. Therefore only the relative photoemission cross section can be measured with the method we employed [17]. Fig. 3.3 shows the relative photoemission cross section of the graphene σ and π bands measured with various photon energies, as derived from the spectral intensities of figure 3.2 (a). The profile of the photoemission cross section dependence on the photon energy of both bands shows a broad resonance. For the π state the maximum PE cross section in the experimentally accessible energy region is reached at a photon energy of $h\nu = 39.2\,\text{eV}$, while that of the σ state occurs approximately at $h\nu = 34.0\,\text{eV}$. The two resonances are therefore spaced about 5 eV apart on the photon energy scale; this difference agrees very well with the difference in binding energy between π and σ states. Therefore we suggest that the maximum

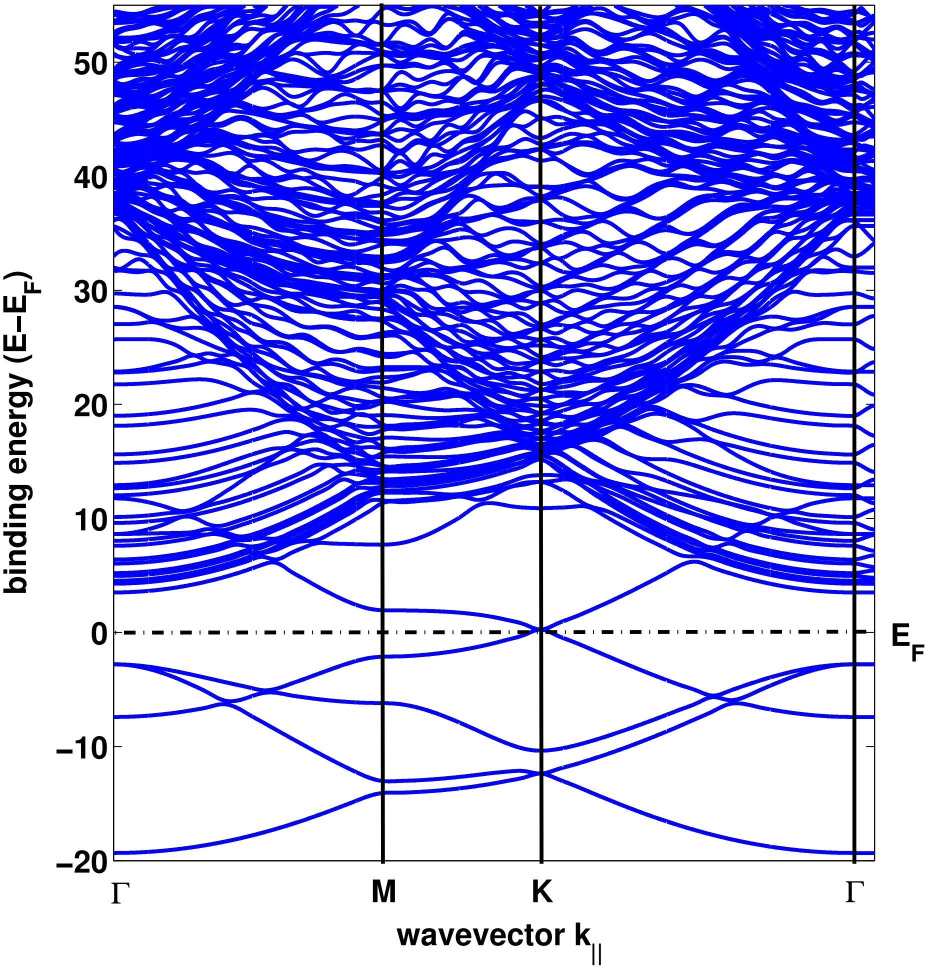

Figure 3.4: Tight-binding simulation of the electronic band structure of free standing graphene

in the photoemission cross section for both bands is due to an increased density of final states.

3.4 INTERPRETATION OF CROSS SECTIONS PROFILES

To understand the presence of such cross section maxima, the band structure for occupied and unoccupied states of a free-standing graphene was calculated with a tight-binding approach using standard methods. This includes atomic potentials with full crystal symmetry, Slater exchange and gradient corrections of the electron density. The results of this calculation are shown in figure 3.4. The σ and π bands are found, at the Γ point of the Brillouin zone, at binding energies of $E - E_F = -4.8$ eV and $E - E_F = -7.4$ eV, respectively. The Dirac point is observed at the K point of the Brillouin zone and the Fermi level is exactly crossing the vertex of the Dirac cone. The numerical results of the occupied band structure are in good agreement with literature data [18, 19, 4]. The distinctive feature of our calculation is that the energetically high unoccupied electronic states that have been taken into account because transitions from the π and σ bands were excited by high photon energies in the experiment. The unoccupied band structure has been calculated up to 55 eV above the Fermi level. A free electron-like dispersion is observed for most of the unoccupied electronic states. Unfortunately it is not possible to calculate the PE cross section directly from tight-binding simulations. Also the density of states cannot easily be extracted exactly from such calculations because the finite lifetime and, accordingly, the energy bandwidth of the electronic states can not be derived from the numerical data.

To obtain further information from the calculated band structure in figure 3.4, we take a closer look at the number of unoccupied electronic states in the $\Gamma \rightarrow L$ direction of the Brillouin zone, *i.e.* the states involved in direct transitions from the Γ point to unoccupied energy states. This direction is orientated perpendicular to the sample surface and therefore responsible for the PE in the normal direction. In Fig. 3.5 the number of unoccupied electronic states for each 0.5 eV energy interval above the Fermi level is plotted as grey colored bars. The total number is normalized to the maximum value, at an energy of $E - E_F = 38.5$ eV. A relatively low number of electronic states per energy interval is observed for energies below $E - E_F = 35$ eV. Increasing the energy, a sharp rise in the number of states is observed, reaching a maximum at $E - E_F = 38.5$ eV above the Fermi level, followed again by a fast decrease. This maximum indicates a high number of electronic states in a relatively narrow energy region. The energy bandwidth of the unoccupied electronic states of graphene was assumed to increase linearly with the energy of the state, ranging from 300 meV for states close to the Fermi level up to 2 eV for states at the highest energy

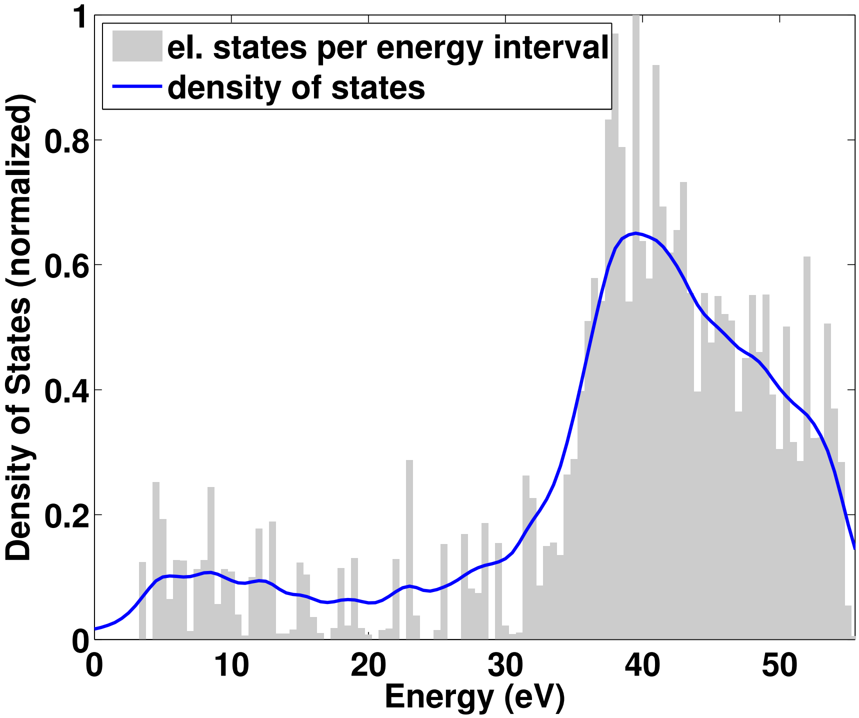

Figure 3.5: Number of unoccupied electronic states in 0.5 eV energy intervals (grey). The calculated density of states assuming a 2 eV energy bandwidth for all states observed is plotted in blue. The zero of the bottom scale represents the position of the Fermi level.

considered. Of course this is a very rough assumption because the electronic lifetime in each state will depend on the specific electron energy and momentum. The resulting approximated density of states is plotted as a blue line in Fig. 3.5. As expected from the number of electronic states mentioned before, the density of states shows a broad maximum at about 38.5 eV above the Fermi level.

Assuming that each PE cross section is proportional to the density of accessible unoccupied electronic states, the relative cross sections can be calculated. When comparing to the measured resonance, one has to bear in mind that the latter is broadened by the energy bandwidth of the ground state and the spectral bandwidth of the exciting photon source. The energy bandwidth of the occupied electronic states of graphene has been measured to be approximately 2 eV both for the π- and the σ-state

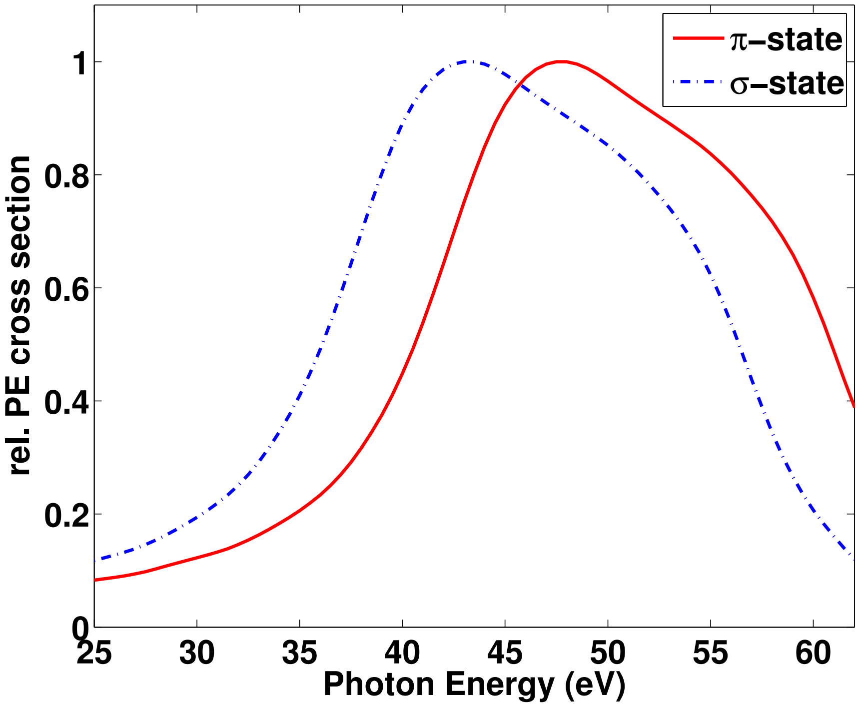

Figure 3.6: Calculated relative cross section for Photoemission from the σ and π bands of free standing graphene

[19] and it is assumed to be a Lorentzian function again. The spectral bandwidth of the high harmonic source is relatively broad due to the ultrashort pulse duration. A Gaussian spectral distribution with a FWHM of ΔE =0.3 eV has been measured. To calculate the relative PE cross sections for various photon energies under realistic experimental conditions, the density of states distribution in Fig. 3.5 was convoluted with the energy distribution of the ground state and the spectral distribution of the photon source. Additionally, the ground state binding energy was taken into account. The resulting relative PE cross sections for the graphene σ and π states are plotted in Fig. 3.6.

The calculated relative PE cross sections were normalized as in Fig. 3.3 for a better comparison. The cross section dependence on photon energy is the same for emission from the σ and the π bands, because the same approximations were made for both states. The rising slope is slightly steeper than the falling slope when increasing the photon energy across the resonance. The overall shape of the calculated cross section resonances and their width in photon energies correspond well to the experimental data. The cross section for emission from the σ- state reaches a maximum at a photon energy of $h\nu = 41$ eV, for emission from the π-state a maximum at $h\nu = 46$ eV. The energetic shift between the maxima can simply be explained by the difference in binding energy of the two electronic states extracted from the tight-binding band structure calculations. However, the maxima of these resonances are shifted by about 5-7 eV to higher photon energies as compared to the experimental findings.

The tight-binding calculations have been performed for free standing graphene instead of graphene on a Ni(111) substrate. The energetic shift of the PE cross sections therefore reflects the signature of the interaction of the graphene with the nickel substrate which, as already stated in the results section, shifts the position of the σ and π bands by about 2 eV towards higher binding energies [13, 14, 20].

3.5 CONCLUSION

In this work we have experimentally and numerically investigated the PE cross section for graphene on Ni(111) up to photon energies of 54.6 eV. Resonances in the PE cross section were found for the graphene σ as well as the π state.
The measured PE cross sections were compared to a standard tight binding calculation for free standing graphene. A comparison between the calculated and the experimentally determined cross sections show a good qualitative agreement. The cross section resonances can therefore be explained by a high density of unoccupied electronic states in a small energy interval in $\Gamma \rightarrow L$ direction. The energetic shift between the calculated and measured maxima of the resonances is attributed to the effect of the interaction between the substrate and the graphene on the electronic structure.

REFERENCES

[1] K. S. Novoselov, A. K. Geim, S. V. Morozov, D. Jiang, Y. Zhang, S. V. Dubonos, I. V. Grigorieva, and A. A. Firsov, *Science* **306**, 666 (2004).

[2] A. K. Geim, *Science* **324**, 1530 (2009).

[3] D. R. Cooper, B. D'Anjou, N. Ghattamaneni, B. Harack, M. Hilke, A. Horth, N. Majlis, M. Massicotte, L. Vandsburger, E. Whiteway, and V. Yu, *ISRN Condensed Matter Physics* **2012**, 56 (2012).

[4] A. H. Castro Neto, F. Guinea, N. M. R. Peres, K. S. Novoselov, and A. K. Geim, *Review of Modern Physics* **81**, 109 (2009).

[5] J. Wintterlin and M.-L. Bocquet, *Surface Science* **603**, 1841 (2009).

[6] M. Batzill, *Surface Science Reports* **67**, 83 (2012).

[7] A. Bostwick, T. Ohta, T. Seyller, K. Horn, and E. Rotenberg, *Nat Phys* **3**, 36 (2007).

[8] T. Pfeifer, C. Spielmann, and G. Gerber, *Reports on Progress in Physics* **69**, 443 (2006).

[9] T. Haarlammert and H. Zacharias, *Current Opinion in Solid State and Materials Science* **13**, 13 (2009).

[10] J. Hüve, T. Haarlammert, T. Steinbrück, J. Kutzner, G. Tsilimis, and H. Zacharias, *Optics Communications* **266**, 261 (2006).

[11] C. Spielmann, N. H. Burnett, S. Sartania, R. Koppitsch, M. Schnürer, C. Kan, M. Lenzner, P. Wobrauschek, and F. Krausz, *Science* **278**, 661 (1997).

[12] S. Evans, J. Pielasze, and J. M. Thomas, *Surface Science* **55**, 644 (1976).

[13] A. Grüneis and D. V. Vyalikh, *Physical Review B* **77**, 193401 (2008).

[14] Y. S. Dedkov and M. Fonin, *New Journal of Physics* **12**, 125004 (2010).

[15] J. Hermanson, *Solid State Communications* **22**, 9 (1977).

[16] A. R. Law, M. T. Johnson, and H. P. Hughes, *Physical Review B* **34**, 4289 (1986).

[17] T. Haarlammert, A. V. Golovin, and H. Zacharias, *Physical Review B* **83**, 125435 (2011).

[18] S. Reich, J. Maultzsch, C. Thomsen, and P. Ordejón, *Physical Review B* **66**, 035412 (2002).

[19] T. Ohta, A. Bostwick, J. L. McChesney, T. Seyller, K. Horn, and E. Rotenberg, *Physical Review Letters* **98**, 206802 (2007).

[20] P. A. Khomyakov, G. Giovannetti, P. C. Rusu, G. Brocks, J. van den Brink, and P. J. Kelly, *Physical Review B* **79**, 195425 (2009).

Chapter Four

Dynamics of excited electronic states at graphene/Ni(111) interface

The dynamics of excited electronic states at the graphene/Ni(111) interface has been investigated by means of time-resolved photoemission spectroscopy, employing a High-Harmonics generation setup producing EUV fs-pulses with an energy of 39.2 eV. The dependence of the lifetimes on the energy of the intermediate state $E - E_F$ was found to be the result of an interplay of substrate and adsorbate bandstructure characters. A dual character of the decay rate of the excited carriers and features typical of graphitic compounds were observed.

The work described in this chapter was reported in:
L. Bignardi, T. Haarlammert, C. Winter, M. Montagnese, P. van Loosdrecht, E. Voloshina, P. Rudolf, H. Zacharias, *Dynamics of excited electronic states at Gr/Ni(111) interface*, in preparation.

4.1 INTRODUCTION

The exploration of the electronic and structural properties of the graphene/metal interfaces gained recently great importance in view of a future technological applications of graphene because of the possibility to grow graphene layers with very high quality on some metallic surfaces [1, 2, 3, 4]. From a fundamental point of view, these interfaces are particularly interesting because depending on the metal on which graphene is grown the level of interaction between adsorbate and substrate can be tuned from weak to strong, inducing variations in the workfunction and in electron doping of graphene at metallic contacts [5, 6, 7, 8] or causing substrate-imposed morphological modifications of the carbon sheet [9, 10].

Among the graphene/metal interfaces, graphene (Gr) on Ni(111) has systematically been a focus of considerable interest in the last years both from the experimental and the theoretical point of view [6, 4, 11]. Angle-resolved photoemission experiments have probed the occupied part of the electronic band structure of the interface [12, 13], demonstrating a hybridization of the π band of graphene with the d band of nickel in the region of the Dirac cone, which leads to major modifications in the band shape and to a strong interaction of the graphene with the substrate [11]. Futhermore, this interface has been predicted to be spin-filtering and therefore appealing for the implementation of spintronics devices [14, 15]. A spin-polarized photoemission signal from the interface has been in fact observed [16] together with a manifestation of Rashba interaction between spin-polarized electrons in the π band and the large effective electric field at the graphene/Ni interface [12]. Furthermore, a transfer of magnetic momentum from the Ni substrate to graphene was observed by means of X-ray circular dichroism measurements [17], opening a way to study the ferromagnetic character of graphene.

An important topic still to be fully explored concerns the dynamics of excited charge carriers at the Gr/Ni(111) interface, which is relevant to transport phenomena as well as to molecule-surface interactions, in the framework of an implementation of spintronic devices based on this interface [11].

An ideal tool to unravel the transient behavior of excited electronic states at surfaces of metals is time-resolved photoemission (TR- PES) spectroscopy with ultrafast laser pulses. This technique has proven very powerful for probing the dynamics of electron-electron and electron-phonon interactions at clean and adsorbate-covered metal surfaces and to measure lifetimes of excited quasiparticle states with high precision [18, 19, 20, 21, 22, 23]. A large impulse to the TR-PES experiments came with the development of the High-Harmonics generation (HHG) sources, which offered a table-top way to produce EUV pulses at a femtosecond timescale, opening the way to the investigation of the relaxation processes in atomic physics, solid-state physics and surface science on a very wide energy scale [24].

This kind of experiments, together with a robust theoretical effort, have suggested that a free-electron approach based on the Fermi-liquid theory [25, 26], in some cases, is unsuitable to describe the lifetimes of excited states in metals and indicated that a more accurate modeling was needed [27, 28, 29, 30].

Herein, we present a study of the dynamics of photoexcited electronic states at the Gr/Ni(111) interface where we show that the lifetime of the excited charge carriers is determined by the interplay of substrate and adsorbate band structures. Valence band spectra have been acquired with a EUV fs-pulse in a pump-probe experiment after exciting the interface with an infrared fs light pulse. Extracted energy-dependent transients of electronic excitations are compared to the lifetimes found for the clean Ni surface and for highly-oriented pyrolytic graphite (HOPG). DFT calculations of the joint density of states support the experimental data and illustrate the importance of band structure effects in shaping the transient dynamics.

4.2 EXPERIMENTAL

Ultra-short laser pulses were produced with a mode-locked, cavity-dumped Ti:Sapp oscillator, whose output was amplified by a cryogenically-cooled Ti:Sapphire amplifier. Finally, 35 fs pulses are generated with a central wavelength of 790 nm (1.57 eV), having an energy per pulse of 0.8 mJ at a repetition rate of 6 kHz. The TR-PES spectra were acquired employing a *pump-probe* geometry experiment, where the pump beam was chosen to be the 5% of the pulse energy of the total output of the amplifier. The size of the pump beam at the sample was about 0.01 cm^2, achieving a peak intensity on the sample of about 1.1×10^{11} W/cm^2. The remaining output of the amplifier was focused into a HHG setup, where IR ultrashort pulses were focused onto an Ar-gas target for nonlinear frequency conversion [31]. Several odd harmonic orders of the fundamental photon energy were generated simultaneously. Therefore, a Mo/Si mirror was used to select a specific harmonic order and thus to change the energy of the photon employed for photoemission experiments. The chosen harmonics corresponded to an EUV photon ($h\nu_{probe}$ = 39.2 eV) and served as probe beam. The time delay between pump and probe could be varied by means of a delay stage, modifying the length of the optical path of the pump. Time-resolved valence band photoemission spectra were acquired by tuning the pump-probe delay in a range between -100 fs and +100 fs, with 10 fs steps.

The time-resolved spectra were recorded by means of a Time-of-Flight (ToF) spectrometer, consisting of a field-free drift tube, terminated with a multichannel plate detector. All the spectra shown were acquired at normal emission and at room temperature (300 K). The angular acceptance of the spectrometer was ±2.5°, which corresponds to an integration over $\Delta k_{||} = 0.37\,\text{Å}^{-1}$ at $E_{kin} = 39.2\,\text{eV}$. Pump and probe beams were focused into a ultra-high vacuum chamber (base pressure 2×10^{-10} mbar) where a Ni(111) single crystal was attached to a Mo plate. The surface of Ni(111) was cleaned with several cycles of Ar-ions sputtering (E_b = 1 keV) followed by annealing at high-temperature (1080 K). Graphene was grown *in-situ* by chemical vapour deposition of ethylene on the Ni surface, according to the procedure described earlier [32, 16]. The cracking reaction took place at a pressure of 10^{-6} mbar of ethylene, while keeping the crystal at a temperature of 870 K for a few minutes. Low-energy electron diffraction (LEED) on the freshly-prepared sample showed a (1×1) pattern due to the almost perfect matching of graphene and Ni(111) surface lattice parameters. The angle-integrated valence band spectrum (not shown), acquired with a commercial He-II discharge lamp and electron analyzer (SPECS CSA300), evidenced the presence of σ and π bands of graphene and was found to be similar to the literature data for graphene single-layer on Ni(111) [12, 11].

4.3 RESULTS AND DISCUSSION

EUV PULSE CHARACTERIZATION AND LAPE EFFECT

A valence band spectrum acquired from graphene/Ni(111) with our setup is shown in figure 4.1. The blue dashed line corresponds to a spectrum acquired with the sole probe beam. The peaks of Ni 3d band and of π and σ band of graphene were detected at about 1.5 eV, 6 eV and 11 eV below the Fermi level. Their positions were found to be consistent with the spectrum acquired with a He-II discharge lamp and earlier works [16, 12] . The red continuous line represents a spectrum acquired while IR pump and EUV probe pulses reach simultaneously the sample, *i.e.* for a pump-probe delay time $\Delta t = 0$ fs.

At $\Delta t = 0$ fs, a depletion of the intensity is observed for Ni 3d peak (labeled with α from now on) with respect to the case of the spectrum acquired with the EUV pulse

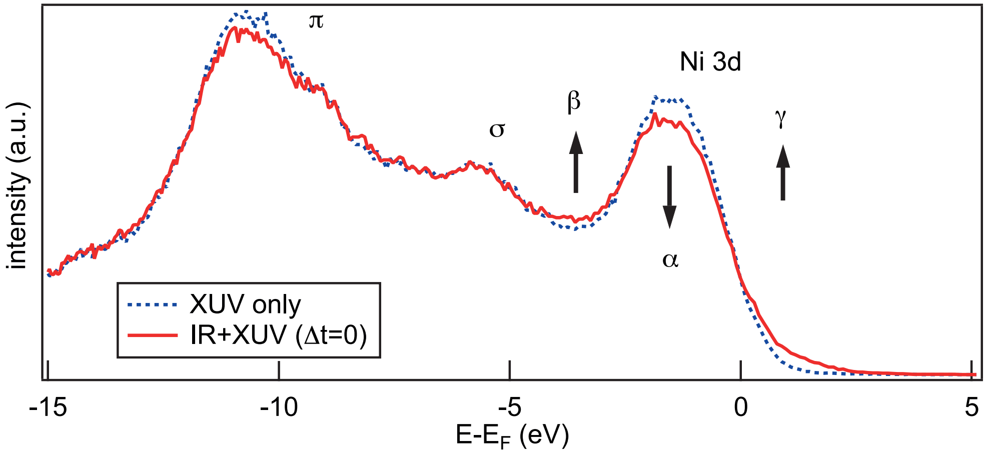

Figure 4.1: Valence band of graphene/Ni(111) interface, acquired with a High-Harmonics generation setup producing EUV fs-pulses with an energy of 39.2 eV. The dashed blue line represents the spectrum acquired with EUV probe beam only. The red continuous line represents the spectrum acquired with IR pump and EUV probe, at delay time $\Delta t = 0$. The zero on the energy axis corresponds to the Fermi level E_F

alone. On the other hand, additional bands (β and γ) rose alongside the α peak, marked by the upward-pointing arrows. The presence of these sidebands and the depletion of the intensity for the β peak was found to depend on the pump-probe delay and to be maximized at $\Delta t = 0$. Thus, we inferred that the simultaneous arrival of pump and probe on the sample is responsible for the observed modification in the spectral intensity.

To quantify the change in PE intensity observed, we calculated the difference in the photoemission signal for the two spectra shown in figure 4.1. The difference is plotted in figure 4.2-(a). The experimental results (blue dots) are interpolated with a convolution of three Gaussian peaks (dashed lines). The fit shows that the decrease in intensity of peak α is compensated by the two rising sidebands β and γ, spaced by an energy $h\nu_{\text{pump}} = 1.56$ eV from the peak α.

The area of the peak β corresponds to the sum (with sign changed) of the area of peaks β and γ. Furthermore, the intensity of the γ sideband appeared to be higher than that of β band, as can be seen in figure 4.2-(a).

To interpret this asymmetry in the intensity of the peaks β and γ, we sketch in figure 4.2-(b) the photoemission mechanisms resulting in spectrum at $\Delta t = 0$ in figure 4.1. The most prominent process is the direct single-photon photoemission caused

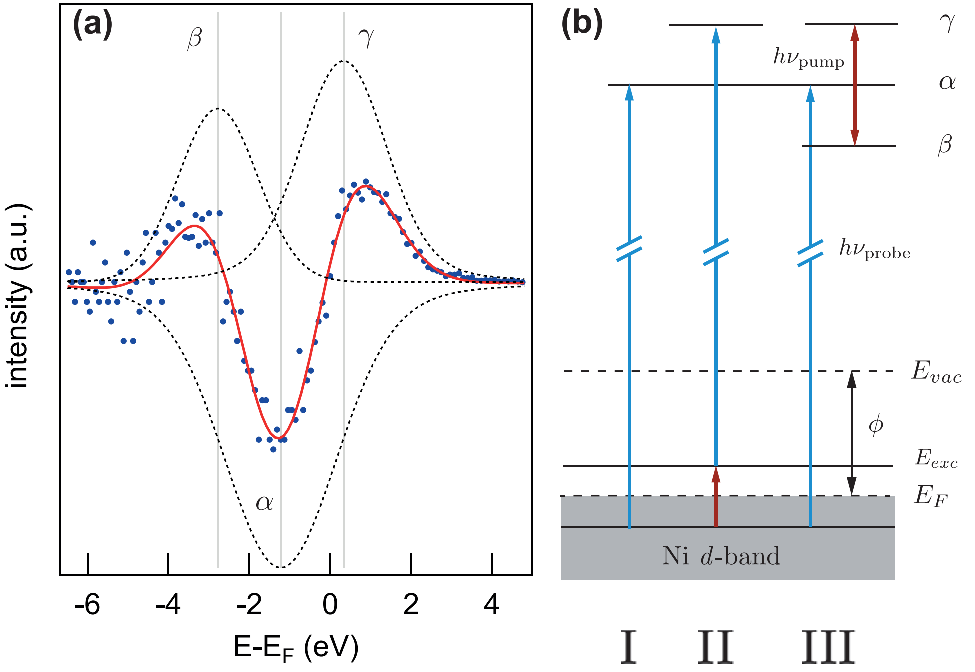

Figure 4.2: a) Difference of the photoemission signal between the two spectra shown in figure 1, in the proximity of the Ni 3d peak. The blue points are the experimental data, the red continuous line is the fitting plot resulting from the sum of the three dashed-line peaks. (b) Scheme of the photoemission mechanisms involved in the process (see text for explanation).

by the EUV pulses (I), which excite electrons from a state E_0 belonging to Ni 3d band into an α final state. The simultaneous arrival of pump and probe pulses on the sample also gives rise to multi-photonic photoemission processes. The IR pump produces a distribution of photoexcited electrons, which fill unoccupied states at E_{exc} above the Fermi energy and are then photoemitted by the probe pulses into the state γ (process II). Moreover, the high peak-intensity of the pump beam on the sample (ca. 10^{11} W/cm^2) leads to the formation of sidebands to the α peak as a result of the laser-assisted photoemission effect (LAPE), which was observed at clean and adsorbate covered metallic surfaces for this range of laser intensities [33, 34]. Hence, symmetrical sidebands, spaced by 1.56 eV from the central α peak (*i.e.* the IR pump energy), are detected at $\Delta t = 0$, contributing to the final intensity of the peaks β and γ (process III). We can therefore conclude that a higher intensity of the γ sideband can be explained with the contribution of the processes II and III, while the intensity of peak β yields only from the LAPE effect.

Because of the instantaneous nature of the LAPE signal, the intensity of the sidebands can be plotted as a function of the time delay in order to characterize the EUV probe pulse. In particular, we extracted the profile of the intensity of the sideband β versus the time delay. Since the intensity of this band is only the result of a LAPE process, the resulting peak shape was supposed to be a very good approximation of the cross-correlation of the IR and EUV pulses. The width of the cross-correlation was found to be 56 ± 7 fs. The width of the IR pump pulse was independently measured with the SPIDER method[35] and established to be equal to 35 ± 10 fs. By deconvolution of the cross-correlation and the pump-pulse autocorrelation, the pulse duration of the EUV probe pulse was determined to amount to 21 ± 10 fs.

LIFETIMES EXTRACTION

A complete characterization of the pump and probe intensities allowed us to focus our attention on the dynamics of the electronic scattering process that happens at the surface when the pump beam reaches the sample. Information about the transient of the excited states is obtained by evaluating the dependence of the intensity of the γ peak in the valence band on the pump-probe time delay. This peak, as stated earlier, is the result of the creation of a distribution of photoexcited electrons on which a contribution of LAPE mechanism is superimposed. By changing the pump-probe delay, we monitored the photoemission intensity for intermediate excited states in order to extract its lifetime. For each of the intermediate states, which were grouped into 0.1 eV wide bins, the photoemission intensity *versus* the pump-probe delay was plotted, as shown in the inset of figure 4.3. This lineshape was fitted with a convolution of the cross-correlation (Gaussian) pulse with an exponential decay $\exp[-t/\tau]$, which is accounting for the decay of the photoexcited electronic state.

In figure 4.3, we show the dependence of the decay rates $\Gamma = 1/\tau$ as a function of the intermediate state energy $E - E_F$ (plotted with red circles). In this plot three regions can be clearly identified. In the range $E - E_F < 1$ eV and for $E - E_F > 1.5$ eV, the value of Γ was found to increase with increasing energy of the intermediate state while a wide plateau where Γ remains nearly constant is observed in the region between 1 and 1.5 eV. To gain a deeper insight on the energy dependence of the decay rate at the Gr/Ni(111) interface, we compared our data with decay rates measured with TR-photoemission experiments on nickel[30] and a DFT calculation on

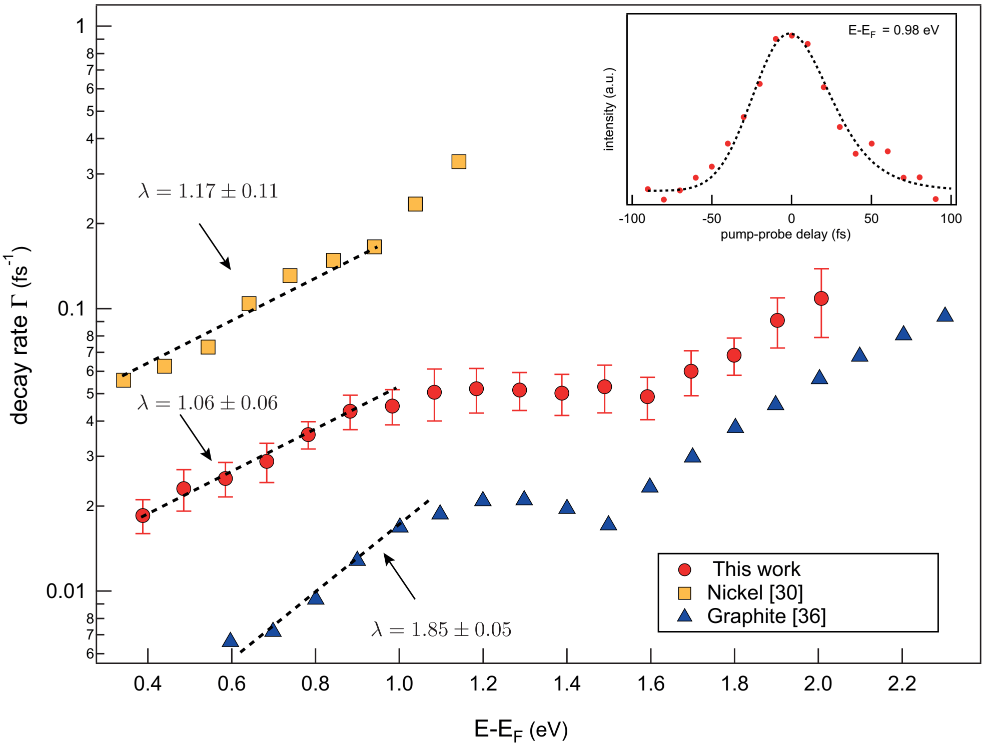

Figure 4.3: Decay rates $\Gamma = 1/\tau$ of photoexcited electrons, plotted as a function of the energy of the intermediate state (semi-log scale). The inset shows the pump-probe scan curve while monitoring electrons photoemitted from states at about 0.98 eV above E_F. The red filled dots represent the experimental data, while the dashed line is the fitting curve given by the convolution of cross-correlation of the pulses with an exponential decay curve accounting for the excited state electrons relaxation. The values of λ reported refers to the trend of the decay rate Γ in the range $E - E_F < 1$ eV.

graphite[36], which are plotted in figure 4.3 with yellow squares and blue triangles, respectively.

In the energy range $E - E_F < 1$ eV, the decay rate of Gr/Ni goes as $(E - E_F)^\lambda$ with $\lambda = 1.06 \pm 0.06$. This value is rather similar to the one found for Ni, $\lambda = 1.17 \pm 0.11$, where the decay rate of the excited charge carriers can be modeled by the same expression. We can therefore conclude that in this energy range the scattering mechanism for the electrons of the excited states in Gr/Ni is similar to metallic Ni. Furthermore, we can notice that the decay rate measured in Gr/Ni is significantly smaller than that recorded for Ni; therefore the lifetime of the excited charge carriers increases when graphene is adsorbed on the surface of the metal. On the other hand the decay rate for graphite shows a much stronger dependence on the energy, with an exponent λ equal to 1.87 ± 0.05.

In the energy range $1 < E - E_F < 1.5$ eV, a plateau-like region is present in the plot of the decay rates for both Gr/Ni and graphite: the onset of this plateau and its width are unaltered for Gr/Ni with respect to what is predicted[36] and observed[37] for graphite and even the values of Γ are almost identical to those predicted for HOPG. We therefore conclude that in the energy range $1 < E - E_F < 1.5$ eV the scattering process ruling the decay rates from the excited state is similar in graphite and at the Gr/Ni interface.

The decay rates observed in TR-PES experiments may directly depend on the shape of the unoccupied electronic bands of the interface, which can be important in understanding the scattering mechanism for excited electronic states. Deviations from the standard Fermi liquid behavior in transition metals like Ni or Co were found to be accountable to the presence of the partially filled, non-dispersive d-bands [27, 30]. On the other hand, the plateau-like region, observed in the energy dependence of the decay rate [36, 37] in HOPG, was directly related to the presence of a van Hove singularity at the M point of the Brillouin zone, located about 1.4 eV above E_F . This resulted in very small decay rates for electronic states located close to the singularity, where many-body effects can become very important [36, 38, 39].

Thus, to better understand the mechanism which rules the scattering process of excited charge carriers a detailed knowledge of the unoccupied band structure is needed. DFT calculations of the band structure and the corresponding C-atom projected density of states for the Gr/Ni(111) interface were carried out. The calculations were performed using the projector augmented wave method[40], a plane wave basis set and the generalized gradient approximation as parameterized by Perdew *et al.* [41], as implemented in the VASP program[42]. The plane wave kinetic energy cutoff was set to 500 eV. The long-range van der Waals interactions were accounted for by means of a semiempirical DFT-D2 approach proposed by Grimme[43]. The supercell used to model the graphene-metal interface was constructed from a slab of 13 layers of nickel atoms with a graphene layer adsorbed at both sides and a vacuum region of approximately 18 Å. In optimizing the geometry, the positions (z-coordinates) of the carbon atoms as well as those of the top two layers of metal atoms were allowed to relax. In the total energy calculations and during the structural relaxations the k-meshes for sampling the supercell Brillouin zone were chosen to be as dense as 24×24 and 12×12, respectively. The calculated projected DOS (PDOS) of graphene/Ni(111) is shown in figure 4.4-(b); the calculated projected DOS for graphite is also reported (panel (a)) for comparison.

In the energy region $E - E_F < 1$ a peak in the PDOS is observed, as a result of the hybridization of the graphene unoccupied π^* band with the unoccupied Ni d bands. We attribute the Ni-like decay rate observed for Gr/Ni in this energy range to the presence of unfilled d-bands [27, 30]. Secondly, a peak in the PDOS of Gr/Ni is predicted at ca. 1.1 eV above E_F. Within the accuracy of the DFT calculations, the energy position of this peak coincides with the plateau-like region observed for the decay rate of excited charge carriers in Gr/Ni. Therefore, we speculate that the presence of a singularity in the DOS affects the decay rate of Gr/Ni, producing a situation similar to what is observed in HOPG [37, 36].

As mentioned earlier, the onset of the plateau in the energy dependence of the decay rate in Gr/Ni and in graphite is the same, despite of the different PDOS of the two interfaces. This observation may suggest that many-body effects are relevant [44, 38, 39] in producing electronic states in the energy range $1 < E - E_F < 1.5$ eV which do no scatter and whose lifetime is greater than expected.

In conclusion, we explored the dynamics of excited charge carriers at the Gr/Ni(111) interface, by means of a time-resolved photoemission experiment based on a HHG setup. The decay rate from the excited states, Γ, was extracted by comparison of the valence band spectra acquired at different pump-probe time delays. The dependence of the decay rate on the energy of the intermediate state was found to be similar to that measured on clean Ni in the energy range $E - E_F < 1$ eV. On the contrary, a nearly constant decay rate was observed for intermediate states in the energy range $1 < E - E_F < 1.5$ eV, of which identically to what is observed on HOPG. We attribute this behaviour to the presence of a residual van Hove singularity in the PDOS of Gr/Ni.

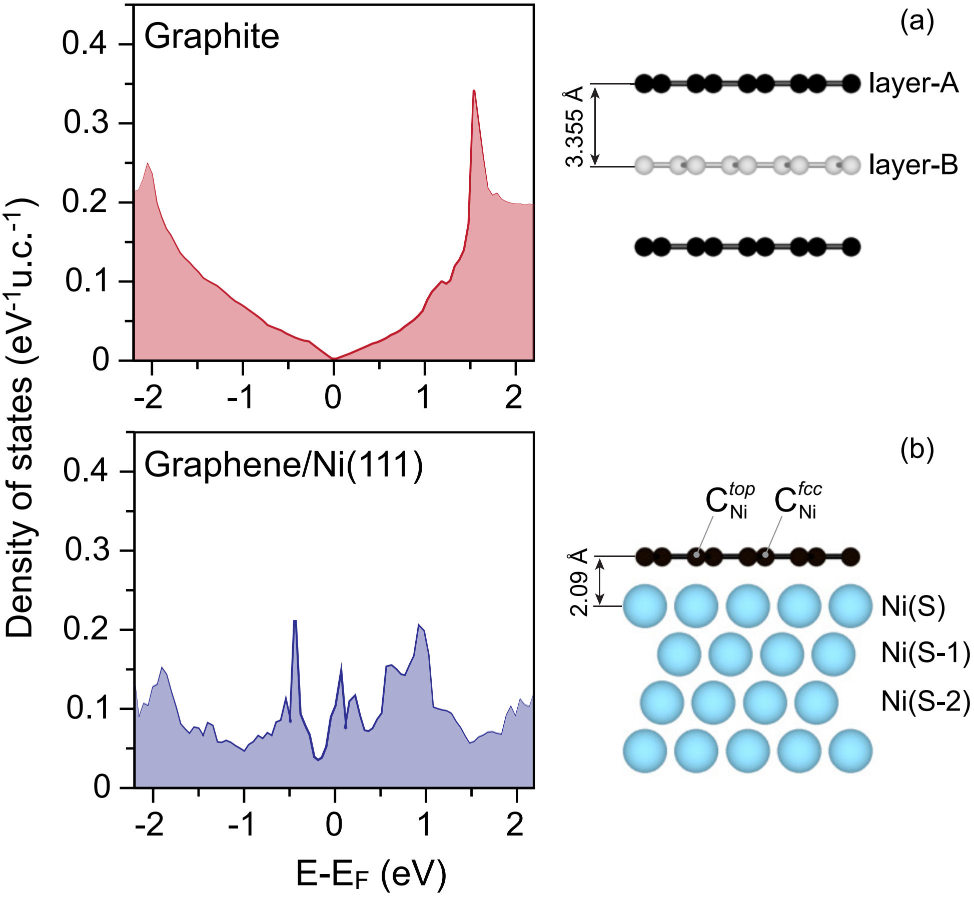

Figure 4.4: Projected density of states (PDOS) for C atoms calculated for graphene (a) and for (b) the graphene/Ni(111) interface. In each panel a schematic draw of the model used for the calculations is shown. Image: courtesy Dr. Elena Voloshina.

REFERENCES

[1] J. Wintterlin and M.-L. Bocquet, *Surface Science* **603**, 1841 (2009).

[2] D. R. Cooper, B. D'Anjou, N. Ghattamaneni, B. Harack, M. Hilke, A. Horth, N. Majlis, M. Massicotte, L. Vandsburger, E. Whiteway, and V. Yu, *ISRN Condensed Matter Physics* **2012**, 56 (2012).

[3] M. Batzill, *Surface Science Reports* **67**, 83 (2012).

[4] E. Voloshina and Y. Dedkov, *Physical Chemistry Chemical Physics* **14**, 13502 (2012).

[5] C. Lee, X. Wei, J. W. Kysar, and J. Hone, *Science* **321**, 385 (2008).

[6] P. A. Khomyakov, G. Giovannetti, P. C. Rusu, G. Brocks, J. van den Brink, and P. J. Kelly, *Physical Review B* **79**, 195425 (2009).

[7] G. Giovannetti, P. A. Khomyakov, G. Brocks, V. M. Karpan, J. van den Brink, and P. J. Kelly, *Physical Review Letters* **101**, 026803 (2008).

[8] C. Gong, D. Hinojos, W. Wang, N. Nijem, B. Shan, R. M. Wallace, K. Cho, and Y. J. Chabal, *ACS Nano* **6**, 5381 (2012).

[9] A. T. N'Diaye, J. Coraux, T. N. Plasa, C. Busse, and T. Michely, *New Journal of Physics* **10**, 043033 (2008).

[10] P. Lacovig, M. Pozzo, D. Alfè, P. Vilmercati, A. Baraldi, and S. Lizzit, *Physical Review Letters* **103**, 166101 (2009).

[11] Y. S. Dedkov and M. Fonin, *New Journal of Physics* **12**, 125004 (2010).

[12] Y. S. Dedkov, M. Fonin, U. Rüdiger, and C. Laubschat, *Physical Review Letters* **100**, 107602 (2008).

[13] A. Varykhalov, J. Sánchez-Barriga, A. Shikin, C. Biswas, E. Vescovo, A. Rybkin, D. Marchenko, and O. Rader, *Physical Review Letters* **101**, 1 (2008).

[14] V. Karpan, G. Giovannetti, P. Khomyakov, M. Talanana, a. Starikov, M. Zwierzycki, J. van Den Brink, G. Brocks, and P. Kelly, *Physical Review Letters* **99** (2007).

[15] V. M. Karpan, P. A. Khomyakov, A. A. Starikov, G. Giovannetti, M. Zwierzycki, M. Talanana, G. Brocks, J. Van Den Brink, and P. J. Kelly, *Physical Review B* **78**, 195419 (2008).

[16] Y. S. Dedkov, M. Fonin, and C. Laubschat, *Applied Physics Letters* **92**, 052506 (2008).

[17] M. Weser, Y. Rehder, K. Horn, M. Sicot, M. Fonin, A. B. Preobrajenski, E. N. Voloshina, E. Goering, and Y. S. Dedkov, *Applied Physics Letters* **96**, 012504 (2010).

[18] M. Wolf, *Surface Science* **377-379**, 343 (1997).

[19] H. Petek and S. Ogawa, *Progress in Surface Science* **56**, 239 (1997).

[20] S. Ogawa, *Journal of Electron Spectroscopy and Related Phenomena* **124**, 245 (2002).

[21] R. Haight, *Surface Science Reports* **21**, 275 (1995).

[22] M. Weinelt, *Journal of Physics: Condensed Matter* **14**, R1099 (2002).

[23] M. Rohleder, K. Duncker, W. Berthold, J. Güdde, and U. Höfer, *New Journal of Physics* **7**, 103 (2005).

[24] T. Haarlammert and H. Zacharias, *Current Opinion in Solid State and Materials Science* **13**, 13 (2009).

[25] J. J. Quinn, *Physical Review* **126**, 1453 (1962).

[26] N. Ashcroft and N. Mermin, *Solid state physics*, Saunders College (1976).

[27] E. Zarate, P. Apell, and P. M. Echenique, *Physical Review B* **60**, 2326 (1999).

[28] P. Echenique, J. Pitarke, E. Chulkov, and A. Rubio, *Chemical Physics* **251**, 1 (2000).

[29] P. Echenique, R. Berndt, E. Chulkov, T. Fauster, A. Goldmann, and U. Höfer, *Surface Science Reports* **52**, 219 (2004).

[30] R. Knorren, K. H. Bennemann, R. Burgermeister, and M. Aeschlimann, *Physical Review B* **61**, 9427 (2000).

[31] T. Haarlammert, A. V. Golovin, and H. Zacharias, *Physical Review B* **83**, 125435 (2011).

[32] C. Oshima and A. Nagashima, *Journal of Physics: Condensed Matter* **9**, 1 (1997).

[33] L. Miaja-Avila, C. Lei, M. Aeschlimann, J. L. Gland, M. M. Murnane, H. C. Kapteyn, and G. Saathoff, *Physical Review Letters* **97**, 113604 (2006).

[34] L. Miaja-Avila, G. Saathoff, S. Mathias, J. Yin, C. La-o vorakiat, M. Bauer, M. Aeschlimann, M. M. Murnane, and H. C. Kapteyn, *Physical Review Letters* **101**, 046101 (2008).

[35] C. Iaconis and I. Walmsley, *Optics Letters* **23**, 792 (1998).

[36] C. D. Spataru, M. A. Cazalilla, A. Rubio, L. X. Benedict, P. M. Echenique, and S. G. Louie, *Physical Review Letters* **87**, 4 (2001).

[37] G. Moos, C. Gahl, R. Fasel, M. Wolf, and T. Hertel, *Physical Review Letters* **87**, 24 (2001).

[38] K. F. Mak, J. Shan, and T. F. Heinz, *Physical Review Letters* **106**, 046401 (2011).

[39] K. F. Mak, L. Ju, F. Wang, and T. F. Heinz, *Solid State Communications* **152**, 1341 (2012).

[40] P. E. Blöchl, *Physical Review B* **50**, 17953 (1994).

[41] J. P. Perdew, K. Burke, and M. Ernzerhof, *Physical Review Letters* **77**, 3865 (1996).

[42] G. Kresse and J. Hafner, *Journal of Physics: Condensed Matter* **6**, 8245 (1994).

[43] S. Grimme, J. Antony, S. Ehrlich, and H. Krieg, *The Journal of Chemical Physics* **132**, 154104 (2010).

[44] L. Yang, J. Deslippe, C.-H. Park, M. L. Cohen, and S. G. Louie, *Physical Review Letters* **103**, 186802 (2009).

Chapter Five

Electronic and structural properties of graphene grown on Cu(111) by chemical vapour deposition

In this chapter, we shall describe a multi-technique characterization of the properties of graphene grown on Cu(111) surface by chemical vapour deposition. The electronic properties of the interface were investigated by (angle-resolved) photoemission spectroscopy and scanning photoemission microscopy, while scanning tunneling microscopy and low energy electron diffraction provided information about the structure.

5.1 INTRODUCTION

The growth of graphene on copper by CVD is nowadays the most exploited method for large scale production of graphene and extensively used for technology-oriented applications [1, 2]. This method allows the production of large graphene areas [3], whose quality, in terms of carrier mobility, does not match the high values achieved for flakes prepared through micro-mechanical cleaving but is by far higher than for samples prepared by chemical exfoliation

A detailed investigation of the interface properties of CVD grown graphene obtained by cracking of hydrocarbons on Cu(111) has not been performed yet. In particular, it is not known how the interaction with the copper substrate modifies the electronic properties of graphene. The growth of graphene on copper requires very high temperatures (about 1200 K) in order to catalytically split the hydrocarbon molecules [3].

An initial reduction of the metallic surface was reported [4] as an essential step to remove any native copper oxide that could prevent the formation of graphene. In this chapter we shall describe the investigation of the interfacial properties of graphene on copper by (angle-resolved) photoemission spectroscopy, scanning-photoemission microscopy, scanning tunneling microscopy and low energy electron diffraction. We shall also discuss how the first step of the growth protocol, namely the reduction in hydrogen at high temperature, affects the growth.

5.2 GROWTH AND PRELIMINARY CHARACTERIZATION

The Cu(111) single crystal was cleaned by several cycles of Ar-sputtering (E_b = 1 keV) and annealed in UHV at about 600 K. The crystal was transferred (through air) to a vacuum furnace and reduced for 1 h in a flow of argon (0.1 mbar) and hydrogen (0.5 mbar) at 1190 K. Graphene was grown by exposing the copper, held at 1190 K, to a mixture of argon (0.1 mbar), hydrogen (0.5 mbar) and methane (0.5 mbar). Low energy electron diffraction (LEED) was carried out on the sample after transfer (through air) from the vacuum furnace to a UHV chamber where the sample was annealed for 45 minutes at 570 K to remove the water and contaminants adsorbed during the transfer in air. The LEED pattern collected with a primary electron beam energy of 70 eV is shown in figure 5.1. The first order diffraction spots of Cu(111) are clearly visible (indicated by a blue arrow), together with additional spots (indicated by red arrow).

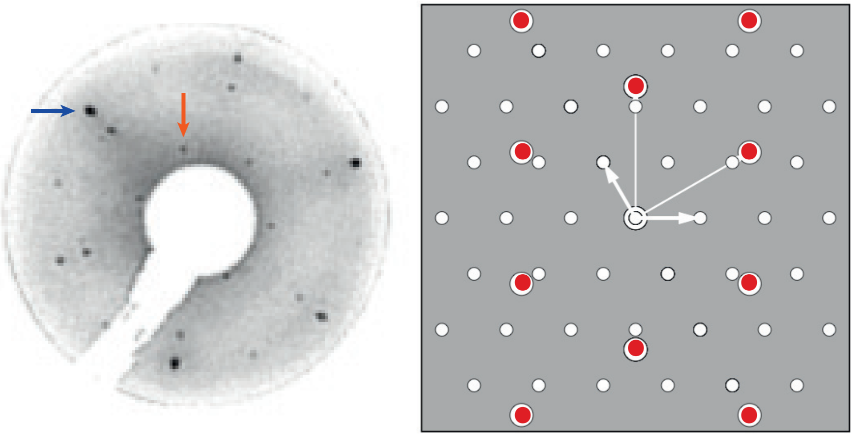

Figure 5.1: (left) LEED pattern of graphene grown on Cu(111), prepared according to the protocol described. The blue arrow points to a spot belonging to the Cu(111) substrate, the red arrow indicates a spot originating from a native copper oxide layer. The energy of the primary electron beam was 70 eV. (right) Simulated LEED pattern, reproducing the diffraction pattern shown in left panel. The red spots are the diffraction spots from the Cu(111) crystal.

We reconstructed the LEED pattern (right panel in figure 5.1), as due to an overlayer with a surface mesh described by

$$\begin{pmatrix} c_1 \\ c_2 \end{pmatrix} = G \begin{pmatrix} a_1 \\ a_2 \end{pmatrix}, \tag{5.1}$$

where a_1 and a_2 are the vectors of the reciprocal space associated with the copper substrate and G is the overlayer matrix

$$G = \begin{pmatrix} 2.30 & 1.15 \\ -1.15 & 1.15 \end{pmatrix} \tag{5.2}$$

By comparing this result with literature data [5, 6], we can associate such a pattern with the formation of oxide on copper . This implies that, surprisingly, no diffraction pattern attributable to the graphene lattice is detected.

Since the preparation of the copper surface and the CVD growth process of graphene were not carried out in the same UHV chamber, the observed LEED pattern could be due either to native oxide present on the copper substrate before graphene growth or to oxygen that intercalated below the graphene layer after the growth when the

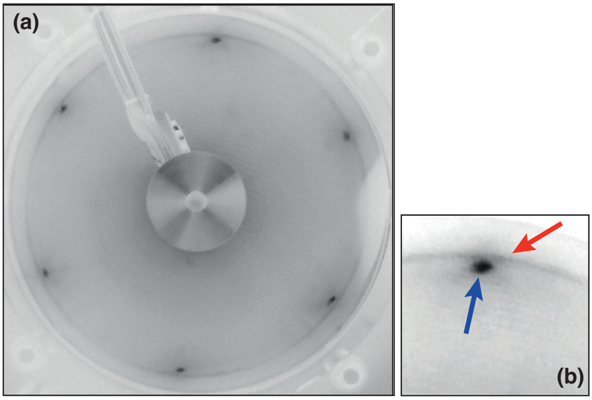

Figure 5.2: (a) LEED pattern acquired on the sample prepared with longer initial reduction. (b) Detail of the Cu(111) first order spot (blue arrow), with part of the ring structure (red arrow). The primary electron beam energy was 80 eV.

sample was exposed to air before LEED characterization. Therefore, to discriminate between the two we decided to increase the hydrogen reduction time in the furnace to 4 h and to increase the temperature during the growth process to 1250 K. The other growth parameters remained unaltered. The LEED pattern of the sample resulting from this growth protocol is shown in figure 5.2. In addition to the $(1, 1)$ spots associated with the Cu(111) surface a circular pattern is detected.

Figure 1.2-(b) shows a detailed image of the (1,1) spot. The lattice parameter of 2.46 Å associated with the ring pattern corresponds to the lattice parameter of graphene. We therefore conclude that the graphene layer is composed of grains of many different orientations, reason for which a ring pattern was observed. However, the intensity in the circular pattern is unevenly distributed and the higher signal in the vicinity of the spots of Cu(111) suggests that although the substrate provide a strong enough template to impose a certain growth direction, an important number of graphene domains has be aligned with the substrate orientation.

We tested the stability of this interface in ambient conditions by leaving the sample at atmospheric pressure for 3 days. We repeated afterwards LEED measurements and observed that the resulting pattern was identical to that shown in figure 5.1. The the ring pattern had disappeared and the spots attributed to the formation of an oxide layer were clearly visible. This indicates that graphene does not completely passivate the surface of copper, differently from what was reported earlier both for the graphene/copper [7] and graphene/Ni(111) interfaces [8, 9] . However the oxidation process of copper when exposed to atmospheric pressure is slower when the surface is covered by a graphene layer.

5.3 X-RAY PHOTOELECTRON SPECTROSCOPY

We investigated this sample by means of X-ray photoemission spectroscopy (XPS) to determine the chemical nature of the compounds present at the surface. The spectra have been collected by employing a non-monochromatized Al-Kα X-ray source and a hemispherical electron analyzer (ThermoFischer). In figure 5.3 we present the XPS spectra acquired on graphene/Cu(111) prepared with 1 hr. of initial reduction in hydrogen and not annealed in vacuo after transfer from the oven into the XPS chamber. The the carbon 1s, copper 2$p_{3/2}$ and oxygen 1s core level regions are shown in panels (a), (b) and (c). The C 1s signal can be fitted with two Voigt peaks, centered at binding energies of 284.5 eV (with a full width at half maximum (FWHM) of 1.7 eV) and 286.8 eV. The lower binding energy component is consistent with the presence of a graphitic layer on the surface [10, 11] while the second contribution can be assigned to C-O groups, which might have formed through adsorption of oxygen at graphene vacancies and defects during the transfer in air. The Cu 2$p_{3/2}$ signal was fitted with two Voigt components, centered at 932.8 and 933.4 eV. The former component can be attributed to metallic Cu (substrate) and to Cu2O, while the latter signals the presence of CuO [12]. The spectrum of the O 1s core level was fitted with three Voigt components centered at 529.9, 530.8 eV and 532.2 eV. The first component can be assigned to CuO while the second one stems from Cu_2O groups[12]. The highest binding energy component arises due to the presence of C-O groups [13] on the surface, as already discussed for the C1s photoemission signal.

We have repeated XPS measurements on a sample prepared with 4 h of initial reduction in hydrogen. Since the two series of spectra were acquired with a different hemispherical energy analyzer and therefore a different energy resolution, we could not directly compare the spectra acquired on the two different samples. However, it was possible to estimate the carbon/oxygen ratio for each series of XPS measurement, assuming that a layer of graphene was covering the surface. The XPS spectra collected are shown in figure 5.4 The C 1s photoemission line was fitted with two Voigt components (FWHM 2.7 eV)with binding energy positions 284.5 eV (graphitic layer) and 286.7 eV (associated to C-O groups). The Cu 2p3/2 line was fitted with a two Voigt peak (FWHM 2.7 eV), which corresponds to metallic copper and Cu_2O

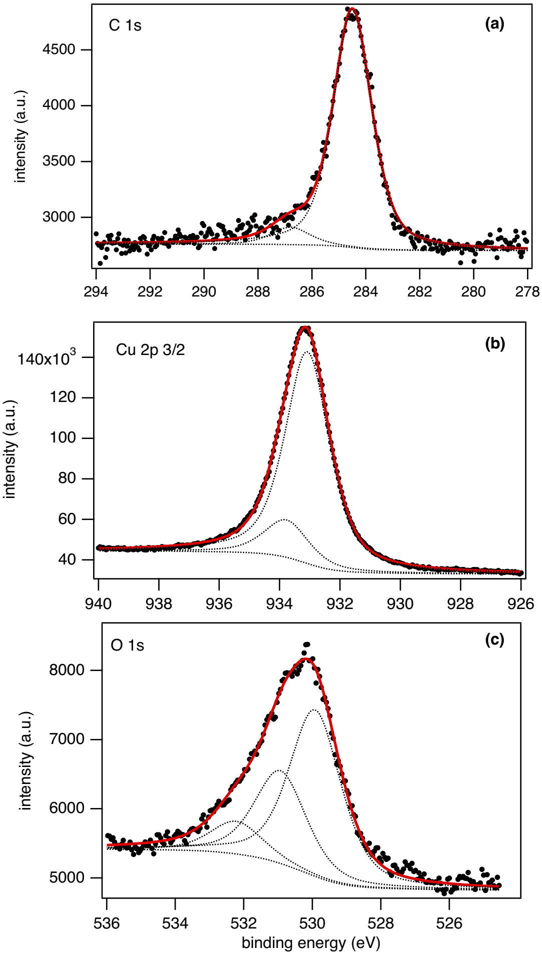

Figure 5.3: XPS spectra for graphene/Cu(111) not annealed *in vacuo*. (a) C 1s peak. (b) Cu 2p 3/2 peak. (c) O 1s peak. The black dots represents the data, the continuous red line corresponds to the total fit. The individual peaks used for the fit are represented with dotted black lines.

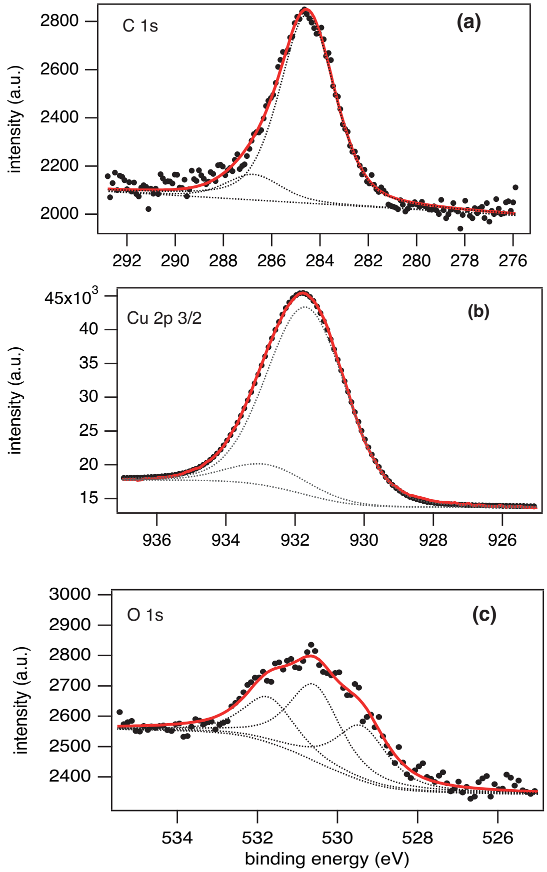

Figure 5.4: XPS spectra of (a) C 1s, (b) Cu 2p and (c) O 1s core levels, acquired on graphene/Cu(111) prepared with 4 hrs. of initial reduction in hydrogen. The black dots represent the data, the continuous red line corresponds to the total fit. The individual peaks used for the fit are represented with dotted black lines.

(932.5 eV) and CuO (932.9 eV) Compared to the previous case (1 hr. reduction in hydrogen), the ratio between the area of the CuO and metallic Cu peaks is smaller, indicating a smaller amount of oxide on the surface.

However, since the interpretation of the shifts observed for the Cu 2*p* peak might be ambiguous, we acquired the O 1s peak and we identified the same three components as in the first sample. However their relative inensity is different, namely the components associated with CuO (530.7 eV) and Cu_2O (529.7 eV) are less intense with respect to the component associated to the C-O groups (532.1 eV). By comparing the area of the O 1s and C 1s peaks and considering the sensitivity factors, we could calculate the ratio between carbon and oxygen present at the surface. We found that for a sample prepared with 1 h of preliminary reduction in hydrogen the O/C ratio was 0.3 (1 atom of oxygen every 3 atoms of carbon), while for the sample prepared with 4 h of reduction the ration decreased to 0.1. Therefore, the duration of the initial reduction is crucial for having a graphene/copper interface where no oxide (or a very low amount of it) is present. In conclusion, by combining XPS and LEED investigations we can therefore speculate that a layer of oxide grows on the surface during the transfer of a UHV prepared Cu(111) surface through air to the deposition furnace. In the following sections of the chapter, we will focus our attention on this sample with the oxide layer.

5.4 ANGLE-RESOLVED PHOTOELECTRON SPECTROSCOPY AND MICROSCOPY

In the previous section we have shown that the growth of a graphene layer could take place on a Cu(111) surface showing areas covered by copper oxide. The investigation of the valence band spectra of the graphene/Cu(111), prepared with one 1h of preliminary reduction, allows to shed light on the nature of the interaction between graphene and the supporting substrate. Angle-Resolved Photoelectron Spectroscopy (ARPES) was carried out at the SpectroMicroscopy beamline at the ELETTRA Synchrotron in Trieste, Italy. The impinging photon beam was focused with Schwarzschild optics resulting in a minimum beam diameter of 600 nm, which makes it suitable for sub-micrometer imaging and spectroscopy [14].

The samples were prepared as described earlier at the University of Groningen and taken to ELETTRA, where they were transferred to the end-station of the beamline. To remove water and contaminants adsorbed during the transport in air, the

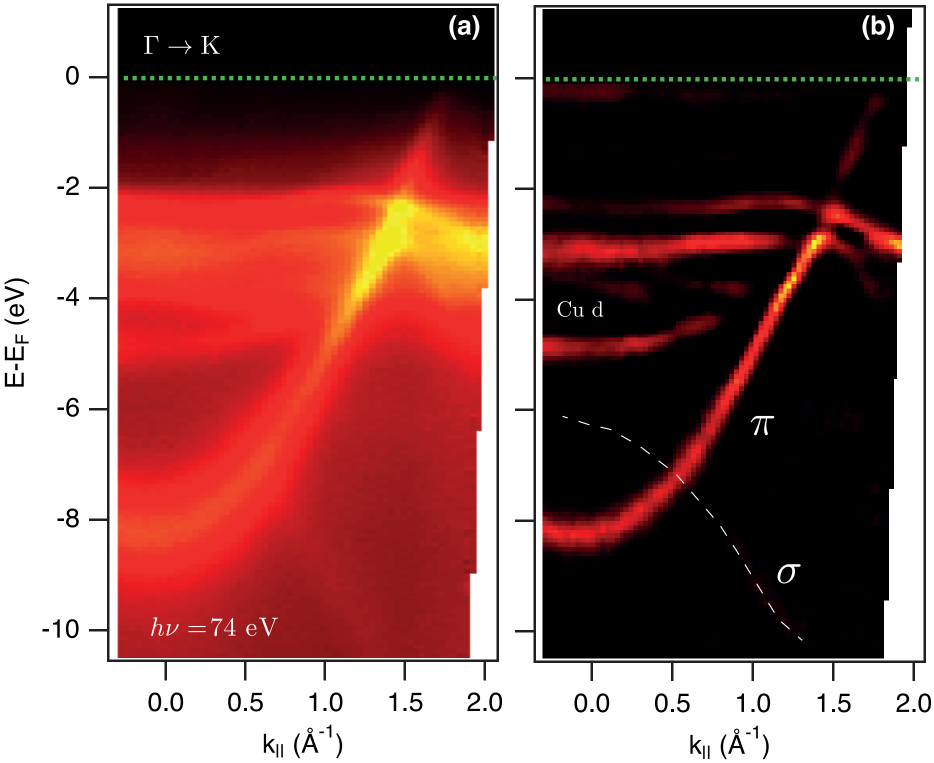

Figure 5.5: (a) ARPES spectra of graphene grown on Cu(111), taken along the $\overline{\Gamma K}$ direction of graphene. The photon energy was 74 eV. (b) Curvature plot of the spectrum shown in panel (a). Lighter colour coresponds to higher photoemission intensity. The origin of the momentum axis corresponds to the position of the Γ point of graphene Brillouin zone. The green dashed line indicates the Fermi level. The white dashed line in panel (b) is a guide for the eye and marks the position of σ band.

samples were annealed in UHV (base pressure 10^{-10} mbar) for 45 minutes at a temperature of about 570 K prior to the acquisition of photoemission spectra. The experiments were carried out at low temperature (T=100 K) in order to minimize the thermal broadening of the spectra.

In figure 5.5-(a), we report an ARPES spectrum showing the valence band structure of the graphene on Cu(111) along the $\overline{\Gamma K}$ high-symmetry direction of the graphene Brillouin zone (BZ). The origin of the momentum axis corresponds to the position of the Γ point of graphene BZ. The photon energy employed was 74 eV, which is very close to the maximum of the photoionization cross section for copper and copper oxide: thus, the measurement was very sensitive to contributions of the copper substrate to the total photoemission signal. In panel (b), we have applied a 2D curvature filter [15] to the spectrum reported in (a), in order to enhance the dispersive band features. Non-dispersive copper d-bands of are found in an interval between 2 and 4 eV below the Fermi level. No Shockley surface state, expected for a clean Cu(111) surface [16], was observed at the Γ point of the Brillouin zone of copper[1]. The π band of graphene is clearly evident and shows a minimum at the centre of the Brillouin zone. Dirac cone is observed and crosses the Fermi level, with a linear dispersion, at about 1.7 Å^{-1} from the centre of the graphene Brillouin zone. A contribution of photoelectrons emitted from the σ band is barely visible at the bottom of the spectrum.

A change of the photon energy to 27 eV enhances the contributions coming from carbon while a reduction of the intensity of the copper bands is expected. Figure 5.6-(a) reports the data as acquired, while in panel (b) a 2D curvature filter was applied, as previously explained. In these graphs, it is possible to unambiguously distinguish the dispersion of the π and σ bands. The Dirac cone, which is crossing the Fermi level at about 1.7 Å^{-1} from the centre of the BZ, is indicated by a blue arrow. Furthermore, an additional dispersing band associated to graphene appears, having a maximum at about 1.45 Å^{-1} from the centre of the Brillouin zone (indicated by a white arrow). The latter value corresponds exactly to the $\overline{\Gamma M}$ distance of the graphene BZ and thus suggests contributions to the photoemission spectrum from domains aligned along $\overline{\Gamma M}$ and $\overline{\Gamma K}$ directions.

We acquired a detailed spectrum of the Dirac cone region (figure 5.7) in order to estimate the interaction of the graphene with the Cu substrate by extracting the Fermi velocity. No apparent doping was observed and the shape of the Dirac cone was unaffected by the presence of the substrate. The dispersion exhibits asymmetric

---

[1] The Shockley surface state at Γ is generally quenched whenever an adsorbate is sorbed on the metallic surface

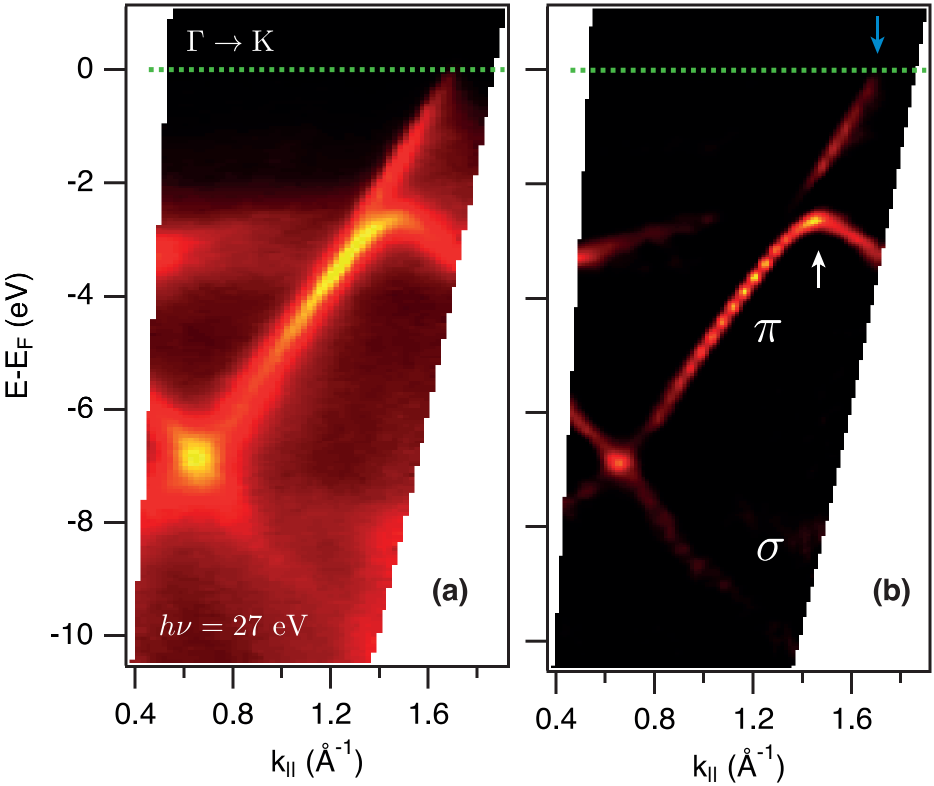

Figure 5.6: (a) ARPES spectrum of graphene grown on Cu(111), taken along the $\overline{\Gamma K}$ direction of graphene. The photon energy was 27 eV. (b) Curvature plot of the spectrum shown in panel (a). Lighter colour coresponds to higher photoemission intensity. The light blue arrow indicates where the Dirac cone crosses the Fermi level. The white arrow points the maximum of a dispersive band, which is located at 1.45 Å^{-1} from the centre of the Brillouin zone. The origin of the momentum axis corresponds to the position of the Γ point of the graphene Brillouin zone. The green dashed line indicates the Fermi level.

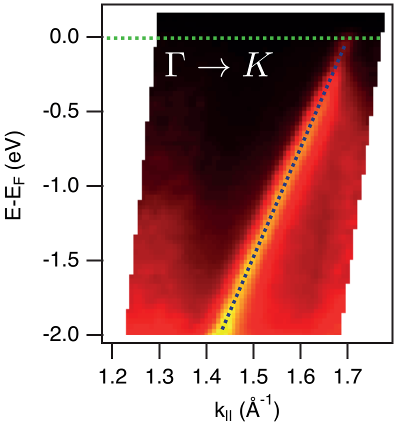

Figure 5.7: Angle-resolved photoemission spectrum acquired in the region of Dirac cone, with a photon energy of 27 eV. The dashed line indicate the best fit used to extract the Fermi velocity.

intensity with respect to the K point: the $\overline{K\Gamma'}$ branch of the cone is not visible. This can be explained by the phase difference of the electrons emitted from A and B sublattices of graphene, which results in a completely destructive interference, as theoretically predicted [17] and observed in earlier ARPES experiments on graphene [18].

Theoretical investigations explored, through a Density Functional Theory (DFT) approach, the band structure of several graphene/metal interfaces [19, 20] and predicted for graphene on Cu(111) a charge transfer from the metal, resulting in a n-doping of graphene of about 200 meV, as a consequence of the weak interaction between the metal and the graphene. By combining the outcomes obtained from ARPES, LEED and XPS measurements, we speculate that for samples prepared according to our growth protocol with 1 hr. of initial reduction in hydrogen, the graphene is supported by a layer of native copper oxide resulting in a lack of doping

Further support to this hypothesis comes from the extraction of the Fermi velocity, whose value probes the interaction with the substrate. The average Fermi velocity can be obtained from the slope of $(E - E_F)$ vs $k_{||}$ in a range of 2 eV below E_F and was found to amount to $v_F = 1.01 \pm 0.09 \times 10^6\ m/s$. This value is very close to the Fermi velocity predicted for free-standing graphene [21] and falls into the range of values reported for suspended graphene samples produced with micromechanical cleaving and investigated with conductivity measurements [22] or angle-resolved photoemission spectroscopy [18, 23]. Therefore, by combining the outcomes from the

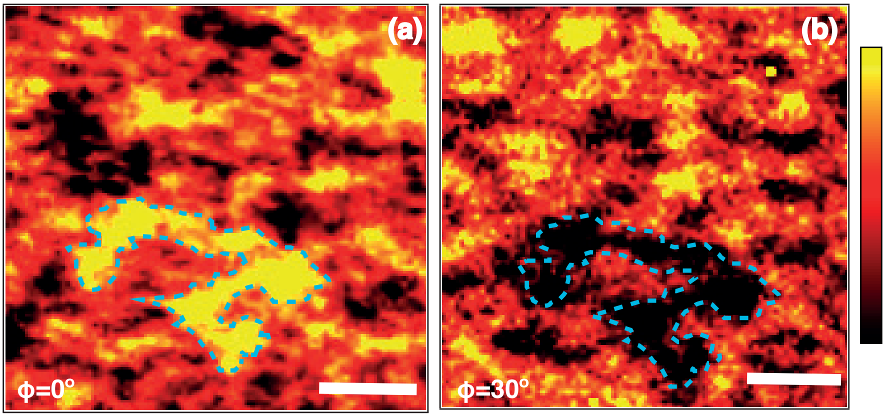

Figure 5.8: Scanning photoemission microscopy maps, acquired with a photon energy of 27 eV by collecting fast photoelectrons, *i.e.* electrons with a binding energy of 1 eV with respect to the Fermi level at azimuthal angle of 0° (panel (a), $\overline{\Gamma K}$ direction) and of 30° (panel (b), $\overline{\Gamma M}$). The scale bars correspond to 10 μm. The two images are presented with the same false colour scale and can be directly compared.

experiments described so far, we infer that the growth of graphene takes place on a layer of native copper oxide. This layer reduces the interaction between the metal and graphene, resulting in a graphene layer whose electronic properties (*i.e.* the Fermi velocity) are comparable to those of a suspended flake. However it must be noted that the band structure was measured only locally (because of the features of Spectromicroscopy beamline) and therefore we cannot directly prove that the graphene/metal interaction is the same in every point of the surface.

As stated earlier, the ARPES spectra suggested the presence of graphene rotated domains (figure 5.6). To gain more information about the presence these rotated domains, we have performed a Scanning-photoemission microscopy (SPEM) investigations, which we show in figure 1.8. SPEM maps were acquired with a photon beam energy of 27 eV by collecting electrons with a binding energy of 1 eV (referenced to the Fermi level) on the same area of the sample but for two different azimuthal angles. Angles of 0° and 30° were chosen because they correspond to the $\overline{\Gamma K}$ and $\overline{\Gamma M}$ high-symmetry directions of the graphene Brillouin zone, respectively. The crystalline domains, which can be identified as areas with the same photoemission intensity, appeared to be extremely different in sizes and orientation. The size ranged from hundreds of nanometers to tens of microns. By inspecting figure 5.8-(a) it appears that it is not possible to establish a preferential azimuthal angle along which the domains grow. In particular, in figure 5.8-(a) one can identify a large area covered with graphene (marked by a dashed blue line), for which the high intensity of the photoemission signal indicates that the azimuthal angle of the analyser matches the $\overline{\Gamma K}$ high-symmetry direction of the Brillouin zone. The image acquired on the same region but with the analyser directed along the $\Gamma - M$ direction (30° azimuth), reported in figure 5.8-(b), shows very low intensity in the area highlighted by the dashed line, demonstrating that this area appears to be monocrystalline. The graphene grown is therefore showing a large extent of azimuthal disorder on the surface, even if some large monocrystalline domains are observed, whereas it is not possible to predict a preferred orientation of growth.

5.5 SCANNING TUNNELING MICROSCOPY INVESTIGATIONS

Scanning photoemission microscopy is an excellent tool for the detection of rotated domains present in a surface lattice. However, the lateral resolution is severely limited by the size of the photon beam spot. Therefore we employed scanning tunneling microscopy (STM) to gain a more detailed insight into the microscopical structural properties of the graphene on such substrate. The sample was introduced into a UHV low-temperature STM (Omicron Nanotechnology). The STM is equipped with a Pt-Ir tip and operates in a UHV chamber with a base pressure of 3×10^{-11} mbar. The sample was annealed before the measurements, analogously to what was done for the ARPES measurements. The measurements were carried out at room temperature.

Figure 5.9-(a) shows a representative STM image. Two main regions can be identified on the surface (delimited by the black dashed line): region A, the top of the micrograph, shows an irregular topography with many smaller or larger protrusions, while in region B large flat terraces are observed. Figure 5.9-(b) presents a detailed STM image of the part framed in green in the region B of panel (a). Here one distinguishes Moiré patterns which are the result of the interference between the graphene and the substrate lattice due to the mismatch between the crystalline lattice parameters of copper (2.55 Å) and of graphene (2.46 Å).

Moiré patterns are typically observed at graphene/metal interface whenever a consistent mismatch between the lattice parameters of the substrate and of the adsorbate is present. The formation of Moiré patterns has been reported for graphene on Ir(111) [24, 25], graphene on Rh(111) [26], graphene on Ni(111) [27, 28], graphene on Ru(0001) [29] and as well for graphene on Cu(111) [30].

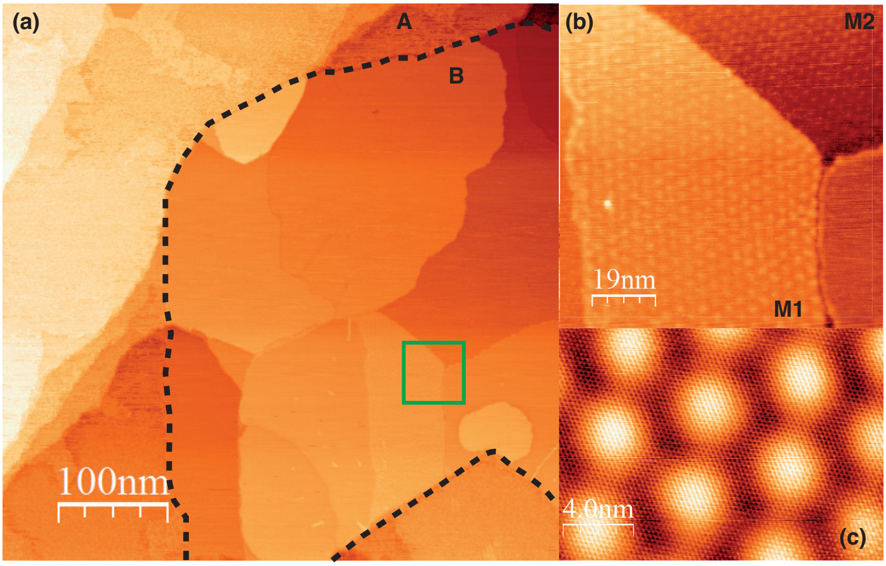

Figure 5.9: (a) STM micrograph of graphene on Cu(111) surface. (b) Detailed image, acquired in the area outlined by a green square in (a), which evidences the presence of a Moiré patterns. (c) Detailed image acquired in the bottom of panel (b), which shows the periodicity of the Moiré pattern and of the graphene layer.

The Moiré patterns in panel (b) have two periodicities, namely 2 nm (M1) and 6 nm (M2). The two patterns were misaligned of about 7° . The same pattern was reported by Gao et al. [30], who investigated graphene grown in situ in UHV by dissociation of ethylene. In panel (c), atomic resolution was achieved (in the region M2) and graphene crystalline lattice (periodicity 2.46 Å) can clearly distinguished.

In other regions of the sample, such as the one depicted in figure 5.10-(a), we could detect areas presenting protrusions similar to what seen in the region A of figure 5.9-(a). Some hexagonally shaped areas are visible such as the one marked by a green square. STM micrographs collected with atomic resolution in such areas (figure 5.10-(b) and (c)) show a hexagonal lattice with an interatomic distance of ca. 2.3 Å. However, no Moiré pattern was observed. This observation enforces the assumption earlier made (based on the XPS, LEED and ARPES data), that in certain parts of the surface a copper oxide layer might be intercalated between the graphene and the metal, preventing the interaction between graphene and copper. However, STM evidences that the distribution of this oxide layer is not homogeneous on the

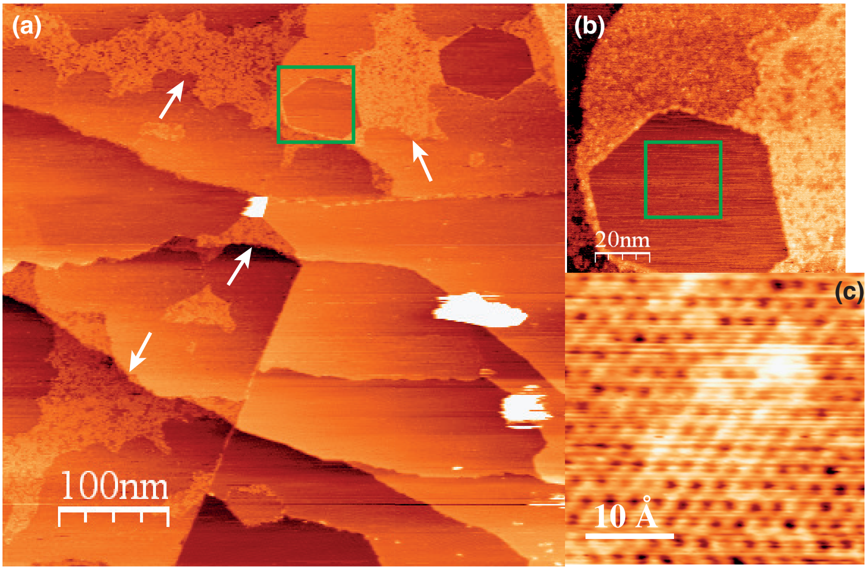

Figure 5.10: (a) STM micrograph of graphene on Cu(111) surface in a region different from the previous image. (b) Detail acquired in the area framed by a green line. (c) Detail acquired in the center of the hexagonal shape in panel (b), showing atomic resolution of graphene but without Moiré pattern.

surface. Areas where the graphene is adsorbed on the clean metal are present and are marked by the presence of a regular moiré pattern.

REFERENCES

[1] D. R. Cooper, B. D'Anjou, N. Ghattamaneni, B. Harack, M. Hilke, A. Horth, N. Majlis, M. Massicotte, L. Vandsburger, E. Whiteway, and V. Yu, *ISRN Condensed Matter Physics* **2012**, 56 (2012).

[2] M. Batzill, *Surface Science Reports* **67**, 83 (2012).

[3] C. Mattevi, H. Kim, and M. Chhowalla, *Journal of Materials Chemistry* **21**, 3324 (2011).

[4] X. Li, W. Cai, J. An, S. Kim, J. Nah, D. Yang, R. Piner, A. Velamakanni, I. Jung, E. Tutuc, S. K. Banerjee, L. Colombo, and R. S. Ruoff, *Science* **324**, 1312 (2009).

[5] G. W. Simmons, D. F. Mitchell, and K. R. Lawless, *Surface Science* **8**, 130 (1967).

[6] F. Besenbacher and J. K. Norskov, *Progress in Surface Science* **44**, 5 (1993).

[7] S. Chen, L. Brown, M. Levendorf, W. Cai, S.-Y. Ju, J. Edgeworth, X. Li, C. W. Magnuson, A. Velamakanni, R. D. Piner, J. Kang, J. Park, and R. S. Ruoff, *ACS Nano* **5**, 1321 (2011).

[8] Y. S. Dedkov, M. Fonin, and C. Laubschat, *Applied Physics Letters* **92**, 052506 (2008).

[9] D. Marchenko, A. Varykhalov, A. Rybkin, A. M. Shikin, and O. Rader, *Applied Physics Letters* **98**, 122111 (2011).

[10] W. R. Salaneck, C. F. Brucker, J. E. Fischer, and A. Metrot, *Physical Review B* **24**, 5037 (1981).

[11] J. Leiro, M. Heinonen, T. Laiho, and I. Batirev, *Journal of Electron Spectroscopy and Related Phenomena* **128**, 205 (2003).

[12] J. Haber, T. Machej, L. Ungier, and J. Ziółkowski, *Journal of Solid State Chemistry* **25**, 207 (1978).

[13] U. Gelius, P. F. Hedén, J. Hedman, B. J. Lindberg, R. Manne, R. Nordberg, C. Nordling, and K. Siegbahn, *Physica Scripta* **2**, 70 (1970).

[14] P. Dudin, P. Lacovig, C. Fava, E. Nicolini, A. Bianco, G. Cautero, and A. Barinov, *Journal of Synchrotron Radiation* **17**, 445 (2010).

[15] P. Zhang, P. Richard, T. Qian, Y.-M. Xu, X. Dai, and H. Ding, *Review of Scientific Instruments* **82**, 043712 (2011).

[16] R. Courths and S. Hüfner, *Physics Reports* **112**, 53 (1984).

[17] E. L. Shirley, L. J. Terminello, A. Santoni, and F. J. Himpsel, *Physical Review B* **51**, 13614 (1995).

[18] K. R. Knox, A. Locatelli, M. B. Yilmaz, D. Cvetko, T. O. Mentes, M. A. Niño, P. Kim, A. Morgante, and R. M. O. Jr., *Physical Review B* **84**, 115401 (2011).

[19] G. Giovannetti, P. A. Khomyakov, G. Brocks, V. M. Karpan, J. van den Brink, and P. J. Kelly, *Physical Review Letters* **101**, 026803 (2008).

[20] P. A. Khomyakov, G. Giovannetti, P. C. Rusu, G. Brocks, J. van den Brink, and P. J. Kelly, *Physical Review B* **79**, 195425 (2009).

[21] A. H. Castro Neto, F. Guinea, N. M. R. Peres, K. S. Novoselov, and A. K. Geim, *Review of Modern Physics* **81**, 109 (2009).

[22] D. C. Elias, R. V. Gorbachev, A. S. Mayorov, S. V. Morozov, P. Zhukov, A. A. Blake, L. A. Ponomarenko, I. V. Grigorieva, K. S. Novoselov, F. Guinea, and A. K. Geim, *Nature Physics* **7**, 701 (2011).

[23] L. Bignardi, W. van Dorp, S. Gottardi, O. Ivashenko, P. Dudin, A. Barinov, J. de Josson, M. Stöhr, and P. Rudolf (2013), submitted to Nanotechnology.

[24] A. T. N'Diaye, J. Coraux, T. N. Plasa, C. Busse, and T. Michely, *New Journal of Physics* **10**, 043033 (2008).

[25] J. Coraux, A. T. N'Diaye, M. Engler, C. Busse, D. Wall, N. Buckanie, F.-J. M. z. Heringdorf, R. van Gastel, B. Poelsema, and T. Michely, *New Journal of Physics* **11**, 3006 (2009).

[26] M. Sicot, P. Leicht, A. Zusan, S. Bouvron, O. Zander, M. Weser, Y. S. Dedkov, K. Horn, and M. Fonin, *ACS Nano* **6**, 151 (2012).

[27] Y. Murata, V. Petrova, B. B. Kappes, A. Ebnonnasir, I. Petrov, Y.-H. Xie, C. V. Ciobanu, and S. Kodambaka, *ACS Nano* **4**, 6509 (2010).

[28] M. Olle, G. Ceballos, D. Serrate, and P. Gambardella, *Nano Letters* **12**, 4431 (2012).

[29] S. Marchini, S. Günther, and J. Wintterlin, *Physical Review B* **76**, 075429 (2007).

[30] L. Gao, J. R. Guest, and N. P. Guisinger, *Nano Letters* **10**, 3512 (2010).

Chapter Six

Microscopic characterization of suspended graphene grown by chemical vapour deposition

We present a multi-technique characterization of graphene grown by chemical vapour deposition (CVD) and thereafter transferred to and suspended on a grid for transmission electron microscopy (TEM). The properties of the electronic band structure are investigated with angle-resolved photoelectron spectromicroscopy while the structural and crystalline properties are studied with TEM and Raman spectroscopy. The suspended graphene membrane locally shows electronic properties comparable with those of samples prepared by micromechanical cleaving of graphite. Measurements show that the area over which high quality suspended graphene is obtained, is limited by the folding of the graphene during the transfer.

The work described in this chapter has been reported in:
L. Bignardi, W.F. van Dorp, S. Gottardi, O. Ivashenko, P. Dudin, A. Barinov, J. Th. M. de Hosson, M. Stöhr and P. Rudolf., Microscopic characterization of suspended graphene grown by chemical vapour deposition, submitted to *Nanoscale*, 2013.

6.1 INTRODUCTION

The growth of graphene on metallic substrates by chemical vapour deposition (CVD) methods is a well-established technique yielding large graphene flakes [1]. In addition, CVD growth is one of the most promising techniques for production on a large and commercially viable scale [2]. Although CVD-grown graphene generally shows lower electron mobility and more defects than graphene produced by the micromechanical cleaving of graphite [1], the easy transfer from the metal substrate to other substrates gives access to many interesting applications [3, 4, 5]. The possibility of using suspended graphene as an ultra-thin membrane in electronic devices and sensors has recently lead to intensive investigations, contributing to reveal outstanding electronic [6, 7, 8, 9, 10] and interesting mechanical properties, *e.g.* high-mechanical strength [11, 12] and micro-filtering properties [13]. Since the interaction with the substrate can strongly modify the electronic structure of graphene [1], in suspended graphene samples one expects the observation of a Dirac-like dispersion [14] at the Fermi level, which is very close to the theoretically predicted dispersion for self-standing single-layer graphene. Furthermore, suspended graphene is suitable for transmission electron microscopy (TEM) experiments, where stable, thin and strong supporting substrates are necessary, *e.g.* to investigate nanoparticles properties [11]. A reliable and non-destructive method for transferring graphene from the metal substrate to a TEM grid has been reported [15], but a complete characterization of these membranes is still lacking.

Herein, we present a study of graphene grown by CVD on copper and subsequently transferred onto TEM grids to produce a suspended layer. Angle-resolved photoemission spectroscopy and microscopy revealed the local electronic structure of this suspended graphene. TEM, electron diffraction and Raman spectroscopy yielded information about the morphology as well as the crystallographic ordering of the suspended areas. These techniques showed that in the suspended areas our samples exhibit single-crystalline domains as well as the electronic structure of non-interacting graphene. In fact, despite the polycrystalline nature of the substrate used for the growth, this graphene exhibits large single-crystalline domains, and, over the suspended areas the characteristic electronic structure of a non-interacting sample. We discuss the role and presence of defects and their influence on the photoemission and Raman spectra and on the diffraction patterns.

6.2 EXPERIMENTAL

Graphene was grown on Cu foil (thickness 25 μm, 99.999% purity, ESPI Metals) in a vacuum furnace (base pressure 10^{-5} mbar). The Cu foil was reduced in a mixture of 0.5 mbar of hydrogen (Messer, purity 5.0) and 0.1 mbar of argon (Linde, purity 5.0) gas for 40 minutes. Afterwards, graphene was grown by exposing the Cu foil to argon (0.1 mbar), hydrogen (0.5 mbar) and methane (0.5 mbar, Messer, purity 4.0) for two min. at a temperature of 1180 K. The sample was subsequently cooled to room temperature in an argon flow (0.09 mbar) at rate of 15 K/min.

Graphene was then transferred to a TEM holey membrane (Quantifoil® 2/2, EMS), which consists of a 200 Au-mesh square grid, covered by a 12 nm thick amorphous carbon film. This film is patterned with 2 μm circular holes. The TEM membrane was placed directly onto the graphene on Cu foil. A droplet of 2-propanol (Merck, 99.95 % purity) was added on top, in order to draw the membrane in close contact with the graphene on Cu foil upon evaporation [15]. The graphene/TEM membrane was then placed in a 5mM solution of $FeCl_3$ in water in order to etch away the copper, leaving the graphene attached to the TEM grid. The TEM grid with the graphene was then rinsed in milliQ water, followed by an annealing in air at 400 K for 5 minutes. A preliminary inspection with scanning electron microscopy showed that the samples consisted of graphene areas which were suspended over 2 μm holes, with a coverage of about 80 % on the entire surface of the sample (not shown).

Angle-resolved photoelectron spectroscopy (ARPES) and Scanning PhotoEmission Microscopy (SPEM) were carried out at the SpectroMicroscopy beamline at the ELETTRA Synchrotron, Trieste, Italy, where the impinging photon beam is focused with Schwarzschild optics resulting in a minimum beam diameter of 600 nm, which makes it suitable for sub-micrometer imaging and spectroscopy [16]. To remove water and contaminants adsorbed during the transfer in air, the samples were annealed in UHV (base pressure 10^{-10} mbar) for 45 minutes at a temperature of about 570 K prior to the acquisition of photoemission spectra. The experiments were carried out at low temperature (T=100 K) in order to minimize the thermal broadening of the spectra.

The TEM images were collected with a JEOL 2010F TEM operated at 200 keV, which is equipped with a field emission gun. The samples were annealed *in vacuo* before image acquisition at a temperature of about 600 K for 20 min. Imaging was done in bright field mode and diffraction patterns were collected with a camera length of 200 mm. All images were recorded with a Gatan CCD camera. The Raman spectra

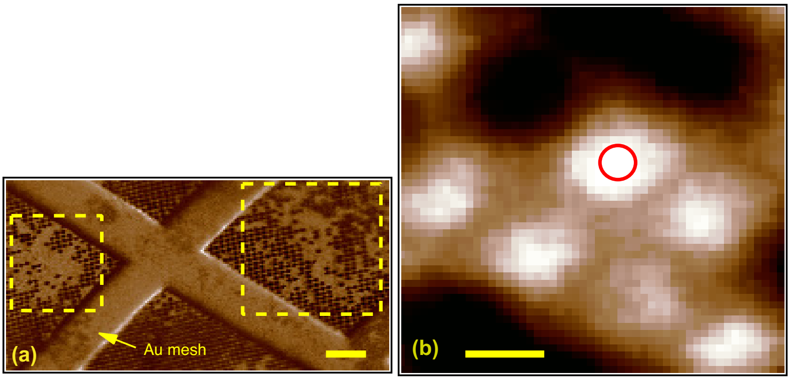

Figure 6.1: (a) Scanning photoemission microscopy (SPEM) map, acquired with a photon energy of 27 eV by collecting fast photoelectrons, *i.e.* electrons with a binding energy of 1 eV with respect to the Fermi level. Areas where a suspended graphene layer is present are marked with a dashed yellow frame. The scale bar corresponds to 20 μm. (b) A more detailed SPEM map acquired under the same experimental conditions in the area marked by the dashed yellow frame on the left in panel (a). The red circle indicates the area where ARPES spectra were acquired. The scale bar corresponds to 2 μm. Brighter areas correspond to higher intensity of the photoemission signal.

were acquired with a Olympus BX51 microscope fiber-coupled to Andor Technology DV420A-BV detector, and a 532 nm laser (25 mW, Cobolt Technology). The laser spot size at the sample was ca. 10 μm with a 50x objective.

6.3 ANGLE-RESOLVED PHOTOELECTRON SPECTROMICROSCOPY

We acquired a series of large-scale SPEM maps, using a photon beam energy of 27 eV and collecting electrons with a binding energy of 1 eV (referenced to the Fermi level). In figure 6.1 a 200×150 μm^2 map is shown. Graphene is present in the areas framed with yellow rectangles. The regular pattern of the holey carbon mesh is not visible there while it is clearly detectable in other areas of the sample.

A more detailed map, acquired within the framed area on the left side of figure 6.1-(a), is presented in figure 6.1-(b); here an area suitable for acquisition of the band structure of the suspended graphene was identified, as indicated by a red circle.

In panel (a) of figure 6.2 we report an angle-resolved photoemission spectrum acquired on suspended graphene, with a photon beam energy of 27 eV, spanning the band dispersions along the $\overline{\Gamma M}$ direction of the Brillouin zone of graphene. To

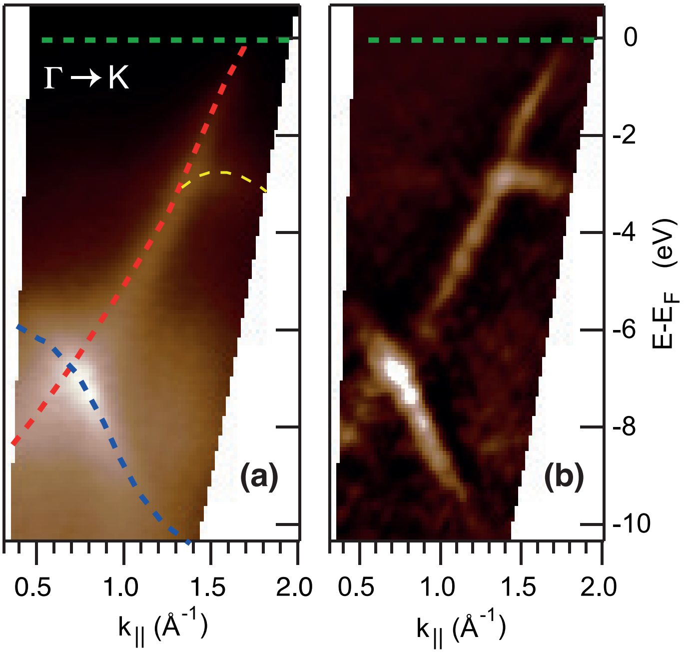

Figure 6.2: (a) Band structure of suspended graphene along the $\overline{\Gamma K}$ direction, taken by angle-resolved photoemission microscopy. The dashed red and blue lines are a guide to the eye and mark the π and σ bands of graphene, respectively, whose shape has been deduced from panel (b). The dashed yellow line marks a branch of π band along the $\overline{\Gamma M}$ direction. The origin of the momentum axis corresponds to the position of the Γ point of graphene. The dashed green line indicates the position of the Fermi level. (b) Same graph as panel (a) after applying a 2D curvature filter to enhance the band structure features

enhance the observed features a false colour scale was used, where brighter colour indicates higher photoemission intensity. The zero of the parallel momentum axis was set at the Γ point of the Brillouin zone of graphene. The σ and π bands of the graphene are marked by dashed red and blue lines, respectively. By applying a 2D curvature filter [17] to the data presented in figure 6.2-(a), the band-structure can be enhanced as shown in figure 6.2-(b). A conical dispersion of graphene π-band centred at the K point of the Brillouin zone can thus be identified. The dispersion looks asymmetric in intensity with respect to the K point: the $\overline{K\Gamma'}$ branch of the cone is not visible. This can be explained by the phase difference of the electrons emitted from A and B sub-lattices, which results in a completely destructive interference, as theoretically predicted [18] and observed in earlier ARPES experiments on graphene [8]. The

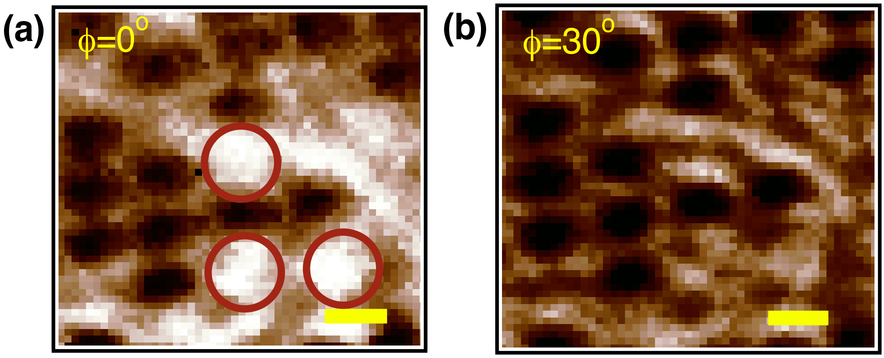

Figure 6.3: Scanning photoemission microscopy map, acquired with a photon energy of 27 eV by collecting fast photoelectrons, *i.e.* electrons with a binding energy of 1 eV with respect to the Fermi level at azimuthal angle of 0° (panel (a)) and of 30° (panel (b)). The scale bars correspond to 2 μm. Brighter areas correspond to higher intensity of the photoemission signal. The two images are presented with the same false colour scale and can be directly compared.

average Fermi velocity can be obtained from the curvature plot of the bandstructure by extracting the slope of $(E - E_F)$ vs $k_{||}$ in a range of 1 eV below E_F and was found to amount to $v_F = 0.97 \pm 0.08 \times 10^6$ m/s. This value is in the range of values reported for graphene samples produced with micromechanical cleaving and investigated with conductivity measurements [19] or angle-resolved photoemission spectroscopy [8].

A further dispersing band, marked with a dashed yellow line as guide to the eye, is observed in panel (a) of figure 6.2. Its vertex lies 2.9 eV below the Fermi level, 1.46 Å^{-1} from the Brillouin zone center Γ. The latter value corresponds exactly to the $\overline{\Gamma M}$ distance and thus suggests contributions to the photoemission spectrum from azimuthally rotated domains. In this case, the graphene area under the photon beam comprised domain boundaries which separated domains aligned along $\overline{\Gamma M}$ and $\overline{\Gamma K}$ directions.

More insight into the distribution of the azimuthally rotated domains is obtained from SPEM at different acquisition angles. Figure 6.3 shows SPEM maps acquired on the same area of the sample but for two different azimuthal angles. Azimuthal angles of 0° and 30° were chosen, because they correspond to the $\overline{\Gamma K}$ and $\overline{\Gamma M}$ high-symmetry directions of the graphene Brillouin zone, respectively. The two images are presented with the same false colour scale and can therefore be directly compared.

Corresponding areas show a different photoemission intensity for the two azimuthal angles, which could indicate that there are several crystalline domains in small portions of the sample. On figure 6.3-(a) one can identify three holes clearly covered with graphene (marked by red circles), for which the high intensity of the photoemission signal indicates that the azimuthal angle of the analyzer matches the $\overline{\Gamma K}$ high-symmetry direction of the Brillouin zone. The image acquired with the analyzer directed along the $\overline{\Gamma M}$ direction (30° azimuth) in the figure 6.3-(b) shows higher intensity at the borders of these holes, indicating that several rotational domains are present in the flakes covering these holes. Furthermore, a higher intensity was also observed in the vicinity of the edges of the graphene flakes for both azimuthal angles. A possible explanation for this may be the contribution from edge states due to the finite size of the graphene layer [20].

6.4 TEM AND RAMAN CHARACTERIZATION

We performed TEM and electron diffraction studies to determine the size and orientation of the crystalline domains of our graphene samples. The TEM micrograph in panel (a) of figure 6.4 shows a region with suspended graphene. The central and the bottom holes are entirely covered with graphene while the two top holes are only partially covered and there the edges of the graphene sheet are folded over, as indicated by the black arrows. A detailed TEM image of a defect-free are is reported in panel (b) while the corresponding electron diffraction pattern is shown in (c) . The single set of hexagonal spots indicates that the graphene membrane is perfectly single-crystalline in this region. Occasionally, as observed on the membrane in the center of figure 6.4-(a) and indicated by the white arrow, we could observe nanoparticles containing copper and iron leftover from the etching procedure[1]. A detailed TEM image and an electron diffraction pattern acquired in a defect-rich area close to an edge of the graphene flake are shown in figure 6.4-(d) and (e), respectively. The diffraction pattern reveals multiple crystalline domains, giving rise to spots arranged along a ring. Systematic study of the TEM images showed that about 50% of the graphene covered holes was showing mono-crystalline features, *i.e.* a pattern like that reported in figure 6.4-(b). We speculate that the diffraction pattern in figure 6.4-(e) could be the results of a multi-crystalline domain graphene and of wrinkles that are forming on the surface, especially in the vicinity of the edges.

These results were confirmed by Raman spectroscopy: the size of the laser beam is larger than the areas with suspended graphene; hence the observed spectrum corresponds to a spatial average over areas with suspended and with supported graphene. In figure 6.5 next to spectrum acquired on the graphene-covered TEM grid (continous

---

[1] The nature of the nano particles has been determined by Energy-dispersive X-ray spectroscopy.

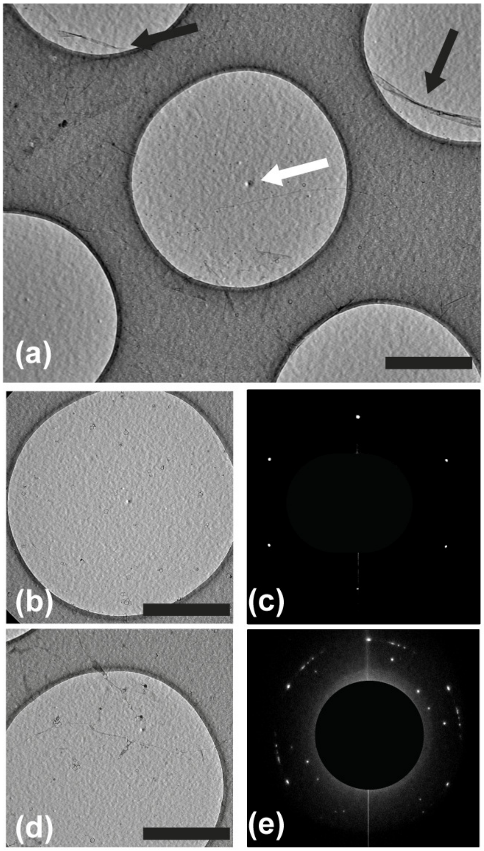

Figure 6.4: (a) TEM micrograph of a suspended graphene sample. The magnification is 30kx. The black arrows point areas where the graphene membrane is folded over itself, at the edges of a flake. The scale bar is 1 μm. (b) Detailed image of a single-crystalline area. (c) Electron diffraction pattern acquired on the area shown in panel (b). (d) Detailed image of a defect-rich area. (e) Electron diffraction pattern acquired on the area shown in panel (d). The non-diffracted beam is masked to enhance the contrast of the diffraction pattern.

blue line) we also report the spectrum acquired on the bare TEM grid (dashed grey line). The prominent peak observed at a shift of 1583 cm^{-1} for the graphene-covered TEM grid corresponds to the G-band, while the peaks at 1358 cm^{-1} and at 2680 cm^{-1} are the D and G′ bands of graphene, respectively [21]. The relative intensity and positions of these peaks were homogeneous on the entire sample surface. The G′ peak could be fitted with a single Lorentzian (FWHM 51.5±1.5 cm^{-1}), confirming that the membrane was composed of single-layer graphene [21]. The G peak displayed a

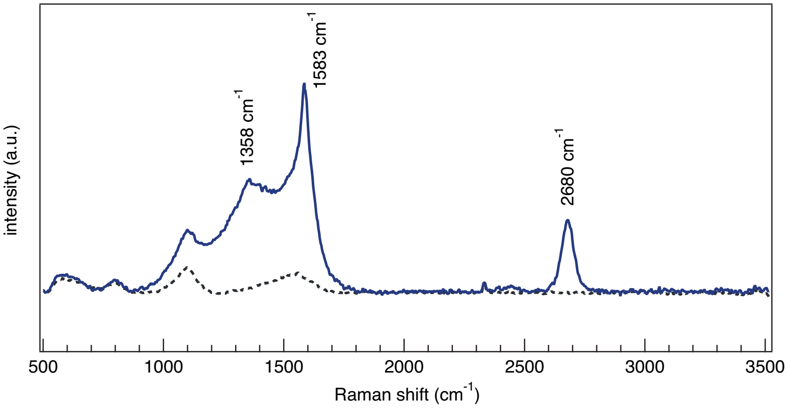

Figure 6.5: Raman spectrum (full line) acquired on graphene covering a holey TEM membrane. The laser spot covered suspended as well as supported graphene areas. The spectrum acquired on the bare holey TEM membrane is also shown (dashed line). The low intensity band at about 2300 cm^{-1} is an artefact of the detector.

shoulder on the left side and did not appear to be as sharp as for graphene obtained by micromechanical cleaving [22]. This might be due to graphene which is locally folded over, as observed in the TEM image discussed above. This hypothesis is supported by the fact that a similar shape of the G peak was observed in single-walled carbon nanotubes [23], where the graphene sheet is strongly curved. The presence of a shoulder on the left side of the D peak is in agreement with what was reported for spectra of edges of graphite and graphene [24, 21]. The bands centerd at 1100, 800 and 600 cm^{-1} are also observed for the TEM grid without the graphene layer and therefore attributed to amorphous carbon [25].

In conclusion, we presented a multi-technique characterization of the local electronic and structural properties of CVD-grown graphene, suspended on TEM grids. The investigated samples displayed electronic properties similar to suspended graphene produced by micromechanical cleaving, with a Fermi velocity close to the theoretical value. Furthermore, our method of CVD growth and stamp-free transfer to the TEM grid was shown to yield suspended graphene membrane areas which in 50% of the cases were single-crystalline over the entire area of each hole in TEM grid. We speculate that the wrinkles and the curvature of the graphene at the edges of the flake, revealed by TEM and Raman spectroscopy, could be the only features that limit the quality in view of a possible future use as ultrathin TEM membranes and in large-scale electronics.

REFERENCES

[1] M. Batzill, *Surface Science Reports* **67**, 83 (2012).

[2] M. J. Allen, V. C. Tung, and R. B. Kaner, *Chemical Reviews* **110**, 132 (2010), pMID: 19610631.

[3] C. Mattevi, H. Kim, and M. Chhowalla, *Journal of Materials Chemistry* **21**, 3324 (2011).

[4] X. Li, W. Cai, J. An, S. Kim, J. Nah, D. Yang, R. Piner, A. Velamakanni, I. Jung, E. Tutuc, S. K. Banerjee, L. Colombo, and R. S. Ruoff, *Science* **324**, 1312 (2009).

[5] X. Li, W. Cai, L. Colombo, and R. S. Ruoff, *Nanoletters* **9**, 4268 (2009).

[6] J. C. Meyer, A. K. Geim, M. I. Katsnelson, K. S. Novoselov, T. J. Booth, and S. Roth, *Nature* **446**, 60 (2007).

[7] K. Bolotin, K. Sikes, Z. Jiang, M. Klima, G. Fudenberg, J. Hone, P. Kim, and H. Stormer, *Solid State Communications* **146**, 351 (2008).

[8] K. R. Knox, A. Locatelli, M. B. Yilmaz, D. Cvetko, T. O. Mentes, M. A. Niño, P. Kim, A. Morgante, and R. M. O. Jr., *Physical Review B* **84**, 115401 (2011).

[9] R. Zan, C. Muryn, U. Bangert, P. Mattocks, P. Wincott, D. Vaughan, X. Li, L. Colombo, R. S. Ruoff, B. Hamilton, and K. S. Novoselov, *Nanoscale* **4**, 3065 (2012).

[10] C. N. Lau, W. Bao, and J. V. Jr, *Materials Today* **15**, 238 (2012).

[11] C. Lee, X. Wei, J. W. Kysar, and J. Hone, *Science* **321**, 385 (2008).

[12] I. W. Frank, D. M. Tanenbaum, A. M. van der Zande, and P. L. McEuen, *Journal of Vacuum Science and Technology B* **25**, 2558 (2007).

[13] J. Bunch, S. Verbridge, J. Alden, A. Van Der Zande, J. Parpia, H. Craighead, and P. McEuen, *Nano Letters* **8**, 2458 (2008).

[14] A. H. Castro Neto, F. Guinea, N. M. R. Peres, K. S. Novoselov, and A. K. Geim, *Review of Modern Physics* **81**, 109 (2009).

[15] W. Regan, N. Alem, B. Alemán, B. Geng, Ç. Girit, L. Maserati, F. Wang, M. Crommie, and A. Zettl, *Applied Physics Letters* **96**, 113102 (2010).

[16] P. Dudin, P. Lacovig, C. Fava, E. Nicolini, A. Bianco, G. Cautero, and A. Barinov, *Journal of Synchrotron Radiation* **17**, 445 (2010).

[17] P. Zhang, P. Richard, T. Qian, Y.-M. Xu, X. Dai, and H. Ding, *Review of Scientific Instruments* **82**, 043712 (2011).

[18] E. L. Shirley, L. J. Terminello, A. Santoni, and F. J. Himpsel, *Physical Review B* **51**, 13614 (1995).

[19] D. C. Elias, R. V. Gorbachev, A. S. Mayorov, S. V. Morozov, P. Zhukov, A. A. Blake, L. A. Ponomarenko, I. V. Grigorieva, K. S. Novoselov, F. Guinea, and A. K. Geim, *Nature Physics* **7**, 701 (2011).

[20] K. Nakada, M. Fujita, G. Dresselhaus, and M. S. Dresselhaus, *Physical Review B* **54**, 17954 (1996).

[21] L. M. Malard, M. Pimenta, G. Dresselhaus, and M. S. Dresselhaus, *Physics Reports* **473**, 51 (2009).

[22] A. C. Ferrari, J. C. Meyer, V. Scardaci, C. Casiraghi, M. Lazzeri, F. Mauri, S. Piscanec, D. Jiang, K. S. Novoselov, S. Roth, and A. K. Geim, *Physical Review Letters* **97**, 187401 (2006).

[23] M. S. Dresselhaus, A. Jorio, M. Hofmann, G. Dresselhaus, and R. Saito, *Nano Letters* **10**, 751 (2010).

[24] L. G. Cançado, M. A. Pimenta, B. R. A. Neves, M. S. S. Dantas, and A. Jorio, *Physical Review Letters* **93**, 247401 (2004).

[25] A. C. Ferrari and J. Robertson, *Philosophical Transactions of the Royal Society of London. Series A: Mathematical, Physical and Engineering Sciences* **362**, 2477 (2004).

Chapter Seven

Thermal depinning of noble gas monolayers on graphene

In this chapter we report on the study of the nanofrictional properties of Xenon monolayers deposited on graphene in a temperature range between 25 and 50 K by means of the quartz crystal microbalance technique. We found that the coverage at which the gas layer starts to slip on graphene/Au increases linearly with decreasing temperature of the substrate while on the bare Au surface no temperature dependence was found. In addition, the slip times measured on gold are much higher than those on graphene. These results are not understood yet and have seeded further experimental and theoretical investigation of the nanotribological properties of graphene, which is currently ongoing.

The work described in this chapter has been reported in:

M. Pierno, L. Bignardi, U. Valbusa, S. Gottardi, M. A. Stöhr, P. Rudolf, and G. Mistura, *Thermal depinning of noble gas monolayers on graphene*, in preparation.

7.1 INTRODUCTION

Graphite is well known to be a very good solid lubricant and is used in a wide spectrum of practical applications. This low-friction behaviour was attributed to the low resistance to shear between the atomic layers of this material [1]. The excellent lubrication properties of graphite, has been widely investigated, mainly by frictional force microscopy experiments [2, 3, 4, 5].

Since graphite lubricates well in a normal air atmosphere, but not at high altitudes or in vacuum it was commonly thought that the low friction properties of graphite rely on the presence of moisture or hydro- carbons which by adsorbing or intercalating weaken of the binding force between basal planes near the surface, thereby allowing these planes to shear easily. Such hypothesis was proven wrong by the results of Yen *et al.* [6], who proved by means of X-ray diffraction that the basal plane spacing of graphite at the surface is the same in vacuum, ambient air, or water vapour-saturated air.

Further investigations [7] of the friction properties at the nanoscale revealed another surprise: when using an atomic force microscope to determine the friction coefficient, it was found that graphite is the first material for which the friction coefficient is negative. This means that friction decreases with increasing normal load. The authors attributed this unusual phenomenon to a reversible partial delamination of the topmost atomic layers, which then mimic few- to single-layer graphene. Other AFM measurements down to single-layer sheets, exfoliated onto a weakly adherent substrate, revealed that friction monotonically increased as the number of layers decreased [8, 9, 10], while, surprisingly, recent studies evidenced how this tendency is inverted when graphene is suspended [11]. The studies above mentioned seem to indicate that the reason for the macroscopic lubricating properties of graphite shall be found in the peculiarity of the crystalline structure of the graphene atomic layers and on the supporting substrate [12].

Despite the recent works described above, much more effort is needed to better understand the frictional properties of graphene and to realize its full potential in tribological applications. In this chapter we report the results of a different approach to study friction on graphene, which does not imply atomic force microscopy but which uses a quartz microbalance to determine the sliding friction of adsorbates on graphene. We have devised a combined chemical-vapour-deposition (CVD) and polymer- stamp-transfer technique for the deposition of graphene on the gold elec-

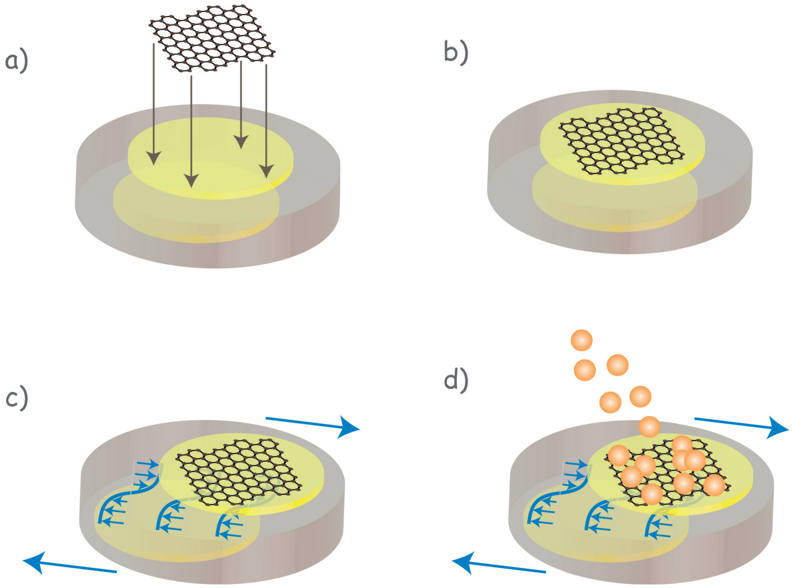

Figure 7.1: Schematic of the experiments depicted in this chapter. (a) and (b), the graphene is prepared and transferred with the help of a PDMS stamp on a face of the Au-covered quartz. (c) The quartz is driven into resonance, by applying an AC voltage at the two Au electrodes. (d) The quartz is cooled down up to LHe temperature and a monolayer of noble gas is deposited on the surface. Image courtesy of M. Pierno.

trodes of a quartz crystal microbalance (QCM) to be used in nanofriction studies.

7.2 QUARTZ MICROBALANCE TECHNIQUE

The quartz crystal microbalance technique (QCM) can be effectively used to probe interfacial phenomena and has been successfully employed to investigate the sliding friction of nanoobjects with moving on the quartz crystal with velocities as large as a few m/s [13, 14].

The microbalance is a small α-quartz disk whose principal faces are optically polished and covered by metal films, which serve at the same time as electrodes and as surfaces on which atoms and molecules can adsorb. Since α-quartz is piezoelectric, by applying an AC voltage across the two electrodes it is possible to drive the crystal to a mechanical resonance where the two parallel faces oscillate in a transverse shear motion. We can define a mechanical "Q-factor" for the crystal, which is written as

$$Q_m = \frac{\omega M_m}{R_m}, \tag{7.1}$$

with ω the driving frequency of the oscillation, M_m the oscillating mass and R_m takes into account effects of a damping force. In the absence of a vapor [15], the slip time τ, which describes the viscous coupling between the substrate and the film, can be easily calculated from the shifts in the resonance frequency and amplitude of the QCM [14]. The slip time represents the time required for the speed of an adsorbed film to decay to 1/e of its initial value after the oscillating substrate has been put to rest and it can be written [16] as

$$\tau_s = \frac{\rho_f d}{\eta} \tag{7.2}$$

where ρ_f is the bulk density of the adsorbate, d the thickness of the layer and η is the lateral viscosity[1]. A very low value of τ indicates a high interfacial viscosity and, in the case of a film rigidly locked to the substrate, τ goes to zero.

The central result achieved by Krim [13] relates the Q factor to the slipping time, according to the relation

$$\delta\left(\frac{1}{Q}\right) = 2\tau_s \delta\omega. \tag{7.3}$$

The quality factor of these resonances is usually very high (10^5) and this explains why the QCM is quite sensitive to interfacial phenomena. A change in the disk's inertia caused for example by the adsorption of a film on the metal electrodes is revealed by a shift in the resonant frequency. Similarly, any dissipation taking place in the system determines a decrease in the resonance amplitude.

In the work described here two significant advantages with respect to a QCM with standard metal electrodes were achieved. Firstly, the average size of the atomic terraces on our graphene-covered electrodes is approximately one order of mag- nitude larger than the best values obtained by depositing metal electrodes on the quartz surface under very controlled conditions [17]. Secondly, the phase diagrams of rare gas monolayers adsorbed on graphite are very well characterized in contrast to the fairly scarce data available for films on metal surfaces [18]. This availability of thermodynamic data allows to directly compare our data with sliding experiments on graphite [19, 20]. Hereafter, we present the results of an extensive QCM study of the sliding of

---

[1] A detailed overview and derivation of the slip time can be found in [16].

Xe monolayers on graphene in the temperature range 20-50 K, which has been little investigated [21] despite its relevance for the two-dimensional phases of adsorbed monolayers [18].

7.3 PREPARATION AND CHARACTERIZATION OF THE GRAPHENE COVERED AU ELECTRODES

Graphene has been grown by CVD on an ultra-pure copper foil (ESPI Metals, purity 99.999%) following the protocol already described in chapter 2. A $0.5 \times 0.5\ \mathrm{cm}^2$ large and 25 μm thick Cu foil was placed in a quartz-tube vacuum furnace (base pressure 10-5 mbar) and reduced in hydrogen (0.5 mbar) and argon (0.1 mbar) gas flow for 60 min at 1180 K; subsequently graphene was grown by exposing the Cu to hydrogen (0.5 mbar), argon (0.1 mbar) and methane (0.5 mbar) for 2 min at the same temperature. This exposure time to methane leads the formation of a single layer of graphene on more than the 95% of the copper surface [48]. The samples were cooled down to room temperature in an Ar flux (0.1 mbar). Following the procedure described in chapter 2, graphene was then transferred onto a polydimethylsiloxane (PDMS) stamp and the copper was etched away by an aqueous solution of $FeCl_3$. After rinsing with milliQ water and drying in a nitrogen flow, the graphene was transferred from the PDMS stamp onto the Au electrode of the quartz crystal by applying pressure and pealing the stamp off. Surface diffraction experiments conducted on suspended graphene prepared with the same growth protocol (results described in chapter 6) indicated that the size of the single crystalline domains range between 0.1 to 10 μm. Moreover, the graphene membrane can be affected by defects (such as dislocations or domains boundaries), which are created when cooling the Cu foil after graphene growth because of the different thermal coefficient of graphene and of copper [22], as discussed in chapter 6. Furthermore, Raman spectroscopy taken on graphene prepared in the same conditions but transferred onto a Si wafer covered by a 300 nm thick SiOx layer (see figure 2.14) indicated that most of the surface is covered by a single layer of graphene. In fact, the G′ peak in the spectra could be fitted with a single Lorenzian peak. The appearance of a D peak revealed that defects are present in the graphene layer. A ratio $I_D/I_G \simeq 0.3$ was detected. By following the approach described in [23], we can estimate that the average distance L_a between two defects in the graphene layer is about 15-20 nm.

The morphology of the graphene-covered Au electrode was investigated by contact-mode atomic force microscopy (AFM) with a Scientec 5100, equipped with silicon n-type cantilever on which a tip with a nominal radius < 10 nm and with a force constant of 0.10 N/m was mounted. The topography and the lateral friction force (LFM) were imaged. The analysis of the micrographswas performed with the help of the WSxM software [24]. Graphene covered about 85-90 % of the Au electrode surface, as determined by means of a combination of AFM and optical microscope imaging.

In Figure 7.2-(a) an AFM micrograph ($3\times3\ \mu\text{m}^2$) of a graphene-covered area of the sample is presented. A rather rough surface is observed and wrinkles in the graphene layer are visible, as indicated by blue arrows. The RMS roughness R_{RMS} is a standard parameter used to describe the roughness of a surface [25] and it is given by the standard deviation of the topography data,

$$R_{RMS} = \sqrt{\frac{\sum_{n=1}^{N}(z_n - \bar{z})^2}{N-1}}$$

where $\bar{z}$ is the average of the z values within the given area, z_n is the current z value, and N is the number of data points within the given area. The RMS roughness extracted from these topography images was 3.0 nm. Panel (b) shows a lateral force microscopy (LFM) micrograph over the identical area of panel (a). The measured lateral friction is homogeneous, except that along the wrinkles, where it appears to be higher. A hole in the graphene membrane (indicated by the black arrow) appears as an area with higher friction. In Figure 7.2-(c) an AFM micrograph of an area at the edge of the Au electrode, partially covered by graphene is displayed. The roughness of this area was uniform, revealing no differences in topography between the covered and uncovered areas and suggesting that graphene is adhering to all the asperities of the Au substrate. The RMS roughness extracted from the AFM topography images on the bare Au surface was 2.5 nm. In the LFM investigation on the same area shown in panel (d), two regions with different friction were identified. Region A shows lower friction compared to region B. A reduced friction on graphene with respect to metal surface is compatible with earlier observations [9].

7.4 FEATURES OF THE EXPERIMENTAL SETUP FOR THE STUDY OF THE NANOTROBOLOGICAL BEHAVIOUR OF GRAPHENE

The QCM measurements were performed by M. Pierno and G. Mistura at the Department of Physics of the University of Padova. The QCM was mounted in an UHV chamber that comprises a jacket designed to house the cold head of a 4 K cryocooler

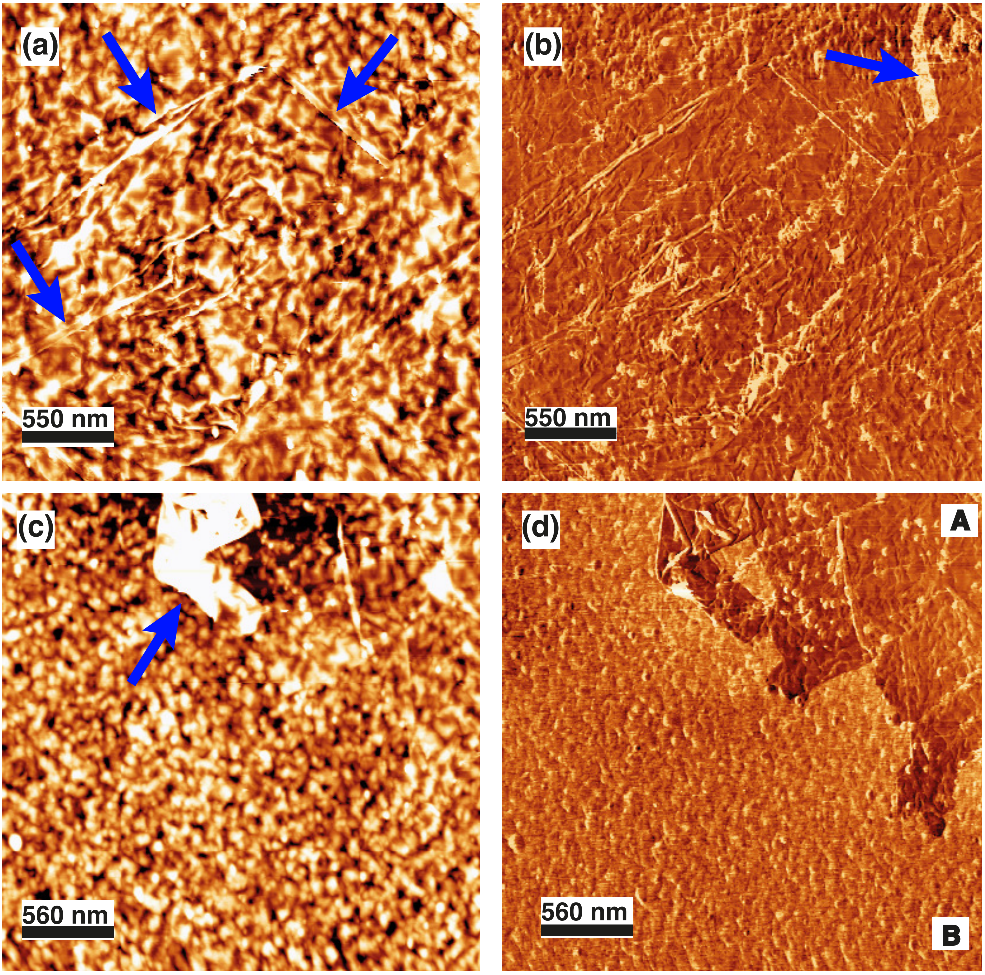

Figure 7.2: Topography (a) and lateral force (b) micrographs of a graphene-covered area on the Au electrode on quartz collected with in contact-mode by AFM. Brighter regions indicate increased height/friction. In the topography image (a) wrinkles on the surface (blue arrows) are evidence of presence of graphene. LFM micrograph (b) shows a homogeneous friction all over the surface, except in correspondence of wrinkles and holes in the graphene membrane (blue arrow). Topography (c) and LFM (d) of an area partially covered by graphene at the edge of the electrode. The observed features and the roughness are comparable those in panel (a). An area where graphene is folded is indicated by the blue arrow. In the LFM micrograph (d) two regions are evident: region A is covered by graphene, while region B represents the bare Au substrate.

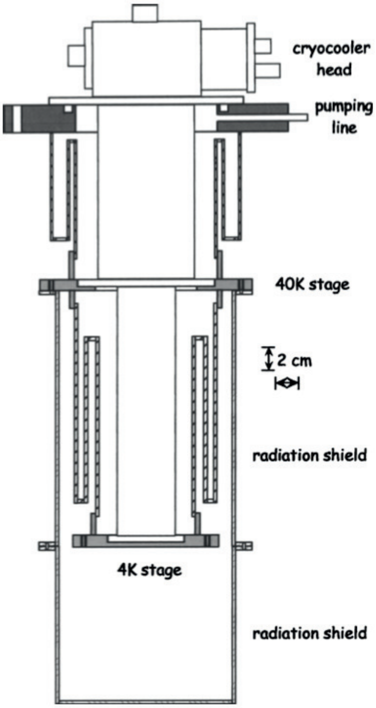

Figure 7.3: Schematic drawing of the low temperature insert jacket. The copper flanges are gray and the stainless steel tubes are hatched. After [26]. © 2005 American Institute of Physics.

[26], as depicted in figure 7.3. Stainless steel spacers thermally decouple the cold head and the QCM holder. The adsorbate layer was condensed directly onto the QCM, kept at the chosen low temperature, by slowly leaking the high-purity gas through a nozzle facing the quartz electrode. The deposition rate can be varied by acting on the leak valve; typical rates range from 20 to 90 min for the deposition of one nominal layer. No systematic differences in the QCM response were observed for this range of deposition rates, suggesting that the data were taken under equilibrium conditions. Between consecutive depositions scans, the QCM was warmed up to about 60 K to guarantee the full evaporation of Xe atoms.

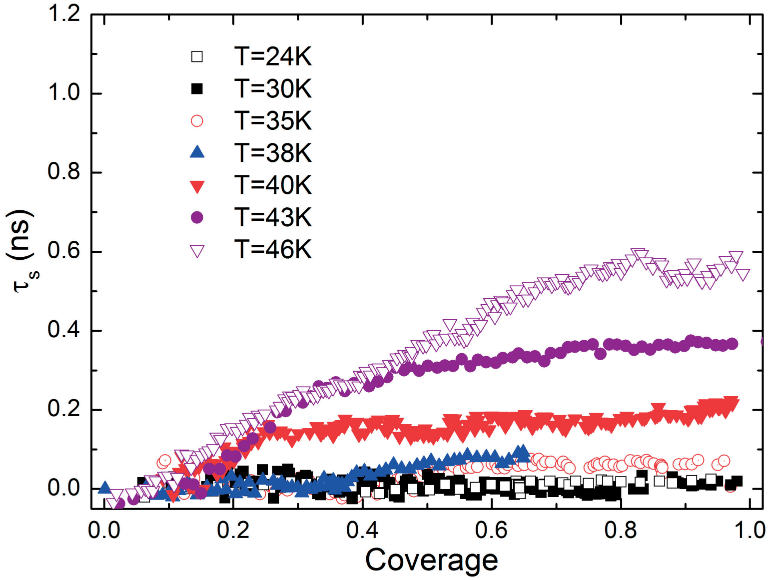

Figure 7.4: Slip time of Xe films on graphene at different temperatures

7.5 ADSORPTION OF A XE MONOLAYER

Figure 7.4 shows the slip time of Xe films deposited on graphene at different temperatures. The film coverage was deduced from the frequency shift assuming for the monolayer an areal density of 5.94 atoms/nm^2 which corresponds to the completion of a solid incommensurate phase on the graphite lattice with nearest-neighbour distance L_{nn} = 0.441 nm [12, 18]. This implies a frequency shift for this monolayer of 7.6 Hz. For each T, the average of a few runs (between 4 and 8 runs, depending on the noise during the measurements) or the most representative scan are reported for the sake of clarity. The data for coverages below 0.1 monolayers are not plotted because of their intrinsic large fluctuations. At temperatures below 30 K, the slip time is zero indicating that the film is completely pinned to the surface. A similar behaviour has been found for a variety of adsorbates deposited on Pb at temperatures below 20 K [27]. As the temperature is increased to 46 K, τ_s is found to increase monotonically while the coverage beyond which the film starts to slide decreases progressively. The corresponding slip time at monolayer completion is 0.5 ns, smaller than the value of 1.7 ns measured at 77 K [12]. This behavior suggests that the increasing temperature

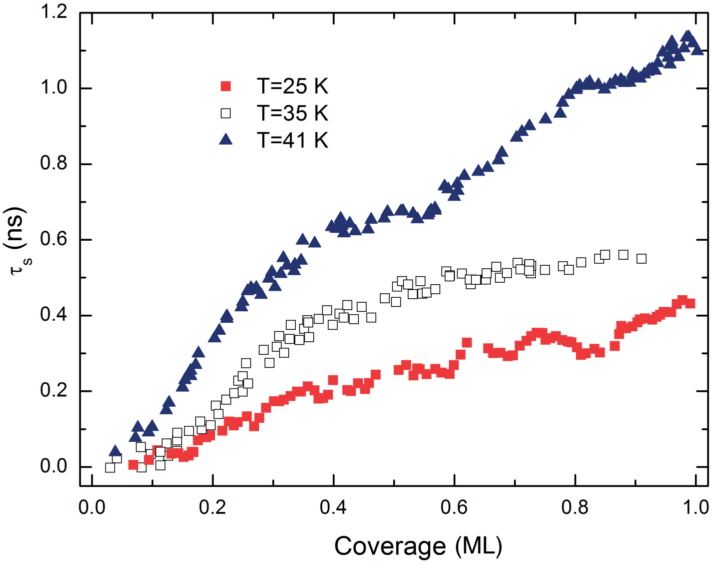

Figure 7.5: Slip time of Xe films on bare Au electrode at different temperatures

favors sliding of the Xe film. Similar thermolubricant effects have been reported for the friction of a contact tip [28].

Beyond this temperature, the evaporation of the Xe film becomes significant due to its relatively high equilibrium vapour pressure. The corresponding slip time at monolayer completion is ca. 0.5 ns, i.e. smaller than the value of 1.7 ns measured at 77 K [12].

The results for an identical experiment but performed on quartz with bare Au electrodes are shown in figure 7.5. The slip times measured on gold are much higher than those on graphene and the pinning coverage is practically zero even at T = 25 K.

We have sketched some possible explanation to motivate this observation. Firstly, the cause of this difference might be the enhanced pinning of Xe atoms at the boundaries of the crystalline domains of graphene.

Another possibility is related to the higher corrugation of the surface potential on graphene with respect to gold. Recent QCM experiments of Xe on a variety of metallic electrodes have verified that the measured slip time is inversely proportional to U_0^2, where U_0 is defined as the amplitude of the periodic function describing the changes in adsorbate-substrate potential with respect to adsorbate position. The value of U_0

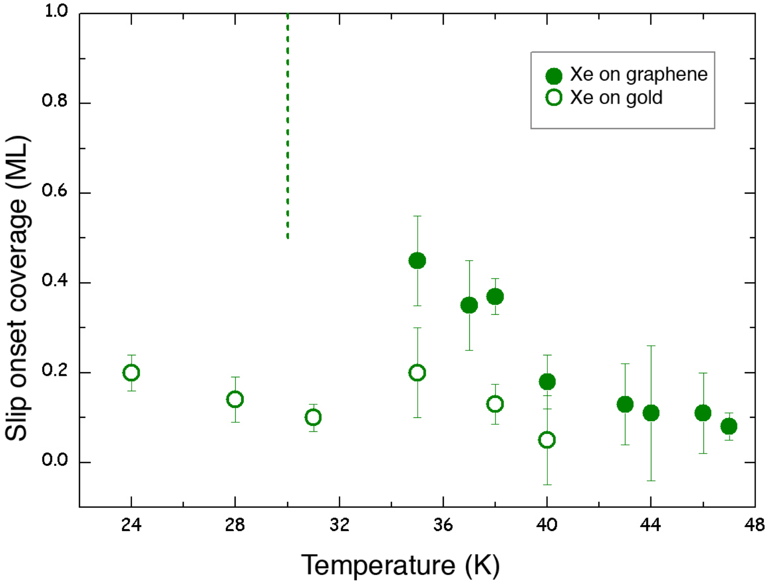

Figure 7.6: Slip onset coverage vs temperature for the Xe monolayer on graphene (filled dots) and on bare Au electrode (empty dots).

for the system Xe/Gr is 5.3 meV [12] while there is no corresponding value in the literature for the Xe/Au system.

The corrugation amplitude U_0 for Xe and N_2 on gold and graphene has been estimatedusing an *ab-initio* scheme based on the recently-developed nonlocal rVV10 density functionals [29] including an accurate description of van der Waals effects implemented in the QE package[2]. These calculations have been carried out by Prof. Pierluigi Silvestrelli at the University of Padova (Italy).

We have considered the interaction of a Xe atom with the ideal, planar single layer of graphene and the Au(111) surface. The computed U_0 value for Xe on graphene, 2.2±0.3 meV, compares favorably with the experimental estimate of Coffey and Krim [12]. Such value is significantly larger than what predicted for Xe/Au (1.6±0.3 meV), thus supporting the explanation based on the higher corrugation of the surface potential on graphene than on gold.

---

[2] www.quantum-espresso.org

Figure 7.6 shows the slip onset coverage as function of the temperature of the QCM; this is the coverage at which the gas layer starts to slip on the surface. The green filled dots indicate data acquired on the graphene-covered Au electrode, while the empty dots refer to data taken on the bare Au electrode. The error bars refer to the standard deviation of data taken in different measurement runs.

The slip onset can be retrieved by measuring the modification in the quartz oscillation amplitude: an amplitude reduction points to energy dissipation in the system, which, in our conditions, can happen only between the Xe film and the underneath substrate (graphene covered Au or bare Au). We point out that, due to large fluctuations in τ_s for coverages below 0.1 ML, the depinning onset ΔV_n has been deduced by considering

$$\Delta V_n = (V_0 - V)/V_0 \tag{7.4}$$

where V_0 is the resonance amplitude at zero coverage and V is the measured resonance amplitude while dosing the Xe. The slip onset measured on graphene increases linearly with decreasing temperature of the substrate. This is indicative of a thermal depinning transition with a characteristic temperature of $30 \pm 3\ K$ for Xe monolayers on graphene (indicated by the green dashed line in figure 7.6). On the contrary, the slip onset on the bare Au electrode does not change with the temperature.

At the present state, a comprehensive explanation for the sliding behaviour of Xe monolayers on graphene is still lacking. Theoretical modeling of this phenomenon is currently under development in order to rationalize the observed data. Defects and domain boundaries in the graphene layer might contribute to the nanofrictional properties, acting as preferential sites for the adsorption of the Xe atoms. However, this hypothesis is not confirmed and the role of the defects is not clearly understood yet.

REFERENCES

[1] B. Kelly, *Physics of Graphite*, RES mechanica monographs, Kluwer Academic Pub (1981).

[2] C. M. Mate, G. M. McClelland, R. Erlandsson, and S. Chiang, *Physical Review Letters* **59**, 1942 (1987).

[3] J. Ruan and B. Bhushan, *Journal of Materials Research* **8**, 3019 (1993).

[4] R. Buzio, E. Gnecco, C. Boragno, and U. Valbusa, *Carbon* **40**, 883 (2002).

[5] M. Dienwiebel, G. S. Verhoeven, N. Pradeep, J. W. M. Frenken, J. A. Heimberg, and H. W. Zandbergen, *Physical Review Letters* **92**, 126101 (2004).

[6] B. K. Yen, B. E. Schwickert, and M. F. Toney, *Applied Physics Letters* **84**, 4702 (2004).

[7] Z. Deng, *Nature Materials* **11**, 1032 (2012).

[8] C. Lee, Q. Li, W. Kalb, X. Z. Liu, H. Berger, R. W. Carpick, and J. Hone, *Science* **328**, 76 (2010).

[9] T. Filleter, J. L. McChesney, A. Bostwick, E. Rotenberg, K. V. Emtsev, T. Seyller, K. Horn, and R. Bennewitz, *Physical Review Letters* **102**, 086102 (2009).

[10] T. Filleter and R. Bennewitz, *Physical Review B* **81**, 155412 (2010).

[11] Z. Deng, N. N. Klimov, S. D. Solares, T. Li, H. Xu, and R. J. Cannara, *Langmuir* **29**, 235 (2012).

[12] T. Coffey and J. Krim, *Physical Review Letters* **95**, 076101 (2005).

[13] J. Krim and A. Widom, *Physical Review B* **38**, 12184 (1988).

[14] J. Krim, D. H. Solina, and R. Chiarello, *Physical Review Letters* **66**, 181 (1991).

[15] L. Bruschi and G. Mistura, *Physical Review B* **63**, 2354111 (2001).

[16] L. Bruschi and G. Mistura, in E. Gnecco and E. Meyer, editors, *Fundamentals of Friction and Wear*, NanoScience and Technology, 35–47, Springer Berlin Heidelberg (2007).

[17] L. Bruschi, G. Fois, A. Pontarollo, G. Mistura, B. Torre, F. Buatier de Mongeot, C. Boragno, R. Buzio, and U. Valbusa, *Physical Review Letters* **96**, 216101 (2006).

[18] L. W. Bruch, R. D. Diehl, and J. A. Venables, *Review of Modern Physics* **79**, 1381 (2007).

[19] N. Hosomi, A. Tanabe, M. Suzuki, and M. Hieda, *Physical Review B* **75**, 064513 (2007).

[20] N. Hosomi, J. Taniguchi, M. Suzuki, and T. Minoguchi, *Physical Review B* **79**, 172503 (2009).

[21] M. F. Danişman and B. Özkan, *Review of Scientific Instruments* **82** (2011).

[22] X. Li, W. Cai, J. An, S. Kim, J. Nah, D. Yang, R. Piner, A. Velamakanni, I. Jung, E. Tutuc, S. K. Banerjee, L. Colombo, and R. S. Ruoff, *Science* **324**, 1312 (2009).

[23] M. M. Lucchese, F. Stavale, E. H. M. Ferreira, C. Vilani, M. V. O. Moutinho, R. B. Capaz, C. A. Achete, and A. Jorio, *Carbon* **48**, 1592 (2010).

[24] I. Horcas, R. Fernández, J. M. Gómez-Rodríguez, J. Colchero, J. Gómez-Herrero, and A. M. Baro, *Review of Scientific Instruments* **78** (2007).

[25] K. Boussu, B. V. der Bruggen, A. Volodin, J. Snauwaert, C. V. Haesendonck, and C. Vandecasteele, *Journal of Colloid and Interface Science* **286**, 632 (2005).

[26] L. Bruschi, A. Carlin, F. B. De Mongeot, F. Dalla Longa, L. Stringher, and G. Mistura, *Review of Scientific Instruments* **76**, 023904 (2005).

[27] M. Pierno, L. Bruschi, G. Fois, G. Mistura, C. Boragno, F. B. de Mongeot, and U. Valbusa, *Physical Review Letters* **105**, 016102 (2010).

[28] S. Y. Krylov and J. W. M. Frenken, *Journal of Physics: Condensed Matter* **20**, 354003 (2008).

[29] R. Sabatini, T. Gorni, and S. de Gironcoli, *Physical Review B* **87**, 041108 (2013).

Chapter Eight

Image potential states at the graphene/Cu interface

Surface states at the weakly coupled interface graphene/copper have been investigated by non-linear angle resolved photoemission spectroscopy. Comparing the spectra collected on graphene grown on Cu(111) and on copper polycrystalline foil, we are able to identify the Shockley surface state and the n=1 image state of the Cu(111) surface and the symmetric $n = 1$ image state of the single layer of graphene.

The work described in this chapter was reported in:
S. Tognolini, L. Bignardi, S. Pagliara, G. Galimberti, P. Rudolf, F. Parmigiani, *Image potential states at the graphene/Cu interface*, in preparation.

8.1 INTRODUCTION

Extensive studies have been carried out in the last years in order to describe the interaction of graphene with metallic substrates. The occupied electronic states of graphene on different substrates have been carefully investigated in the vicinity of the Fermi level, where (self-standing) graphene exhibits a zero-band gap with linear band dispersion, forming a Dirac-cone at the K-points of its Brillouin zone [1, 2]. On the other hand, the unoccupied electronic states of the graphene/metal interfaces have not been characterized or discussed in detail yet, in spite of their relevance for the electrical and optical properties. Image potential states (IPS) are particularly relevant among the unoccupied states; similarly to the π bands of graphene, they are expected to depend sensitively on the graphene-metal interaction. These states, due to the large spatial expansion into the vacuum of the associated wavefunctions, can provide a very sensitive tool for understanding the coupling of graphene with the substrate [3, 4, 5].

A remarkable consequence of the graphene two-dimensional (2D) character is the occurrence of two series of IPSs at the Brillouin zone center, as predicted by ab-initio band structure calculations [6, 5]. This is different from what is observed for surfaces of three-dimensional (3D) solids where only one such series of states exists [7, 8]. For the two series in graphene, the wavefunctions of the states have opposite parity with respect to the reflection at the graphene plane. The state with a symmetric wave function, n^+, shows a lower energy compared with the state with anti-symmetric wavefunction, n^-, (for each n integer). The upper anti-symmetric $n = 1$ IPS (1^-–IPS) displays a spatial expansion towards the metal interface region and evolves, with increasing number of carbon layers, into the $n = 1$ IPS of graphite. The 1^+–IPS, which shows a larger weight towards the vacuum, evolves into the interlayer band of graphite and therefore it is believed to be responsible of the superconducting properties to intercalated graphite compounds. When few layers are stacked together to form a quasi-bidimensional solids, the inner layers IPSs hybridize generating interlayer states. This mechanism has been observed in intercalated graphite compounds [9], carbon nanotubes [10, 11], fullerenes [12, 13] and fullerites [13], where the IPSs hybridize into a Super Atomic Molecular Orbital (SAMO).

Based on the results reported so far and as recalled in the introduction to this thesis, graphene/metal interfaces can be divided in two categories: strongly and weakly interacting. A strong interaction between metal and graphene, such as for Ru and Ni, entails a small distance between metal and graphene, much smaller than graphene planes separation in graphite, and leads to an alteration of the graphene π band, with a shift to higher binding energy and opening of a band gap. For graphene deposited on a weakly interaction substrate, *e.g.* Ir and Cu, the predicted graphene–metal separation is about 3.3 Å [14, 15, 16, 17], *i.e.* similar to the distance between graphene layers in graphite [18]. The π band remains almost undisturbed with the Dirac cone at the K-point intact, whereas small doping effects can be observed [16].

Surface states comparable to those of the clean metal surface were observed both in weakly and strongly interacting systems [14, 19]. In the former, the metallic surface state appears essentially unchanged by the presence of graphene. Despite of a strong corrugation at the interface, the strongly interacting graphene/Ru interfaces , shows a series of unchanged slightly decoupled image-potential states and the IPS is characterized by a larger binding energy compared to that measured for the same state on HOPG, a shorter lifetime, and a higher effective mass.

In this work, we studied the properties of IPSs at graphene-Cu interface by means of angle-resolved non-linear photoemission, employing femtosecond laser pulses as photon source. This technique is a powerful tool in the investigation of the unoccupied electronics states at surfaces, allowing to change both the photon energy and the polarization of excitation source. By comparing the results obtained on graphene/Cu(111) and on graphene grown on Cu foil, we were able to measure, for the first time, the symmetric n=1 IPS of a single layer of graphene and to unambiguously discriminate between the graphene IPS and the surface states of the metal. The binding energy and the effective mass of this state were measured and compared with those of graphite in order to understand the role of the interaction with the metallic substrate.

8.2 EXPERIMENTAL

The protocol of growth of graphene on copper was similar to what already described in the previous chapters. Graphene was grown on a Cu(111) single crystal (MaTeck) that was previously Ar-sputtered (E_b=1 keV) and annealed (650 K) in ultrahigh vacuum. The crystal was then transferred (through air) into a vacuum furnace (base pressure 10-5 mbar), where it was reduced in a mixture of 0.5 mbar of hydrogen (Messer, purity 5.0) and 0.1 mbar of argon (Linde, purity 5.0) gas for 4 hrs. at a temperature of 1250 K before graphene was grown by exposing to argon (0.1 mbar), hydrogen (0.5 mbar) and methane (0.5 mbar, Messer, purity 4.0) for two min at 1250 K. The sample was subsequently cooled to room temperature in an argon flow (0.09

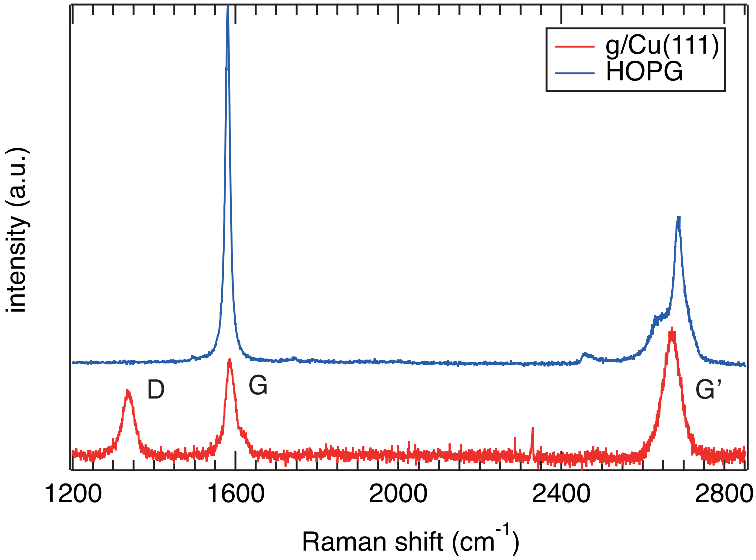

Figure 8.1: Raman spectrum of graphene/Cu(111) and of HOPG. The relevant peaks of the graphene spectrum are marked. The excitation wavelength employed was 633 nm.

mbar) at a rate of 15 K/min. The Cu foil (thickness 25 μm, 99.999% purity, ESPI Metals) was etched in a 0.25 M solution of H_2SO_4 in water for 5 min, rinsed in water and ethanol, dried in an argon flow and transferred to the vacuum furnace. The growth of graphene followed the same protocol described above for the growth on Cu(111).

A LEED pattern similar to what shown in figure 5.2 was observed for graphene grown on Cu(111). Furthermore, Raman spectroscopy was used to characterized the deposited graphene. We employed a Raman setup (Renishaw), working with a 633 nm He-Ne CW laser. The output average power was 50 mW and the spot size was below 1 μm.

The resulting spectrum is shown in figure 8.1, together with a spectrum acquired on HOPG for comparison. We identified three main peaks at 1336, 1586 and 2670 cm^{-1}, which we labeled D, G and G′. The G and G′ peaks are characteristic of a graphitic layer. The G′ could be fitted with a single Lorentzian peak (width= 49±7 cm^{-1}), indicating that a single layer of graphene grew on the copper surface. The presence of peak D with an intensity comparable to peak G suggests the presence of grain boundaries and defects in the layer. This is in agreement with the LEED pattern

Figure 8.2: Electron back scattering diffraction map acquired on a graphene/Cu foil sample.

5.2, which suggested the present of domains with different crystalline orientation in the graphene layer.

The crystalline orientation of the copper foil substrate was checked by Electron-Back-Scattering Diffraction (EBSD). Crystalline domains with sizes ranging from 100 to 1000 μm with a dominant crystalline orientation close to (001) were observed.

For non-linear angle resolved photoemission measurements, we used a Ti:Sapp laser system delivering 0.8 mJ, 150 fs pulses at a wavelength of 790 nm and 1 kHz repetition rate. A schematic of the setup is shown in figure The laser pulses were also used to pump a travelling wave optical parametric amplifier covering a wavelength range from 0.80 eV to 1.07 eV. By quadrupling the output of the parametric amplifier the photon energy could be tuned continuously from 3.20 eV to 4.28 eV, although the fluence was adjusted only over a limited range (around 100 μJ/cm^2). The near-UV pulses were focused then on the sample, which was kept in an UHV chamber at a residual pressure < 2×10^{-10} mbar. Photoelectrons were detected by a custom-made time of flight (ToF) electron spectrometer with an angular acceptance of ± 0.85° and an overall energy resolution of 35 meV at an electron kinetic energy (EK) of 2.0 eV. The experimental geometry and the available photon energies allowed the investigation of the parallel crystal momenta in a range of ± 0.3 Å^{-1} around $k_{||}$ = 0 (normal emission). The angle of incidence of the laser beam with respect to the surface normal was θ = 30°. Therefore, while the s-polarized ligth beam had electric field E parallel to the sample surface (horizontal component), the p-polarized beam

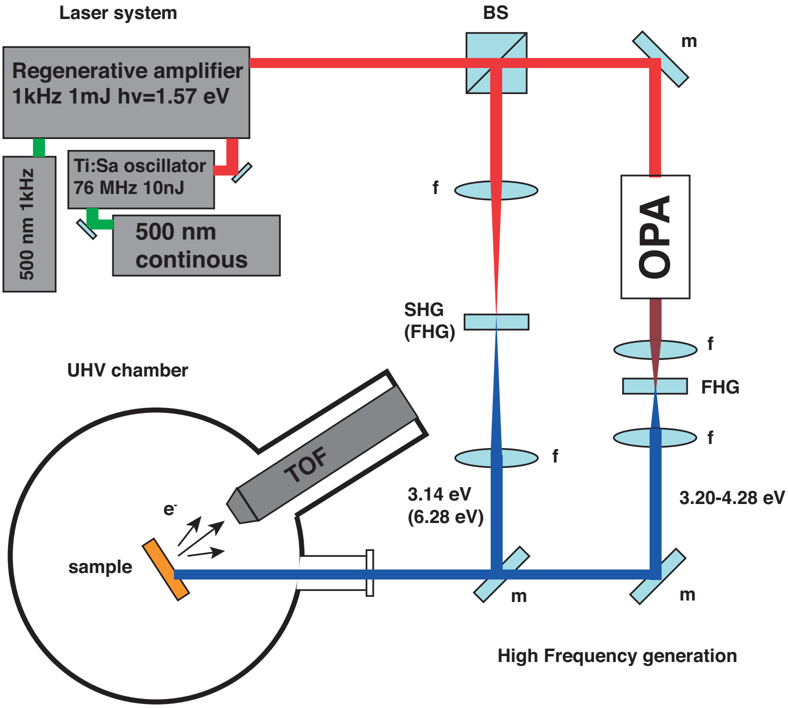

Figure 8.3: Schematic of the setup used for the acquisition of 2PPE spectra on graphene/Cu. See the text for details. Adapted from [20]

displayed a horizontal component given by a $E_h = |E| \cos \theta$ and a vertical component given by $E_v = |E| \sin \theta$. All measurements were performed at room temperature.

8.3 IMAGE POTENTIAL STATES AT THE GRAPHENE/CU(111) INTERFACE

Fig. 8.4-(a) shows non-linear photoemission spectra on graphene/Cu(111) acquired with p- and s-polarized light, with a photon energy $h\nu = 4.05$ eV. The d-band of Cu(111) were identified at about 2 eV kinetic energy (KE) and three features were observed, figure 8.4-(b) and labeled IS1 (3.0 eV), IS2 (3.5 eV) and SS (4.0 eV). Remarkably, the three features vanished when the laser beam was switched to s polarization indicating that these states posses the expected symmetry for surface states [21].

To distinguish the structures belonging to occupied states, a linear photoemission spectrum on graphene/Cu(111) was recorded ($h\nu$=6.3 eV) and it is shown in Fig. 8.5-

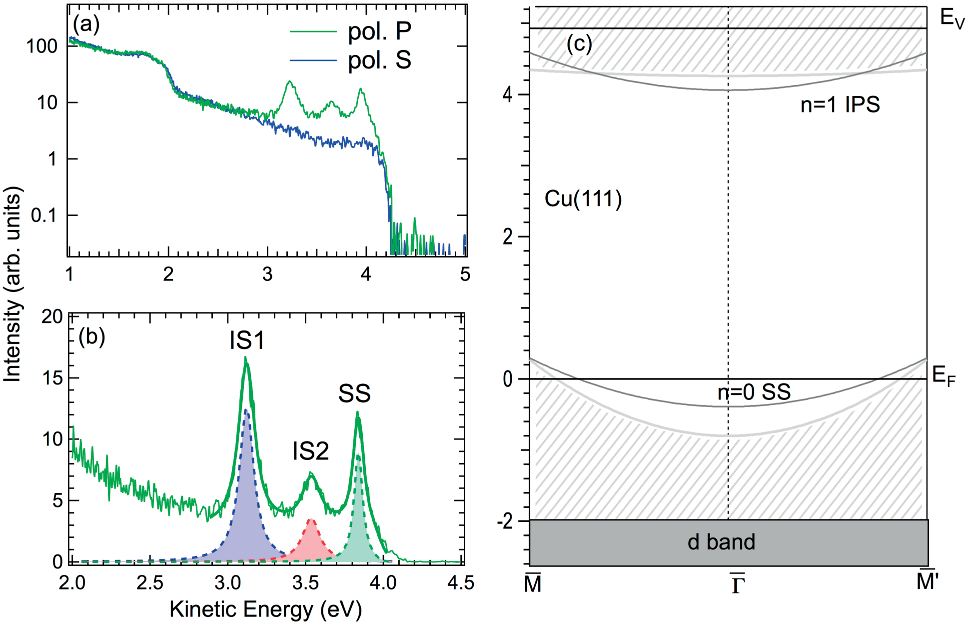

Figure 8.4: (a) Non-linear photoemission spectra collected at normal emission ($k_{||} = 0$) with a photon energy of 4.05 eV in s and p polarization. Three structures labelled IS1, IS2 and SS (b) were obserbed with p-polarized light and resulted completely quenched when switching to s polarization. (c) Projected band structure of clean Cu(111)

(a). Only one structure was observed at about 0.2 eV below the Fermi level, which suggests an assignment to the Schockley surface state of Cu(111) (fig. 8.4-(c)). This assignment is in agreement with previous results reported on graphene/Ir(111) [14], where the Shockley surface state was not quenched by the graphene layer due to the large distance (3-3.5 Å) between the metal and the graphene and because the probability density associated with the Schockley state is maximized at the metal surface.

The binding energy of the SS state is shifted with respect to the Shockley surface state on clean Cu(111) by about 0.2 eV (fig. 8.4-(c)). A similar effect was reported also for graphene grown on Ir(111) [14] and it is consistent with a charge transfer process from the metal to graphene caused by differences in work function [17]. This charge transfer does not entail any hybridization or chemical bonding. We determined whether the intrinsic linewidth and the effective mass associated with the SS

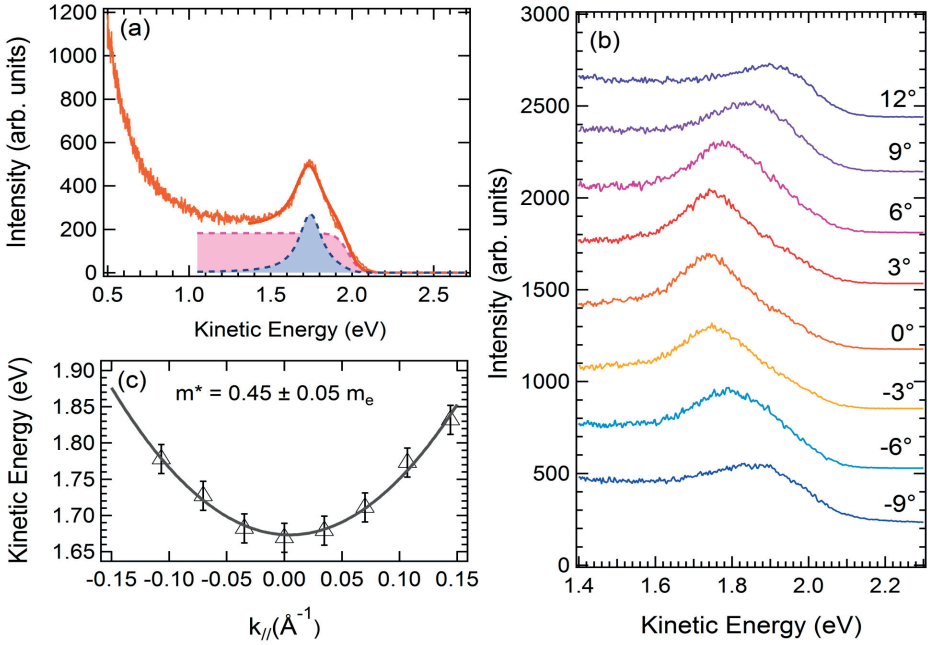

Figure 8.5: (a) Linear photoemission spectrum collected at normal emission ($k_{||}$=0) with a photon energy of 6.3 eV and p polarized light. (b) Angular dispersion of the photoemission spectra collected at $h\nu$ = 6.3 eV. (c) Kinetic energy versus $k_{||}$-momentum for the Shockley surface state (triangle). A parabolic fit (line) gives an effective mass of 0.45 ± 0.05.

were consistent with those of clean Cu(111) surface to confirm the proposed assignment. In fig. 8.5-(c) the SS energy position, measured by varying the angle between the sample and the direction of electron detection (fig. 8.5-(b)), are displayed as a function of parallel momentum ($k_{||}$). The SS effective mass evaluated by fitting the data with a parabolic function was found to be $m^* = 0.45 \pm 0.05\ m_e$, which is very similar to the value $0.46 \pm 0.04\ m_e$ measured on clean Cu(111). Moreover, the intrinsic linewidth at normal emission (70 ± 5 meV), measured by fitting the SS with a Lorentzian convoluted with a Gaussian function to take into account the experimental resolution, was found to be consistent with the value recorded for the surface state on the clean metal (50 ± 5 meV) [24, 22].

Considering the linear photoemission spectrum, we can suppose that the features IS1 and IS2 of fig.8.4 can be assigned to unoccupied image potential states of the

	Φ (eV)		SS	IS1	IS2
Cu(111) [22]	4.9	BE (eV) m^*/m_e	0.43 0.4	0.9 1.3	-
HOPG [23]	4.5	BE m^*/m_e	-	-	0.85 ± 0.1 1.0
G/Cu(111)	4.2 ± 0.1	BE m^*/m_e	0.24 ± 0.05 0.45 ± 0.05	0.90 ± 0.05 0.9 ± 0.1	0.50 ± 0.05 1.3 ± 0.1

Table 8.1: Summary of features of surface states at Γ point of the Brillouin zone of Cu(111), HOPG and G/Cu(111). The states are named according to the convention used so far in the chapter. BE indicates the binding energy of the state with respect to the Fermi level for the SS state and with respect to vacuum level for IS1 and IS2.

graphene/Cu(111) interface. Both Cu(111) and graphite show image potential states in their projected band structure, whose measured binding energy and effective mass are reported in table 8.1, together with those determined for the graphene/Cu(111) interface.

8.4 IMAGE POTENTIAL STATES AT THE GRAPHENE/CU FOIL INTERFACE

To shed light on the origin of IS1 and IS2 we grew graphene on a polycrystalline copper foil, in order to eliminate contributions from the Shockley state of Cu(111) as well as from the image state of Cu(111), which is located exactly at the Γ point of the BZ. The resulting non-linear photoemission spectra ($h\nu$ = 4.05 eV) acquired on graphene/Cu foil (gr/Cu) and on clean Cu foil are shown in fig. 8.7-(a).

In the spectrum of the Cu foil only the d-band and the Fermi level are seen, indicating that in these experimental conditions we are not able to reveal any surface state ascribed to Cu foil. This is in agreement with the EBSD data shown earlier, which evidenced a prevalent (001) orientation of the Cu grains at the surface. This surface orientation of copper, unlike the (111) orientation, is known to have no Shockley surface states at the Γ point of the Brillouin zone [25]. On the contrary, a feature close to the Fermi level is evident in the spectrum acquired on graphene/Cu. This peak showed a surface-state symmetry, vanishing with s-polarized light. The binding energy with respect to the vacuum level and the effective mass (fig. 8.7-(c) and (d)) of this structure were comparable with those of IS2 of graphene/Cu(111). As

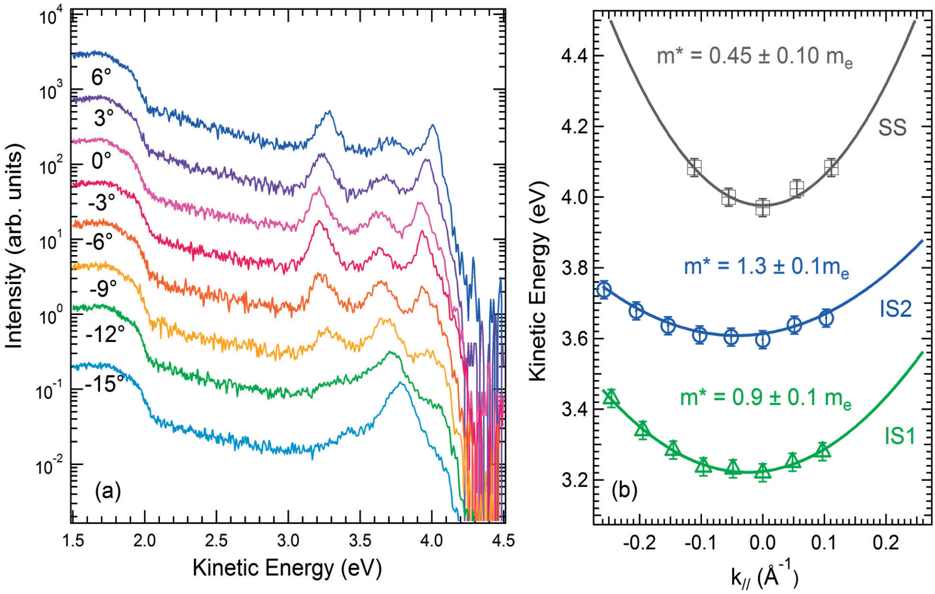

Figure 8.6: (a) Angle-resolved non-linear photoemission spectra collected at $h\nu = 4.05$ eV. (b) Kinetic energy versus $k_{||}$-momentum for the Shockley surface state (SS) and for IS1 and IS2 image potential states. The parabolic fit (line) of the data gives the effective masses reported in the figure for each surface states.

shown in fig. 8.7, IS1 is well fitted by a single Lorentzian function with an intrinsic linewidth of about 140 meV. Such value is smaller to what was found for the $n = 1$ IPS on graphite [23, 26]. These result suggest that IS1 and IS2 are due to the $n = 1$ IPS of Cu(111) and of graphene, respectively. However, the properties of these two states at graphene/Cu(111) interface differ from those observed for similar states at the weakly interacting g/Ir(111) and the strongly interacting g/Ru(0001) interfaces.

As reported in Table 8.1, the character of the Cu(111)-IPS seems to be only slightly affected by the presence of graphene: its binding energy is comparable with that of clean Cu(111) and the effective mass is consistent with the free-electron mass. This result is in contrast with what is observed for the graphene/Ir(111) interface [14] where the binding energy of the $n = 1$ IPS attributed to Ir(111) is 40% larger than on the clean surface. The graphene overlayer in close contact with the metal is expected to push the wave function of the image-potential states away from the metal surface. The maximum of the $n = 1$ wave function of the IPS of graphene grown on Ru(0001)

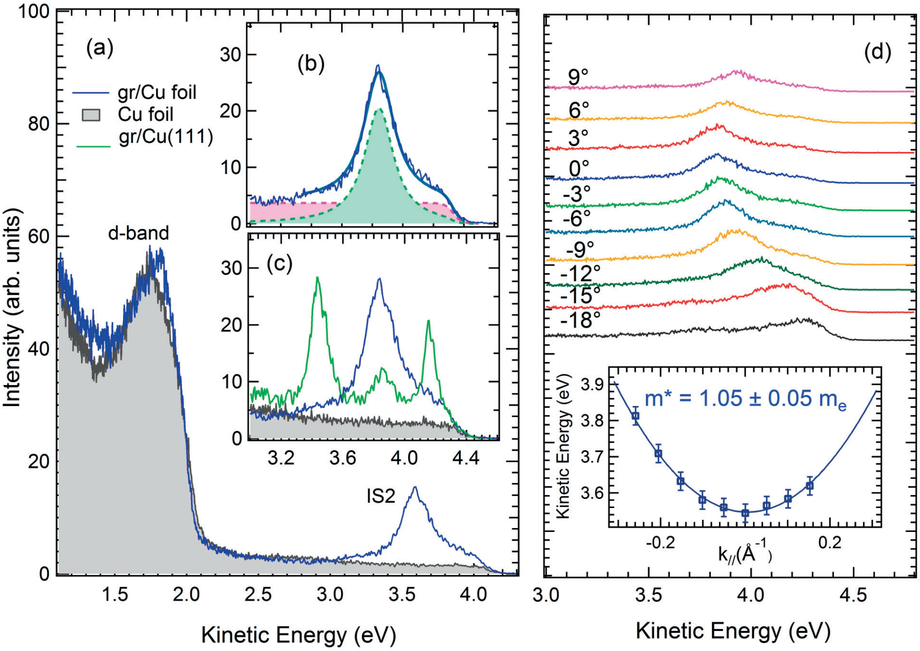

Figure 8.7: (a) Comparison between non-linear photoemission spectra collected with $h\nu$ = 4.05 eV at normal emission on graphene grown on polycristalline Cu foil and on clean Cu foil. The spectra were normalized to the maximum of the d-band (b) The spectrum in the [3.1eV- 4.5 eV] energy range results well fitted by a single Lorentzian and a Fermi Dirac function. (c) Comparison between non-linear photoemission spectra collected with $h\nu$ = 4.05 eV on graphene grown on Cu foil, clean Cu foil and graphene on Cu(111). (d) Non-linear photoemission spectra collected with $h\nu$ = 4.05 eV by varying the angle between the sample and the direction of electron detection. In the insert kinetic energy versus $k_{||}$ for IS2 state. The parabolic fit (line) of the data gives the effective mass.

is located about 2 Å away from the image plane [19]. For copper, this distance is expected to be about 3-3.5 Å and therefore the metal surface and the graphene layer can act as a quantum well if the maximum of the IPS state wave function is found to be between the graphene and the metal. This yields, in the phase shift model approach [27], to a phase shift of the IPS wave function and to a change of its binding energy.

The absence of an energy shift for graphene/Cu(111) suggests that the maximum of the Cu(111) IPS wave function falls outside the region delimited by the metal, on one side, and graphene, on the other. While the n = 1 IPS in Ir(111) is a mid-gap surface state with little interaction with the metal bulk bands, in Cu(111), the n = 1 IPS is found at the top of the gap, close to the unoccupied bulk band, resulting in a strong interaction with these states. This accounts for the different behavior of the IPS for graphene/Cu(111) and graphene/Ir(111) interfaces. The great novelty of this work is the presence of the IPS (IS2) originating from graphene, which is observed both on Cu(111) and Cu polycrystalline foil. It is important to underline that graphene IPS features have never been observed up to now, neither on the weakly interacting graphene/Ir(111) interface nor on the strongly interacting graphene/Ru(111).

As already mentioned, ab initio calculations for free-standing graphene[5] predict two $n = 1$ image potential states below the vacuum level, separated in energy by about 0.7 eV. As recently reported by DFT calculations [3], when a single layer of graphene approaches a metallic surface up to a distance larger than 3.0 Å, the energy position of the 1^+–IPS,which shows even symmetry with a larger weight towards the vacuum, remains on the same as for free-standing graphene. On the contrary, the 1^-–IPS, which shows an odd symmetry and is located at the interface region, rapidly shifts upwards in energy above the vacuum level.

Assuming that for graphene/Cu we could apply a mechanism similar to what was reported for graphene/Ru [3] and supposing, based on theoretical calculations [16, 15] that the graphene-copper distance is 3-3.5 Å, we can argue that the IS1 feature observed in our experiment is the symmetric graphene 1^+–IPS. The measured binding energy of IS2 with respect to the Fermi (vacuum) level is 3.7 ± 0.2 eV (0.5 eV) which is consistent with the value of 3.24 eV with respect to the Fermi level for free-standing graphene calculated by using LDA method [5]. However, due to the different values of the work funcion between graphene/Cu interface and free-standing graphene, the values for the binding energy refereed to the vacuum level were found to be not in agreement with each other. This could be consistent with local variations of the value of the work function [28], where the image states feel a local work function corresponding to the individual patch of graphene at which the electron is trapped.

REFERENCES

[1] J. Wintterlin and M.-L. Bocquet, *Surface Science* **603**, 1841 (2009).

[2] M. Batzill, *Surface Science Reports* **67**, 83 (2012).

[3] B. Borca, S. Barja, M. Garnica, D. Sánchez-Portal, V. M. Silkin, E. V. Chulkov, C. F. Hermanns, J. J. Hinarejos, A. L. Vázquez de Parga, A. Arnau, P. M. Echenique, and R. Miranda, *Physical Review Letters* **105**, 036804 (2010).

[4] S. Bose, V. M. Silkin, R. Ohmann, I. Brihuega, L. Vitali, C. H. Michaelis, P. Mallet, J. Y. Veuillen, M. A. Schneider, E. V. Chulkov, P. M. Echenique, and K. Kern, *New Journal of Physics* **12**, 023028 (2010).

[5] V. Silkin, J. Zhao, F. Guinea, E. Chulkov, P. Echenique, and H. Petek, *Physical Review B* **80**, 121408 (2009).

[6] M. Posternak, A. Baldereschi, A. J. Freeman, and E. Wimmer, *Physical Review Letters* **52**, 863 (1984).

[7] D. Dougherty, P. Maksymovych, J. Lee, M. Feng, H. Petek, and J. Yates, *Physical Review B* **76**, 125428 (2007).

[8] U. Höfer, I. L. Shumay, C. Reuß, U. Thomann, W. Wallauer, and T. Fauster, *Science* **277**, 1480 (1997).

[9] G. Csányi, P. B. Littlewood, A. H. Nevidomskyy, C. J. Pickard, and B. D. Simons, *Nature Physics* **1**, 42 (2005).

[10] M. Zamkov, N. Woody, S. Bing, H. Chakraborty, Z. Chang, U. Thumm, and P. Richard, *Physical Review Letters* **93**, 156803 (2004).

[11] M. Zamkov, H. Chakraborty, A. Habib, N. Woody, U. Thumm, and P. Richard, *Physical Review B* **70**, 115419 (2004).

[12] M. Feng, J. Zhao, and H. Petek, *Science* **320**, 359 (2008).

[13] J. Zhao, M. Feng, J. Yang, and H. Petek, *ACS Nano* **3**, 853 (2009).

[14] D. Niesner, T. Fauster, J. I. Dadap, N. Zaki, K. R. Knox, P. C. Yeh, R. Bhandari, R. M. Osgood, M. Petrović, and M. Kralj, *Physical Review B* **85**, 081402 (2012).

[15] Z. Xu and M. J. Buehler, *Journal of Physics: Condensed Matter* **22**, 485301 (2010).

[16] G. Giovannetti, P. A. Khomyakov, G. Brocks, V. M. Karpan, J. van den Brink, and P. J. Kelly, *Physical Review Letters* **101**, 026803 (2008).

[17] P. A. Khomyakov, G. Giovannetti, P. C. Rusu, G. Brocks, J. van den Brink, and P. J. Kelly, *Physical Review B* **79**, 195425 (2009).

[18] B. Kelly, *Physics of Graphite*, RES mechanica monographs, Kluwer Academic Pub (1981).

[19] N. Armbrust, J. Güdde, P. Jakob, and U. Höfer, *Physical Review Letters* **108**, 056801 (2012).

[20] M. Montagnese, *Non-linear angle-resolved photoemission of Graphite: surface and bulk states*, Ph.D. thesis, Scuola di Dottorato di Fisica, Astrofisica e Fisica Applicata, Università degli Studi di Milano (2009).

[21] M. Wolf, A. Hotzel, E. Knoesel, and D. Velic, *Physical Review B* **59**, 5926 (1999).

[22] S. Pagliara, G. Ferrini, G. Galimberti, E. Pedersoli, C. Giannetti, C. A. Rozzi, and F. Parmigiani, *Surface Science* **602**, 2983 (2008).

[23] J. Lehmann, M. Merschdorf, A. Thon, S. Voll, and W. Pfeiffer, *Physical Review B* **60**, 17037 (1999).

[24] S. Pagliara, G. Ferrini, G. Galimberti, E. Pedersoli, C. Giannetti, and F. Parmigiani, *Surface Science* **600**, 4290 (2006).

[25] R. Courths and S. Hüfner, *Physics Reports* **112**, 53 (1984).

[26] S. Pagliara, M. Montagnese, S. Dal Conte, G. Galimberti, G. Ferrini, and F. Parmigiani, *Physical Review B* **87**, 045427 (2013).

[27] P. M. Echenique and J. B. Pendry, *Journal of Physics C: Solid State Physics* **11**, 2065 (1978).

[28] R. Fischer, S. Schuppler, N. Fischer, T. Fauster, and W. Steinmann, *Physical Review Letters* **70**, 654 (1993).

Appendix A

Fundamental properties of graphene

Graphite (and therefore graphene) is one of the result of the capability of the carbon atoms to form several types of chemical bonds and, consequently, to be able to appear in several allotropes. Its electronic configuration (at the ground state) is $(1s^2)(2s^2)(2p^2)$, which can lead to different hybridization of the chemical bonds and, therefore, to different crystalline structures. Diamond (figure A.1-(a)) appears as a 3D typical lattice, formed by carbon atoms bonded with sp^3-hybridized bonds, having a fcc symmetry with a basis of two carbon atoms.

On the other hand, in graphene (figure A.1-(b)) only the s, p_x and p_y atomic orbitals are hybridized and form the so-called σ molecular orbital, while the unhybridized p_z are forming the π molecular orbitals. The σ orbitals are oriented along the graphene plane and arrange the carbon atoms in a honeycomb crystalline lattice, with interatomic distances amounting to 1.42 Å.

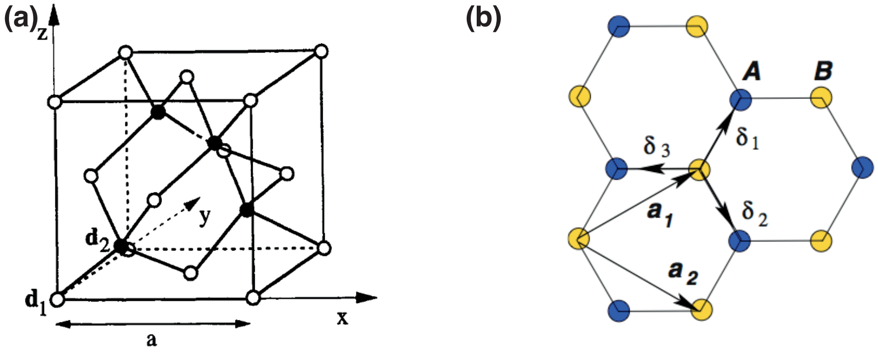

Figure A.1: Crystalline structure of (a) diamond and (b) graphene. See the text for explanation to the image. Adapted from [1] and [2]. © 2000 by Academic Press and © 2009 by American Physical Society.

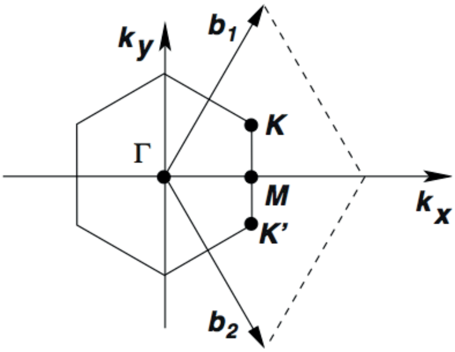

Figure A.2: First Brillouin zone of graphene, with reciprocal lattice vectors and high-symmetry points [2]. © 2009 by American Physical Society.

The honeycomb structure can be easily described as a triangular lattice with a basis of two carbon with two non-equivalent atoms (A and B in figure A.1-(b)) per unit cell. The lattice vectors can be written as [2]

$$\mathbf{a}_1 = \frac{a}{2}\left(3, \sqrt{3}\right) \qquad \mathbf{a}_2 = \frac{a}{2}\left(3, -\sqrt{3}\right) \quad \text{with } a = 1.42\ \text{Å}. \tag{A.1}$$

We can also write the expression for the first-neighbor distances, as marked in figure A.1-(b)

$$\delta_1 = \frac{a}{2}\left(1, \sqrt{3}\right) \quad \delta_2 = \frac{a}{2}\left(1, -\sqrt{3}\right) \quad \delta_3 = -a(1, 0). \tag{A.2}$$

Consequently, the reciprocal lattice vectors are

$$\mathbf{b}_1 = \frac{2\pi}{3a}\left(1, \sqrt{3}\right) \qquad \mathbf{b}_2 = \frac{2\pi}{3a}\left(1, -\sqrt{3}\right) \quad \text{with } a = 1.42\ \text{Å}. \tag{A.3}$$

The hexagonal first Brillouin zone of graphene (see figure A.2) can be reduced, by symmetry considerations, to a triangle, whose corners are Γ, K and K'. In particular, the position of these two points in the Brillouin zone are

$$K = \left(\frac{2\pi}{3a}, \frac{2\pi}{3\sqrt{3}a}\right) \qquad K' = \left(\frac{2\pi}{3a}, -\frac{2\pi}{3\sqrt{3}a}\right) \tag{A.4}$$

The electronic properties of graphene are, to a large extent, depending on the electronic structure at the K points (named, *Dirac points*). The electronic band structure of a single layer of graphene was calculated, as stated earlier, with a tight-binding approach [3, 2]. The tight-binding Hamiltonian for electrons in graphene considering that electrons can hop to both nearest- and next-nearest-neighbor atoms has the form

$$\mathcal{H} = -t \sum_{\langle i,j\rangle,\sigma} \left(a^{\dagger}_{\sigma,i} b_{\sigma,j} + H.c.\right) - t' \sum_{\langle\langle i,j\rangle\rangle,\sigma} (a^{\dagger}_{\sigma,i} a_{\sigma,j} + b^{\dagger}_{\sigma,i} b_{\sigma,j} + H.c.) \qquad (\hbar = 1), \quad \text{(A.5)}$$

where $a^{\dagger}_{\sigma,i}$ ($a_{\sigma,i}$) creates (annihilates) an electron in the position R_i, with spin σ in the sub-lattice A. $H.c.$ indicates the conjugated term of the hamiltonian. Analogous definition is given for the electrons created (or annihilated) in the sub-lattice B. t is the nearest neighbor hopping energy (2.8 eV), while t' is the next-nearest neighbor hopping energy. The resulting band structure is [3, 2].

$$E_{\pm}(\mathbf{k}) = \pm t\sqrt{3 + f(\mathbf{k})} - t' f(\mathbf{k}), \qquad \text{(A.6)}$$

having

$$f(\mathbf{k}) = 2\cos(\sqrt{3}k_y a) + 4\cos\left(\frac{\sqrt{3}}{2}k_y a\right)\cos\left(\frac{3}{2}k_x a\right). \qquad \text{(A.7)}$$

The resulting band structure is depicted in figure A.3. With the ± sign, we indicate the upper (π^*, conduction) and the lower (π, valence) band. If we do not include the next-nearest neighbor hopping ($t' = 0$), the spectrum is symmetric around zero energy. Symmetry is broken if we introduce a non-vanishing t'. To achieve the dispersion in the vicinity of the Dirac points we now introduce a relevant approximation. For small excitations energy we can write the dispersion relation (A) as

$$E_{\pm}(\mathbf{q}) \approx \pm\hbar v_F|\mathbf{q}| + o[(q/K)^2], \qquad \text{(A.8)}$$

where $\mathbf{q}$ is the crystalline momentum measured with respect to the Dirac point, such as $\mathbf{k} = \mathbf{K} + \mathbf{q}$, with $|\mathbf{q}| \ll |\mathbf{K}|$. v_F is the so-called Fermi velocity and accounts to be $v_F = \frac{\partial E}{\partial k} = 3ta/2 = 10^6\ m/s$. The velocity of the electrons does not depend on the energy or momentum: in the case of free electrons, we have $v = k/m = \sqrt{2E/\hbar^2 m}$ and hence the velocity changes substantially with energy.

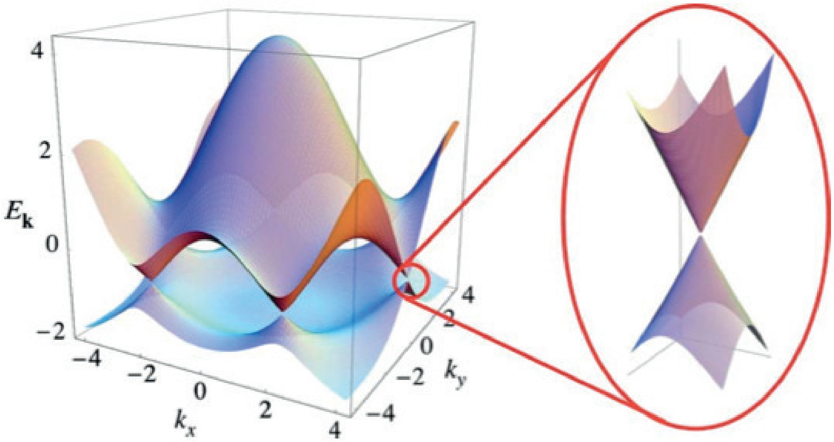

Figure A.3: Electronic dispersion in the honeycomb lattice. Left: energy spectrum (in units of t) for finite values of t and t′, with $t = 2.7$ eV and $t' = -0.2t$. Right: zoom in of the energy bands close to one of the Dirac points [2]. © 2009 American Physical Society.

REFERENCES

[1] G. Grosso and G. Parravicini, *Solid State Physics*, Academic Press (2000).

[2] A. H. Castro Neto, F. Guinea, N. M. R. Peres, K. S. Novoselov, and A. K. Geim, *Review of Modern Physics* **81**, 109 (2009).

[3] P. R. Wallace, *Physical Review* **71**, 622 (1947).

Summary

The aim of this thesis is to deepen the knowledge about substrate induced modifications of electronic and structural properties of graphene grown or deposited on metallic surfaces. Such task has been accomplished by employing a wide combination of Surface Science techniques.

The growth of graphene on metallic surfaces by means of chemical vapour deposition (CVD) has been recently exploited to achieve graphene layers on a large scale and easily transferrable to other substrates. In the last years, CVD has appeared to be the most promising method of growth to be successfully implemented into a mass-scale production of graphene, aiming to the achievement of a graphene-based electronics. Many efforts have been devoted in the last years to improve the quality of the final product and to industrially implement CVD growth of graphene.

Despite of their importance at an applicative level, the features of graphene-metal interfaces are as well interesting from a fundamental point of view: the modifications in the graphene properties are depending on the metal on which it is adsorbed, ranging from weak to strong interaction. As a consequence of this, the electronic band structure of graphene can be severely affected by the metallic substrate, resulting in an electronic doping of graphene at metallic contacts, in modifications of the work function or in provoking substrate-induced morphology modifications of the graphene layer.

Chapter 1 provided a general introduction to the topic, listing all the achievements so far acquired about graphene/metal interfaces. Chapter 2 addressed the methods of preparation of these interfaces by means of CVD, providing a detailed description of the protocols employed.

In chapter 3 and 4 we reported an investigation on the graphene/Ni(111) interface by employing time-resolved photoemission based on a high harmonics generation setup. A preliminary photon-energy dependent study on valence band spectra of graphene/Ni(111) allowed to individuate the selection rules for photoemission from the valence band of the interface and to sketch a profile for the photoemission cross section. A pump-probe experiment allowed to extract information about the lifetimes of photoexcited electronic states and about the mechanism of depopulation from the excited to the ground state of the system.

Chapter 5 provides a wide overview of the electronic and structural properties of the graphene/Cu(111) interface, prepared with a fully ex-situ approach. The influence of the different steps of the CVD growth procedure on the final graphene/Cu(111) interface were discussed. Angle-resolved photoemission allowed casting an eye on the band structure of the interface, revealing an unaltered Dirac cone. Scanning tunneling microscopy outlined areas covered with a Moirè pattern, due to differences in lattice parameters of copper and graphene, and areas with no Moirè, although graphene was detected. By combining these observations we speculated about the presence of a layer of native oxide intercalated between the metal and the graphene.

In chapter 6 we present a multi-technique characterization of graphene grown by chemical vapour deposition (CVD) and thereafter transferred to and suspended on a grid for transmission electron microscopy (TEM). We demonstrated that the suspended graphene membrane locally shows electronic properties comparable with those of samples prepared by micromechanical cleaving of graphite. We suggested that to enable a large-scale use of CVD graphene for electronics it is important that the folding of the graphene during the transfer is prevented.

Chapter 7 reported the study of the nanofrictional properties of Xenon monolayers deposited on graphene in a range of temperatures between 25 and 50 K by means of the quartz crystal microbalance technique. We found that the coverage at which the gas layer starts to slip on graphene/Au increases linearly with decreasing temperature of the substrate while on the bare Au surface no temperature dependence was found. In addition, the slip times measured on gold are much higher than those on graphene.

In chapter 8, an investigation of the surface states at the weakly coupled interface graphene-copper by means of non-linear angle resolved photoemission spectroscopy is reported. Comparing the spectra collected on graphene grown on Cu(111) and on copper polycrystalline foil, we are able to identify the Shockley surface state and the $n = 1$ image state of the Cu(111) surface and the symmetric $n = 1$ image state of the single layer of graphene.

Samevatting

Het doel van deze thesis is het verbreden van de kennis over door het substraat geïnduceerde modificaties van de elektronische en structurele eigenschappen van grafeen welke is gegroeid of geplaatst op metaaloppervlakken. Deze taak is volbracht door gebruik te maken van een combinatie van wetenschappelijke oppervlaktetechnieken.

Het groeien van grafeen op metallische oppervlakken door middel van chemische dampdepositie (CVD) is uitgebreid geëxploiteerd om lagen grafeen op grote schaal te verkrijgen, welke makkelijk zijn over te brengen op andere substraten. De laatste jaren blijkt CVD de meest veelbelovende groeimethode te zijn om met succes te implementeren in een grafeenproductie op massaschaal, met het doel op grafeen gebaseerde elektronica te bereiken. Vele inspanningen zijn gewijd aan de kwaliteit van het eindproduct en aan het industrieel implementeren van CVD-groei van grafeen.

Bovenop hun belang voor applicaties zijn de eigenschappen van grafeen/metaaloppervlakken ook interessant vanuit een fundamenteel oogpunt: de modificaties van de grafeeneigenschappen hangen af van het metaal waarop het geabsorbeerd is en variëren van zwakke tot sterke interactie. In het laatste geval kan de elektronische bandstructuur van grafeen sterk beïnvloed worden door het metaalsubstraat, wat resulteert in een elektronische doping van grafeen- en metaalcontacten, in modificatie van de werkfunctie of in het provoceren van door het substraat geïnduceerde veranderingen in de morfologie van de grafeenlaag.

Hoofdstuk 1 biedt een algemene introductie op het onderwerp en bespreekt wat er tot nu toe bekend is over grafeen/metaaloppervlakken. Hoofdstuk 2 beschrijft de preparatiemethoden van deze oppervlakken door middel van CVD, met een gedetailleerde beschrijven van de gebruikte protocollen.

Hoofdstuk 3 en 4 rapporteren over een onderzoek naar het grafeen/Ni(111)-raakvlak met behulp van tijdsopgeloste foto-emissie gebaseerd op een opstelling waarin hoge harmonischen worden gegenereerd. Een fotonenergie afhankelijke studie op de valentiebandspectra van grafeen/Ni(111) stond het identificeren van de selectieregels

voor fotoemissie van de valentieband van het raakvlak, en het schetsen van een profiel voor de fotoemissie doorsnede toe. Een pump-probe experiment stond het verkrijgen van informatie over de levensduur van fotogeëxiteerde elektronische toestanden en het verhelderen van het vervalmechanisme van de aangeslagen ladingsdragers toe.

Hoofdstuk 5 biedt een overzicht van de elektronische en structurele eigenschappen van het grafeen/Cu(111)raakvlak, geprepareerd met een volledige ex-situ benadering. De invloed van de verschillende stappen van de CVD-groeiprocedure op het uiteindelijke grafeen/Cu(111)raakvlak worden bediscussieerd. Hoek-opgesloten foto-emissie onthulde een onveranderde Dirac-kegel in de bandstructuur van het raakvlak net boven het Ferminiveau. Rastertunnelmicroscopie laat gebieden zien die bedekt zijn met een Moiré patroon, dat komt door de verschillen in roosterparameters van koper en grafeen, welke bestaan naast door grafeen bedekte gebieden zonder Moiré patroon. Deze observaties geven de suggestie van de aanwezigheid van een laag van natuurlijk oxide geïntercaleerd tussen het metaal en het grafeen.

Hoofdstuk 6 presenteert een karakterisatie door verschillende technieken van grafeen, gegroeid met behulp van chemische dampdepositie (CVD), welke was overgebracht naar en opgehangen aan een rooster voor transmissie elektronen microscopie (TEM). Het opgehangen grafeenmembraan laat plaatselijk de elektronische eigenschappen zien, vergelijkbaar met de eigenschappen van samples geprepareerd met het micromechanisch klieven van grafiet. Echter, bij de productie van opgehangen grafeen samples moet men rekening houden met het omvouwen van de randen van het membraan, wat de eigenschappen van een gehele vlok kan beïnvloeden (hoofdstuk 6).

Hoofdstuk 7 rapporteert over de studie naar de nanowrijvingseigenschappen van Xenon monolagen op grafeen met een reeks temperaturen van 25 to 50 K door middel van de kwartskristalmicrobalanstechniek. Er is gevonden dat de dekkingsgraad waarbij de gaslaag begint te glijden over de grafeen/Au lineair toeneemt als de temperatuur van het substraat afneemt, terwijl op het kale Au oppervlak geen temperatuurafhankelijkheid werd waargenomen. Verder zijn de glijtijden gemeten op goud veel hoger dan deze gemeten op grafeen.

Hoofdstuk 8 focust op oppervlaktetoestanden op het zwak gekoppelde grafeen-koper-raakvlak, welke onderzocht zijn door middel van niet-lineaire hoekopgeloste foto-emissie-spectroscopie. Als de spectra verkregen voor grafeengroei op Cu(111) en op polykristallijn Cu-folie vergeleken worden, kunnen de Shockley oppervlaktetoestand en de $n = 1$ afbeeldingstoestand van de Cu(111) alsmede de symmetrische $n = 1$ afbeeldingstoestand van de enkele laag grafeen geïdentificeerd worden.

Acknowledgements

The research activity which I carried out in these last four years, widely described in this dissertation, could not have been accomplished without the help and the support of many people.

First of all, I wish to thank my PhD advisor and promotor, prof. Petra Rudolf. Petra, you decided to take me as one of your students to work on a very challenging project. Despite of difficulties, we are now harvesting the rewards of a great effort. Thank you very much for the many things I have learned from you, from organizing my scientific activity up to how to write a good paper. You always told me that if I have some idea, I just have to stand up and realize it: I think this is the best attitude and motivation for a scientist wishing to progress with his/her research.

My grateful acknowledgment goes also to my co-promotor, Dr. Meike Stöhr. Meike, thank you very much for all the support and good ideas which you contributed to my project. You always gave me good suggestions and hints, helping me to see from a different perspective the problems I was facing.

I gratefully thank the members of my reading committee, prof. Helmut Zacharias, prof. Giampaolo Mistura and prof. Jeff de Hosson for reading and approving the manuscript and for the suggestions they provided.

In particular, I wish to thank prof. Zacharias, together with Dr. Thorben Haarlammert and Carsten Winter, for the hospitality during my work at the Münster University and for the great contributions you gave to our common research project, leading to important and interesting results: thanks for the many suggestions you provided, which helped me to increase my knowledge in the field of time-resolved photoemission. My deep acknowledgment goes also to Dr. Elena Voloshina, for her important theoretical support to the project.

I am grateful to prof. Mistura for the collaboration we carried out in a field that was unknown to me, but which opened me many new perspectives. Thanks to prof. de Hosson for the suggestions and comments in the preparation of the manuscript on suspended graphene.

I gratefully acknowledge prof. Fulvio Parmigiani, for the great support and advices he gave me in these years. I always enjoyed our discussions aiming to understand "the Physics" behind the outcomes of the experiments. You taught me how to enjoy the wonder which comes out from a beautiful experiment. I hope to be able in my career to stick to this philosophy and attitude towards the scientific research.

Thanks to prof. Paul val Loosdrecth and Dr. Matteo Montagnese for fruitful discussions about Physics and for the collaboration in the teaching activity of the course of Kwantumfysica 2. Matteo, I had the privilege to collaborate with you and I am very grateful for the many good suggestions you provided in these years, having always a good solution at the right moment. I enjoyed very much the discussion with you and I am thankful for your efforts to help me to organize my research activity. Paul: thanks for your always very clear point of view and honest opinion about many issues.

During the last two years of my phd I have actively collaborated with Dr. Willem van Dorp. Willem: thank you very much for the many things you taught to me and for the good science we have carried out together. I enjoyed to work with you, in a relaxed but always focused and attentive manner, producing interesting and nice results. I wish you all the best for your future academic career.

The image-potentials-states project was performed in collaboration with Silvia Tognolini, Dr. Stefania Pagliara and Dr. Gianluca Galimberti. Thank you very much for the measurements and the important contribution you gave to the research activity of my PhD and for the good piece of science we have realized together.

A special acknowledgment goes to my paranymphs: Oleksii and Marianna. Oleksii, it was a privilege to meet such a thoughtful, attentive and competent scientist as you are. Your passion and love for Science are always a great example for myself. You have been a great friend in these years in Groningen with whom I shared so many different activities, from scientific discussion to "sampling beers", as you say... I am proud you agreed to be my paranymph and I foresee a bright future for you.

Mary, you are an enthusiastic, passionate, thoughtful and polyhedric scientist and and a very good friend. It was a great pleasure and great luck for me to meet you. Thanks for the many discussions and chats we had: they brought always new motivations to me. You are a smart scientist and a talented singer: I wish you success in Music as much as in Physics.

During these years I met many researchers at the Surfaces and Thin Films group, from which I have learned a lot and with whom I shared the lab life.

I wish to thank the office 0052, Oleksii, Stefano and Peter. Gentlemen, our office was an incredible synthesis of totally different cultures and attitudes. It will be difficult to find such great officemates in the future. Thanks for participating in my glad moments, for your patience during my frustrations and for standing my "suffering lady" music.

Stefano, you are a truly creative and passionate physicist and a great friend. I admire your determination to achieve the results and your creativity. It was a great pleasure to work on projects together with you: I really enjoyed it. Thank you very much for your friendship and support during these years.

Peter, you are the Dutch component of the office, bringing a taste of Dutch mood to us. Thank you very much for your help in these years with "Nederlands" issues and for the nice discussions about the Dutch politics and society.

Naureen, you are a very good and competent scientist. Although our projects were so different, we shared many concerns of the phd life. I enjoyed to take part in some discussions about them. I wish you all the best for your future career.

Martina, you brought a light touch of mess and craziness to the group and also to our office, just popping in at any time during the day and starting to talk with us. I enjoyed our coffee discussions about your experiments, the politics and the life. Your determination is exemplary and it will bring you successful results.

Kostas, we started together our PhD but you beated me on the finish line! We have learned many things together, even if with different attitudes and ways. Thanks for all the time we spent in discussing how to progress in our PhD research and for sharing many of the issues of our work.

Tatiana, you introduced me in the group and to Groningen. Thanks for being very supportive at the early stages of my doctorate and to push me and encourage me when it was necessary.

I wish to thank all the other researchers I have met in the group: Regis, Lumi, Yu, Fei, Ahn, Juan Carlos, Kathrin, Florian, Mihaela, Tashfeen, Jiquan, Jordi, Mary, Hans, Sadaf, Ali, Rossella, Fouli, Jotta, Liliane, Andre: I wish you all to progress with your scientific research and not to lose the enthusiasm about it. A grateful acknowledgment goes to Luc Venema: I could really take advantage of your competence about many equipments and devices. You always came out with a good hint for each problem we found on our experiments, helping me to greatly progress with my research. A special thanks goes to Yvonne, for her precious and kind help during these years.

My acknowledgement goes to Dr. Tamalika Banerjee and Subir Parui for the fruitful collaboration on the nickel-silicides project. I have met a wide number of people

during these years at the Zernike Institute: Juliane, Alina, Jasper, Marcos, Thomas, Nikos, Magda, Paul, Johan, Ivan, Davide, Simone, Michiel, Toni, Maria, Michel, Elia. Thank you for the good environment you cooperated to create at the Institute, which was very stimulating for my personal progress.

Groningen gave me the chance to meet many friends from any part of the world, with whom I shared many moments of my life. You have been my family here in the Netherlands and I owe you wide part of this success, always standing next to me to celebrate happy moments and to support during hard times. Marianna, Oleksii, Silvia, Giovanni, Andrea, Lucia, Patrizio, Elena, Stefano, Teresa, Aartje, Andrea, Giulio, Fabio, Alessio, Elena, Manuela, Martina, Stefano, Toni, Matteo, Elia, Heidi, Tati, Santi, Stefanie, Maria Jesus, Nuria, Tom, Maria Josè, Tano, Johanne, Valentin, Puri, Sara, Lucas, Hector, Raquel, Ana, Juliane, Filippo, Dorota, Alessio, Daniele, Valerio, Giulia, Francesco, Cecilia, Elena, Davide: probably a book would not be enough to gather and contain my gratitude for you. You are the most important reason for which I will never forget Groningen. Thanks to all my italian friends: they were always warmly welcoming me when I was visiting back home. Stefano, Federica, Patrizia, Bruno, Giulio, Federico, Stefano, Raimondo, Giovanni, Isa, Marco, Davide, Carola, Mary, Marco, Ilaria, Yuki, Matteo. You guys were the link between the Netherlands and Italy, a link that I want to preserve carefully and bring with me wherever I will end up.

Un grande ringraziamento va alla mia famiglia. Avete sempre appoggiato in tutto le mie scelte, sempre sostenendomi e dandomi quell'incoraggiamento che mi ha permesso di arrivare fin qua. Pa, Ma, Emanuele, Paolo e tutti gli altri: questa tesi e tutto il lavoro che essa ha comportato sono dedicati a voi, a dimostrazione del mio affetto, della mia riconoscenza e dell'attaccamento alle mie radici. Voglio in particolare ringraziare Emanuele: Lele, durante gli ultimi quattro anni, alcuni dei quali abbiamo condiviso qui a Groningen, sei stato un fratello, un amico e un consigliere come raramente se ne possono trovare. Non potrai fisicamente essere presente alla mia doctoral defense, ma ti sentiró vicino, come sempre ti ho sentito in tutti questi anni. Spero che queste parole possano essere un sincero segno di riconoscenza, dandoti una motivazione per rinascere e ripartire.

Luca
Groningen, May 2013

Curriculum Vitae

Luca Bignardi
Date of birth: 27th July 1984.
Place of birth: Cremona, Italy.
email: luca.bignardi@gmail.com

2008-2013
PhD researcher, Physics, Stichting voor Fundamenteel Onderzoek der Materie (FOM) and Zernike Institute for Advanced Materials, University of Groningen (NL).
Thesis title: *Electronic and structural properties of graphene/metal interfaces.*

2006-2008
MSc in Physics, Università Cattolica del Sacro Cuore, Brescia.
Thesis title: *Time-resolved reflectivity and photoemission studies on graphite.*

2003-2006
BSc in Physics, Università Cattolica del Sacro Cuore, Brescia.
Thesis title: *Second Harmonic Generation with ultra-short laser pulses in KNS ceramic glasses.*

1998-2003
High school, Liceo Scientifico Statale "Aselli", Cremona.